



**Experimental study on the influence
of fluid dynamics and mixing on
crystallisation of PABA in multiphase
flow systems**

Valentina Nappo

Department of Chemical Engineering

University College London

A thesis submitted for the degree
of Doctor of Philosophy of University College London

I, Valentina Nappo, confirm that the work presented in this thesis is my own. Where information has been derived from other sources, I confirm that this has been indicated in the thesis.

Signature

Date

Abstract

Cooling crystallization is extensively used by the pharmaceutical industry to produce and purify Active Pharmaceutical Ingredients. Nucleation, that is the first step of crystallization, is pivotal in determining the final product properties. For these reasons, understanding the nucleation process and the factors that control crystal formation is essential to limit product variations and ultimately to improve the efficacy and the safety of the final drug.

This thesis aims to investigate the mechanisms responsible for initiating nucleation in a clear solution and to identify the key process parameters that control nucleation. In particular, we used three experimental systems to explore the influence of micromixing, shear rate and gas bubbles under a wide range of fluid dynamic conditions.

The first part of this work focuses on the experimental characterization of two laboratory scale batch systems to explore the effect of micromixing on metastable zone width (MZW) in industrial-like fluid dynamic conditions. The results demonstrated that, although increasing agitation is beneficial in reducing the MZW, the presence of gas bubbles was more effective in inducing nucleation supporting the theory that the gas bubbles offer a surface for heterogeneous nucleation. However, due to the complexity of the systems studied (non-spatially uniform fluid dynamic), it is difficult to untangle the effect of the various process parameters. For this reason, a novel droplet-based crystalliser was used to quantitatively investigate the effect of shear rate in well-controlled fluid dynamic conditions (quiescent-stagnant conditions, low-shear laminar flow and high-shear turbulent flow). The results suggested that a shear field can significantly enhance primary nucleation by increasing the meso-scale cluster collision efficiency. However, further experimentation is necessary in order to verify this hypothesis. Finally, a novel experimental system was proposed to explore the possibility of heterogeneous nucleation on gas bubbles. The experiments revealed that nucleation on gas-liquid interface is favoured.

Impact statement

Crystallization is a common unit operation designed to separate and purify crystalline materials. It has been used for decades, and is widely employed in the pharmaceutical industry for the production of most drugs, however, crystallization is still poorly understood and often an empirical approach is used to identify optimal values of the critical parameters controlling the crystals formation. This often results in poor quality crystals that need to undergo additional processes in order to acquire the desired characteristics (i.e. low aspect ratio shape, narrow particle size distribution and small dimensions), increasing both the manufacturing costs and the production time. An optimal control of the crystallization process is essential to obtain high quality crystals with high reproducibility; however, industries face many challenges in this regard due to a poor understanding of the crystallization mechanism and of the parameters affecting it. A better understanding of this process is crucial especially when it comes to crystallization of Active Pharmaceutical Ingredients (APIs), which is the first step of many drugs manufacture. Non-uniform crystals can be in fact responsible for a number of issues during drug formulation, as well as decreasing the effectiveness of the drug itself.

In this work, I exploited traditional reactors and novel microfluidic devices with the aim of exploring the influence of various parameters on crystal nucleation, which is the first step of crystallization. Compared to traditional reactors, microfluidic devices offer an optimal control of the experimental conditions (temperature, fluid dynamics etc.) and allow fundamental studies on nucleation kinetics to be performed. The results obtained using these techniques contribute to the fundamental understanding of crystallization and lead to a better design of the crystal production process. On the other hand, the use of traditional reactors allowed studies to be performed under operating conditions which are closer to those used in industry and therefore are more directly applicable to industrial practice. The combined use of these techniques will contribute to the fundamental understanding of the factors affecting crystal formation, and will help to improve process controllability to produce uniform high quality crystals.

Table of Contents

Abstract.....	3
Impact statement	4
Table of Contents.....	5
List of figures.....	9
List of tables.....	15
Chapter 1 INTRODUCTION.....	18
1.1 Research background	19
1.2 Thesis objective	22
1.3 Thesis outline	22
Chapter 2 LITERATURE REVIEW.....	24
2.1 Fundamentals of crystallization	25
2.1.1 Nucleation thermodynamics.....	25
2.1.2 Nucleation kinetics.....	30
2.1.3 Metastable zone	34
2.1.4 Induction time	36
2.1.5 Stochastic model of nucleation.....	37
2.1.6 Secondary nucleation.....	42
2.1.7 Crystal growth	42
2.1.8 Crystal breakage and crystal agglomeration.....	44
2.2 Fundamentals of mixing	45
2.2.1 Mixing time scales.....	45
2.2.2 Micromixing characterization through chemical reaction methods	48
2.2.3 Micromixing models.....	49

Table of contents

2.2.4	Mixing and energy dissipation in agitated vessels	53
2.2.5	Energy dissipation in a bubble column	56
2.2.6	Influence of fluid dynamics on small particles motion and aggregation	57
2.2.7	Effect of agitation on the nucleation rate of crystals in solution	60
2.3	Microfluidics	64
Chapter 3 MICROMIXING EFFICIENCY AND LOCAL ENERGY DISSIPATION IN STIRRED TANK AND BUBBLE COLUMN REACTORS.....		70
3.1	Introduction	71
3.2	Experimental setup and procedure	72
3.2.1	Reaction system	72
3.2.2	Segregation index.....	73
3.2.3	Experimental procedure	75
3.2.4	Experimental setup	77
3.3	Results and discussion	80
3.3.1	Results from micromixing model	80
3.3.2	Injection time and mesomixing considerations	81
3.3.3	Loss of iodine due to stripping	82
3.3.4	Stirred tank: effect of agitator speed and feed position	83
3.3.5	Bubble column: effect of gas flow rate and feed position.....	88
3.3.6	Comparison between the stirred tank and the bubble column	91
3.4	Conclusion.....	93
Chapter 4 EFFECT OF FLUID DYNAMICS ON NUCLEATION OF PABA IN STIRRED TANKS AND BUBBLE COLUMNS.....		95
4.1	Introduction	96
4.2	Experimental	96

Table of contents

4.2.1	Materials	96
4.2.2	Experimental setup	98
4.2.3	Experimental procedure	99
4.3	Results and discussion	100
4.3.1	Concentration determination from conductivity measurements	100
4.3.2	Temperature profile.....	103
4.3.3	Metastable zone width	104
4.3.4	Effect of impeller rotational speed	105
4.3.5	Effect of the gas flow rate.....	109
4.3.6	Effect of local fluid dynamic conditions	111
4.4	Conclusion.....	114
Chapter 5	EFFECT OF SHEAR RATE ON NUCLEATION KINETICS OF PABA IN MILLICHANNELS.....	117
5.1	Introduction	118
5.2	Experimental.....	119
5.2.1	Materials	119
5.2.2	Experimental setup and procedure	119
5.3	Results.....	127
5.3.1	Nucleation rate under stagnant conditions	127
5.3.2	Nucleation rate under flow conditions	129
5.3.3	Stochastic model validation	132
5.3.4	Nucleation rate in stirred vials	132
5.4	Discussion	136
5.5	Conclusion.....	138
Chapter 6	CRYSTAL NUCLEATION ON A GAS-LIQUID INTERFACE.....	140

Table of contents

6.1	Introduction	141
6.2	Experimental section	141
6.2.1	Experimental setup and procedure	141
6.2.2	COMSOL simulation of temperature profile	145
6.3	Results and discussion	146
6.4	Conclusion and future recommendations	151
Chapter 7	CONCLUSION AND FUTURE WORK.....	154
7.1	General conclusions.....	155
7.2	Future work.....	158
Appendix A	Triiodide extinction coefficient determination	160
Appendix B	Acid injection procedure	165
Appendix C	Metastable zone width determination for the droplet based crystallizer ..	166
Appendix D	Image processing using Matlab®	167
Appendix E	Raw data Chapter 3	170
E.1	Stirred tank	170
E.2	Bubble column	175
Appendix F	Raw data Chapter 4.....	178
F.1	Stirred tank	178
F.2	Bubble column	179
Appendix G	Raw data Chapter 5.....	181
Appendix H	Raw data Chapter 6.....	183
	List of symbols	188
	References.....	192

List of figures

Figure 2.1 Nucleation mechanisms (adapted from Mullin, 2001)	25
Figure 2.2 (a) Homogeneous nucleation of a spherical cluster; (b) heterogeneous nucleation of cap-shaped cluster; (c) heterogeneous nucleation of disk-shaped cluster. Adapted from (Kashchiev & van Rosmalen, 2003).	28
Figure 2.3 Dependence of the shape factor from the contact angle Θ according to eq. (2.12).	29
Figure 2.4 Interfacial tensions at the boundaries between three phases (two solids, one liquid), adapted from (Mullin, 2001).	30
Figure 2.5 Schematic representation of the classical nucleation path-way (top) and two-step nucleation (Davey et al., 2013)	31
Figure 2.6 Supersaturation curve and metastable zone (Wohlgemuth, 2012).	36
Figure 2.7 Qualitative dependence of MZW on the nucleation mechanism (Wohlgemuth, 2012).	37
Figure 2.8 Concentration driving forces in crystal growth in solution according to the diffusion-reaction model (Mullin, 2001)	45
Figure 2.9 Schematic of the incorporation model, where 2 indicates a fluid aggregate and 1 indicates the surrounding fluid incorporating in the aggregate (Fournier et al., 1996)	51
Figure 2.10 Stretching of a fluid element and engulfment model for micromixing (Baldyga & Bourne, 1983)	52
Figure 2.11 Typical flow pattern produced by: an axial flow impeller in a baffled tank (A), a radial flow impeller in a baffled tank (B) and either an axial or radial flow impeller in an unbaffled tank (C) (Priday et al., 1999)	55
Figure 2.12 Schematic representation of particle distribution (the circles represent the turbulent eddies, while the black dots represent particles of different dimensions) (Sundaram & Collins, 1997).	59
Figure 2.13 Qualitative representation of the effect of diffusion and attrition on the critical supercooling needed to initiate nucleation in a clear solution (Mullin & Raven, 1962).	62
Figure 2.14 Summary of different possible mechanisms explaining agitation-enhanced nucleation of crystals (Liu & Rasmuson, 2013)	63

List of figures

Figure 2.15 Schematic of a microfluidic T-junction and droplet formation inside the channel (adapted from Garstecki et al., 2006)----- 67

Figure 2.16 Schematic representation of the possible recirculation flow patterns that can be observed in two-phase gas-liquid flow in capillaries; (a) $m > 0.5$, (b)(c) $m < 0.5$, where $m = (v_b - U_{mix})/v_b$ (Adapeted from Taylor, 1960). ----- 68

Figure 2.17 Schematic of liquid-liquid slug flow in a microchannel (Dore et al., 2012). ----- 69

Figure 2.18 Samples of the horizontal component of velocities inside the plug; Y is the vertical direction (parallel to the channel radius) and X is the horizontal direction (parallel to the flow direction); x_c is the axial location of the plug centre; $\Delta x \approx 24$ mm. (Dore et al., 2012). ----- 70

Figure 3.1 Simplified representation of the reaction scheme in perfect micromixing conditions and perfect segregation conditions. ----- 77

Figure 3.2 Rushton turbine used in this work (dimensions are listed in Table 3.3)----- 79

Figure 3.3 Gas sparger used in this work (dimension listed in Table 3.3) ----- 79

Figure 3.4 Glass pipette used for the acid injection for the experiments with the gas sparger (left) and Rushton turbine (right). ----- 80

Figure 3.5 Schematic of reactor configuration for the *stirring* experiments with the Rushton turbine (left) and the *bubble column* experiments with the gas sparger (right).----- 80

Figure 3.6 Segregation index versus micro-mixing time calculated according to the IEM model for the concentration set used in this work (see Table 3.1 and Table 3.2). ----- 82

Figure 3.7 Effect of acid injection time on segregation index obtained for the stirred tank (120 rpm) (left) injection point <2>, and the bubble column (1 l/min) (right), injection point <2>. ----- 83

Figure 3.8 Decrease of segregation index X_S (calculated from absorbance measurements) due to iodine stripping over time (injection position <2>); measurements are taken at various times after the end of the acid injection while the solution was sparged continuously.----- 84

Figure 3.9 Micromixedness ratio α versus stirrer speed N obtained for measuring position <1> (R^2 of linear fitting 0.98) and <2> (R^2 of linear fitting 0.98). ----- 85

List of figures

Figure 3.10 Micromixing time as function of the stirrer speed (left) and the average energy dissipation (right) for position <1> (R^2 of fitting 0.98) and <2> (R^2 of fitting 0.98); the corresponding standard deviations are reported as error bars.-----	86
Figure 3.11 Local energy dissipation versus stirring speed at position <1> and <2>. -----	87
Figure 3.12 Non-dimensional energy dissipation rate, $\varphi T = \varepsilon T \varepsilon T$ at position <1> and <2> as function of the stirring speed N (left) and average energy dissipation εT (right). -----	89
Figure 3.13 Micromixedness ratio α versus gas flow rate calculated for position <1> and <2>. -----	89
Figure 3.14 Micromixing time versus gas flow (left) and average energy dissipation εG (right) rate calculated for position <1> and <2>. -----	90
Figure 3.15 Local energy dissipation rate versus gas flow rate for position <1> and position <2>. -----	91
Figure 3.16 Non-dimensional energy dissipation rate, $\varphi G = \varepsilon G \varepsilon G$ at position <1> and <2> as function of gas flow rate (left) and average energy dissipation (right)-----	92
Figure 3.17 Micromixing time versus specific power input at feed position <1> (left) and <2> (right) for the bubble column (G) and the stirred tank (T). -----	93
Figure 3.18 Local energy dissipation rate versus average energy dissipation rate at feed position <1> (left) and <2> (right) for the bubble column (G) and the stirred tank (T). -----	94
Figure 4.1 Para-amino benzoic acid (PABA) structure -----	98
Figure 4.2 α (left) and β (right) para-amino benzoic acid (Gracin & Rasmuson, 2004; Sullivan & Davey, 2015) -----	98
Figure 4.3 Reactor configuration for the crystallization experiments in the stirred tank (left) and bubble column (right); internal cylinder height is 200 mm. -----	100
Figure 4.4 Electrical conductivity ($\mu S/cm$) of para-amino benzoic acid aqueous solution as function of temperature ($^{\circ}C$) and concentration (R^2 of fittings > 0.99); solution concentrations are reported in the legend as mg of PABA per ml of water. -----	102
Figure 4.5 Qualitative trend of measured conductivity vs solution temperature (left), qualitative trend of solution concentration vs temperature calculated from the conductivity measurements using equation (4.1) -----	104
Figure 4.6 An example of the temperature profile of the solution during the cooling crystallization experiments measured for the highest and lowest stirring speed and highest	

List of figures

and lowest gas flow rate used in this work; the slope of the best linear fit represents the experimental cooling rate and it is reported at the bottom of each curve (R^2 of fitting > 0.99). -----	105
Figure 4.7 Solution concentration, in mg of PABA per ml of water (left), and supersaturation (right) vs temperature for the cooling crystallization experiments performed in the stirred tank for various stirring rates. -----	106
Figure 4.8 Batch reactor containing: clear, uncrystallised solution (left); crystallizing solution at <i>cloud point</i> (centre); crystallization solution after ~ 20% of solute has crystallized (right). -----	108
Figure 4.9 Microscope images of α -PABA crystal obtained via cooling crystallization. -----	108
Figure 4.10 Metastable zone width (left) and maximum supersaturation S_{max} (right) measured by <i>naked eye</i> and <i>conductivity meter</i> for different stirrer speeds. -----	109
Figure 4.11 Concentration profile (left) and supersaturation profile (right) vs temperature for the experiments performed in the bubble column. -----	111
Figure 4.12 Metastable zone width (left) and maximum supersaturation (right) measured by <i>naked eye</i> and <i>conductivity meter</i> for different gas flow rates. -----	111
Figure 4.13 Metastable zone width and maximum supersaturation for the <i>stirred tank</i> and <i>bubble column</i> crystallization experiments vs local maximum energy dissipation rate (left) (equations (3.20) and (3.21)), and average energy dissipation rate (right) (equations (2.64) and (2.66)) -----	114
Figure 5.1 PABA aqueous solution droplet formation (carrier phase: heptane)-----	121
Figure 5.2 Water droplet in a 1 mm I.D. PTFE channel (heptane carrier phase)-----	122
Figure 5.3 Schematic of the experimental setup used in this work for the quiescent conditions (stagnant nucleation) and flowing conditions (in-flow nucleation) experiments. -----	123
Figure 5.4 Qualitative representation of the specific supersaturation ratio profile used. -	123
Figure 5.5 PTFE tubing (IDEX, 1 mm I.D., 1.58 mm O.D.) immersed in a custom Refractive Index Matching (RIM) device filled with water; (A) side, (B) top-----	124
Figure 5.6 PTFE tubing IDEX, 1 mm I.D., 1.58 mm O.D.) immersed in a custom Refractive Index Matching (RIM) device filled with water placed under the microscope (Olympus IX50),	

List of figures

a digital camera (Leica EC3) is connected to the microscope to capture images of the droplet inside the tubing. ----- 125

Figure 5.7 Aqueous droplets containing α -PABA crystals ----- 126

Figure 5.8 Experimental probability $P_E(t_i, V, S)$ versus nucleation time t_n of α -PABA in *stagnant conditions* at different supersaturation ratios: 2.29 (A), 2.37 (B), 2.47 (C); (D) nucleation rate J determined by fitting the experimental data with equation (2.30). ---- 128

Figure 5.9 Fitting of nucleation rate equation $J(S) = A S \exp[-B/(\ln S)^2]$ (2.23) relative to the experimental data obtained from the capillary crystalliser in *stagnant conditions*, $R^2 = 0.97$. ----- 129

Figure 5.10 Experimental probability $P_E(t, V, S)$ versus the nucleation time of α -PABA in flowing conditions (moving droplets) at different supersaturation ratios 2.02 (A), 2.29 (B), 2.47(C); (D) nucleation rate J determined by fitting the experimental data with equation (2.30). ----- 131

Figure 5.11 Schematic representation of recirculation pattern inside the droplet. ----- 132

Figure 5.12 Experimental (deterministic) nucleation rates (J) obtained for α -PABA in water versus supersaturation ratio in stirred vials; each experimental point is based on 80 nucleation time measurements; fluid dynamic conditions are the same for all the experiments (adapted from Sullivan, 2015). ----- 135

Figure 5.13 Fitting of nucleation rate equation $J(S) = A S \exp[-B/(\ln S)^2]$ (2.23) relative to the experimental data obtained from the capillary crystalliser in *stagnant conditions*, R^2 of fitting = 0.96. ----- 136

Figure 5.14 Nucleation rate of α -PABA estimated from the best fit of equation (2.30) vs average shear rate; the reported values refer to the microfluidic experimental setup in stagnant conditions ($S = 2.29$), flowing conditions ($S = 2.02$) and stirred vials ($S = 1.97, 2.02$). ----- 138

Figure 6.1 Experimental setup: Perspex box and square glass capillary fitted at the bottom. ----- 143

Figure 6.2 Solubility of adipic acid in water as function of the temperature (Rossi et al., 2015). ----- 143

Figure 6.3 Experimental supersaturation profile used (gray line), metastable zone width (dashed red line) and solubility limit (blue line). ----- 145

List of figures

Figure 6.4 Schematic of the glass capillary used for the experiments; the air pocket forms a meniscus separating the gas and the liquid solution; the three locations considered for nucleation are depicted as A (gas-liquid interface), B (glass surface) and C (bulk of solution). -----	145
Figure 6.5 Temperature profile versus time at the centre of the glass channel (blue line) and the glass internal surface (green line); at t=0 temperature at the glass external surface is dropped from 30 °C to 8.8 °C.-----	146
Figure 6.6 Number of nuclei counted in the bulk of solution (A), glass surface (B) and gas-liquid interface (C) versus the nucleation time for different supersaturation; solid red lines represent the best linear fit for a selected subrange of data ($R^2 = 0.98, 0.86, 0.99$ for $S = 2.09, 2.18, 2.30$ respectively for the bulk of solution, graph A) ($R^2 = 0.86, 0.95, 0.94$ for $S = 2.09, 2.18, 2.30$ respectively for the glass surface, graph B); the slope of the fitting curves represents the stationary nucleation rate; standard deviations are reported as error bars. -----	147
Figure 6.7 Microscope images of adipic acid crystals in the glass channel at the three locations considered bulk of the solution (A), glass surface (B) and gas-liquid interface (C) as schematically shown in Figure 6.4; the gas-liquid interface is visible on the left-hand side of each image as a dark curved fringe. -----	149
Figure 6.8 Nucleation rate versus supersaturation ratio calculated as the slope of the best linear fit shown in Figure 6.6 relative to the bulk of the solution and the glass surface. --	150
Figure 6.9 Fitting of nucleation rate equation $J(S) = A S \exp[-B/(\ln S)^2]$ (equation (2.36)) ($R^2 = 0.76, 0.89$ for the bulk of the solution and the glass surface respectively). -----	150
Figure A.1 Example of iodine-triiodide absorbance spectra-----	161
Figure A.2 Solution absorbance at 460 nm ($R^2 = 0.998$). -----	163
Figure A.3 Solution absorbance at 353 nm ($R^2 = 0.998$) -----	164
Figure C.1 Comparison between the metastable zone found for the experimental conditions described in Chapter 5 and the one reported by Gracin et al. (2004) (red line); the blue dots represent the condition in which no crystals were observed; orange dot represents the condition for which crystals were observed in a few droplets; the red dots represent the conditions for which crystals were observed in more than 70% of the droplets. -----	167

List of tables

Table 3.1 Initial reactant concentrations in the buffer solution (total volume of the solution: 1.5 L).....	78
Table 3.2 Experimental parameters relative to the sulfuric acid injection (concentration is calculated based on the volume of acid injected).	78
Table 3.3 Dimensions of the equipment shown in Figure 3.2 and Figure 3.5 (all dimensions in millimetres)	81
Table 3.4 Experimental fitting parameters of equations (3.20) for the stirred tank	87
Table 3.5 Experimental fitting parameters of equation (3.21) for the bubble column.	91
Table 4.1 Solubility of α and β PABA in water (g_{PABA}/kg_{water}) (Gracin & Rasmuson, 2004). ...	99
Table 4.2 Experimental conditions for the crystallization experiments	101
Table 4.3 Fitting parameters of equation (4.1)	102
Table 5.1 Summary of the experimental parameters for the <i>stagnant</i> and <i>flowing</i> conditions experiments in the capillary crystalliser.	127
Table 5.2 Nucleation rate parameters derived from the Classical Nucleation Theory (equations (2.38)-(2.42))under stagnant conditions.....	130
Table 5.3 Summary of the experimental parameters for the experiments performed by Sullivan (2015) using a commercial stirred multiple reactor system (Crystal16®).	134
Table 5.4 Nucleation rate parameters derived from the Classical Nucleation Theory (equations (2.38)-(2.42)) based on the experimental nucleation rates of PABA in water at 20 °C obtained by Sullivan (2015).	137
Table 6.1 Summary of the experimental condition used.....	146
Table 6.2 Nucleation rate equation parameters relative to nucleation in the bulk on the solution and on the glass surface.	151
Table 6.3 Interfacial energy for heterogeneous (γ_{eff}) and homogeneous (γ) nucleation, based on equations (2.42) and (2.45)	151
Table A.1 Triiodide extinction coefficient values from literature and this work.	164
Table E.1 Segregation index X_S and micromixedness ratio α as function of the rotational stirring rate N and average energy dissipation ϵ_{av} for the stirred tank relative to POSITION <1>.....	171

List of figures

Table E.2 Micromixing time t_{μ} and local energy dissipation ϵ_G as function of rotational stirring rate N and average energy dissipation ϵ_{av} for the stirred tank relative to POSITION <1>.....	173
Table E.3 Segregation index X_S and micromixedness ratio α as function of rotational stirring rate N and average energy dissipation ϵ_{av} for the stirred tank relative to POSITION <2>... ..	174
Table E.4 Micromixing time t_{μ} and local energy dissipation ϵ_G as function of the rotational stirring rate N and average energy dissipation ϵ_{av} for the stirred tank relative to POSITION <2>.....	175
Table E.5 Segregation index X_S and micromixedness ratio α as function of gas flow rate Q and average energy dissipation ϵ_{av} for the bubble column relative to POSITION <1>.....	176
Table E.6 Micromixing time t_{μ} and local energy dissipation ϵ_G as function of gas flow rate Q and average energy dissipation ϵ_{av} for the bubble column relative to POSITION <1>.....	177
Table E.7 Segregation index X_S and micromixedness ratio α as function of gas flow rate Q and average energy dissipation ϵ_{av} for the bubble column relative to POSITION <2>.....	177
Table E.8 Micromixing time t_{μ} and local energy dissipation ϵ_G as function of gas flow rate Q and average energy dissipation ϵ_{av} for the bubble column relative to POSITION <2>.....	178
Table F.1 Metastable zone width and maximum supersaturation measured by conductivity meter for the stirred tank.....	179
Table F.2 Metastable zone width and maximum supersaturation resulting from naked eye observations for the stirred tank.....	180
Table F.3 Metastable zone width and maximum supersaturation measured by conductivity meter for the bubble column.....	181
Table F.4 Metastable zone width and maximum supersaturation resulting from naked eye observations for the bubble column.....	181
Table G.1 Experimental probability, $P_E(t,V,S)$ determined according to equation (2.31) as function of the nucleation time at different supersaturation ratios (2.29, 2.37, 2.47) in stagnant conditions (static droplets).....	182
Table G.2 Experimental probability, $P_E(t,V,S)$ determined according to equation (2.31) as function of the nucleation time at different supersaturation ratios (2.02, 2.29, 2.47) in flowing conditions (moving droplets).....	183

List of figures

Table H.1 Number of nuclei counted in the bulk of solution per mm^3 of solution as function of nucleation time at $S = 2.09$ ($T = 10^\circ\text{C}$).....	184
Table H.2 Number of nuclei counted in the bulk of solution per mm^3 of solution as function of nucleation time at $S = 2.18$ ($T = 9.5^\circ\text{C}$).....	185
Table H.3 Number of nuclei counted in the bulk of solution per mm^3 of solution as function of nucleation time at $S = 2.30$ ($T = 8.8^\circ\text{C}$).....	185
Table H.4 Number of nuclei counted on the glass surface per mm^2 as function of nucleation time at $S = 2.09$ ($T = 10^\circ\text{C}$).....	186
Table H.5 Number of nuclei counted on the glass surface per mm^2 as function of nucleation time at $S = 2.18$ ($T = 9.5^\circ\text{C}$).....	186
Table H.6 Number of nuclei counted on the glass surface per mm^2 as function of nucleation time at $S = 2.30$ ($T = 8.8^\circ\text{C}$).....	187
Table H.7 Number of nuclei counted on the gas-liquid interface per mm^2 as function of nucleation time at $S = 2.09$ ($T = 10^\circ\text{C}$).....	187
Table H.8 Number of nuclei counted on the gas-liquid interface per mm^2 as function of nucleation time at $S = 2.18$ ($T = 9.5^\circ\text{C}$).....	188
Table H.9 Number of nuclei counted on the gas-liquid interface per mm^2 as function of nucleation time at $S = 2.30$ ($T = 8.8^\circ\text{C}$).....	188

Chapter 1

INTRODUCTION

1.1 Research background

Crystallization is one of the oldest unit operations in chemical engineering and it is traditionally used to separate and purify solid crystalline materials from other phases. Thanks to its unique characteristics (relatively low energy requirements and mild process temperature and pressures) it is particularly attractive to the pharmaceutical industry to produce Active Pharmaceutical Ingredients (APIs). It is in fact reported that at present over 90% drugs are produced in crystalline form (Shekunov & York, 2000). Controlling the crystallization process is fundamental to achieve the following conditions (Shekunov & York, 2000):

- High product purity.
- Isolation of the desired polymorph.
- Narrow crystal size distribution (CSD), specific crystal mean size and crystal habit.
- High throughput (the target final concentration of the slurry is usually 8-15%_{wt}).
- A relatively short production cycle time for the crystallization, filtration and drying processes.

Very high crystal purity, small dimensions of the crystals with narrow CSD and specific polymorphic form are essential characteristics for the final crystalline product, especially in pharmaceutical applications as they influence the bioavailability of the drug as well as its shelf life. However, in industrial practice obtaining the desired product specifications whilst maintaining low operating costs often represents a challenge. The reason is related to the high complexity of the crystallization process and the many process parameters that have to be controlled in order to achieve the desired product quality. In addition, due to the lack of fundamental knowledge of the various crystallization mechanisms (uncertainty in the nucleation and growth rates, polymorphic transformations etc.), industrial process design is often long and is based on a trial and error approach.

The classification of crystallization techniques usually refers to the way in which supersaturation is generated in the solution; therefore, we can usually identify: cooling crystallization, evaporative crystallization, vacuum crystallization, antisolvent crystallization and reactive crystallization. Cooling crystallization is probably the technique most commonly adopted and consists in lowering the temperature of the solution at constant

pressure so that the solution is brought below the saturation point and nucleation becomes possible (Myerson, 1952). Due to the small volumes of production in pharmaceutical processes, crystallization is normally carried out in relatively small agitated batch reactors. Agitation of the crystallising solution is crucial as it helps maintain uniformity of temperature and concentration; however, the intensity and the source of agitation can also have profound effects on the final crystal characteristics, influencing for example their size, size distribution, and even the polymorphic form.

Controlling the product quality during the crystallization step is crucial to minimise the need for post-crystallization processes, such as milling, crushing and grinding, which can modify the crystal properties and even diminish the purity of the final drug by, for example, affecting the stability of the crystals (Mullin, 2001). In the attempt to control the product quality, seeding is often employed specifically to reduce the metastable zone width, controlling the polymorphic form and the CSD. This technique is widely employed in industry and consists in adding a small quantity of the solute in crystalline form to the supersaturated solution (if the material has more polymorphic forms, adding crystals of the target polymorph may redirect the crystallization process towards the desired form). Nevertheless, seeding adds an additional degree of complexity and has to be done with care. In particular, if the seeds are added too soon they will dissolve, while if they are added too late they will not have any effect on the crystallization process.

An alternative method to control crystallization is applying power ultrasound to the supersaturated solution. This technique, called *sonocrystallization*, has been reported as being able to drastically reduce the metastable zone width, to increase nucleation and growth rates and to have beneficial effects on CSD and crystal habit (Kordylla et al., 2008; Wohlgemuth et al., 2010a); in addition, it can be used as a method to induce nucleation of a specific polymorphic form (Llinas & Goodman, 2008). It is generally accepted that the enhancement of crystal nucleation under ultrasound irradiation is related to the presence of cavitation bubbles (Wohlgemuth et al., 2009). However, despite the number of studies present in the literature regarding this topic, the exact mechanism behind this phenomenon is still unclear.

Evidence that gas bubbles dispersed in a supersaturated solution can trigger nucleation in a clear supersaturated solution can be found since the 70s (Rhein, 1976). This effect was

attributed to the enhancement of mixing that would increase the probability of collision of the solute molecules in the fluid. The hypothesis that mixing can promote primary nucleation has been supported by several authors, but although theories have been proposed in order to explain this phenomenon (Liu & Rasmuson, 2013), the exact mechanism controlling nucleation under fluid dynamic conditions remains unclear (Forsyth et al., 2016; Jawor-Baczynska et al., 2013).

On the other hand, it has been suggested (Hem, 1967) that the enhancement of nucleation could be attributed to heterogeneous nucleation on the bubble surface. The hypothesis that a gas-liquid interface can represent a site for heterogeneous nucleation was systematically investigated by Wohlgemuth and her co-workers in a series of papers (Kleetz et al., 2016, 2017, Wohlgemuth et al., 2009, 2010b, 2010a). Their study shows that gassing crystallization has a similar effect to that observed with the use of ultrasounds (narrower MZW and CSD, reduced crystal median diameter) and seems to support the hypothesis of heterogeneous nucleation on the surface of gas bubbles, however, no direct evidence to support the hypothesis was provided.

One reason for the poor understanding of the crystallisation process under fluid dynamic conditions is that industrial crystallisers are often characterised by complex fluid dynamics and non-uniform temperature; therefore, carrying out systematic studies is difficult. Recently, there have been great advances in microfluidic technology as a means to perform fundamental studies on crystallization in well controlled fluid dynamic and supersaturation conditions. These devices allow partitioning the crystallising solution into hundreds of monodispersed droplets to which a precise temperature (and therefore supersaturation) profile can be applied. The accuracy with which it is possible to control the main parameters affecting the nucleation process (e.g. supersaturation) is the reason for the success of these devices in fundamental nucleation kinetics studies. Despite these advantages, it should be noted that microfluidic devices do not allow experiments to be performed in industrial-like conditions as the flow regime is limited to the laminar regime.

1.2 Thesis objective

In this work, I aim to advance the knowledge of the nucleation mechanism by investigating the effect of various parameters on crystal nucleation from supersaturated solution. In particular, the following specific objectives are pursued:

- ❖ To investigate the correlation between micromixing phenomena and nucleation under process conditions similar to those adopted in industrial processes.
- ❖ To investigate whether there is a correlation between energy dissipation rate and crystal nucleation in turbulent flow conditions.
- ❖ To advance the knowledge of nucleation mechanisms under specific fluid dynamic conditions by quantifying primary nucleation rate under diffusion-dominated regime, low shear rate and intense shear rate conditions.
- ❖ To investigate whether the enhancement in the nucleation rate observed when a gas is sparged in a supersaturated solution can be attributed to heterogeneous nucleation happening on the gas-liquid interface by designing a specific apparatus that allows to isolate the effect of the gas-liquid interface from other phenomena (e.g. shear rate, mixing).

1.3 Thesis outline

This thesis consists of seven chapters. Chapter 2 is divided into three sections. The first describes the fundamental theory of crystallisation with the main focus on Classical Nucleation Theory and the statistical-based approaches that can be used to estimate nucleation rates from small volume solution experiments. The second part describes the mixing mechanisms taking place at different length scales and gives an overview of the chemical methods available to study mixing at molecular level as well as the models that allow estimating the micromixing time. In addition, we described the mechanisms that can lead to collision of small particles in an agitated fluid. Finally, I discuss how agitation and fluid shear can influence crystal nucleation. The last part gives an overview of microfluidic technology and its relevance to crystal nucleation kinetics studies.

Chapter 3 focuses on the characterization of micromixing in a laboratory-scale stirred tank and bubble columns by means of the experimental approach and model described in

Chapter 1

Chapter 2. The micromixing performances of the two systems are compared with relevant literature data.

In Chapter 4, I present the values of the metastable zone width measured in a series of cooling crystallization experiments performed in a laboratory scale stirred tanks and a bubble column involving crystallization of para-amino benzoic acid in water. The results obtained in Chapter 3 are then used to find a link between micromixing and nucleation rate of para-amino benzoic acid in solution.

In Chapter 5, I present a microfluidic system which allows performing fundamental studies on primary nucleation kinetics to be performed under stagnant and flowing conditions. The nucleation kinetics are estimated through the model described in Chapter 2 and the results are analysed on the basis of the Classical Nucleation Theory. In order to expand the breadth of the study, a comparison with a similar experimental work present in the literature was performed and the published data are further analysed. This was useful to elucidate the influence of shear on primary nucleation. The experimental study presented in Chapter 5 has been published in *Chemical Engineering Research and Design*: Nappo, V., Sullivan, Davey, R., Kuhn, S., Gavriilidis, A., Mazzei, L. (2018) Effect of shear rate on primary nucleation of para-amino benzoic acid in solution under different fluid dynamic conditions. *Chemical Engineering Research and Design*, 136, 48-56. doi.org/10.1016/j.cherd.2018.04.039

In Chapter 6, we present a custom-made nucleation cell to investigate whether a gas-liquid interface can act as a site for heterogeneous nucleation in a way similar to a foreign particle in the solution. In particular, we measured the time needed to nucleate on different supports: bulk of the solution, gas-liquid interface and glass inside the nucleation cell. The nucleation rate is estimated through a linear fitting of the experimental data and the results are analysed based on Classical Nucleation Theory.

Chapter 2

LITERATURE REVIEW

2.1 Fundamentals of crystallization

Crystallization denotes the formation of a solid crystalline phase from an disordered phase. In this process, the molecules form highly ordered structures with specific optical and physical properties. It is one of the oldest unit operations and is used for purification and separation purposes both for production of fine chemicals (pharmaceuticals, proteins etc.) and for high-throughput production (sucrose, sodium chloride etc.). The word *crystallization* refers to many different processes: crystallization from melts, evaporative crystallization, antisolvent crystallization, polymeric crystallization etc. However, this work will only focus on cooling crystallization from liquid solutions.

2.1.1 Nucleation thermodynamics

Nucleation is the first fundamental step that initiates crystal formation from a solution. It involves the aggregation of solute molecules to form small solid structures, called clusters. Clusters smaller than a critical size may redissolve, while larger clusters form stable nuclei that can grow to the macroscopic size (Kashchiev & van Rosmalen, 2003). The path through which the nuclei are formed defines the nucleation mechanism. The term *primary nucleation* generally refers to a system in which nucleation occurs in the absence of any crystalline matter; primary nucleation can be *homogeneous*, if the crystallizing solution is pure (only the solvent and the solute are present), or *heterogeneous*, if the nucleation is initiated by foreign particles (Mullin, 2001).

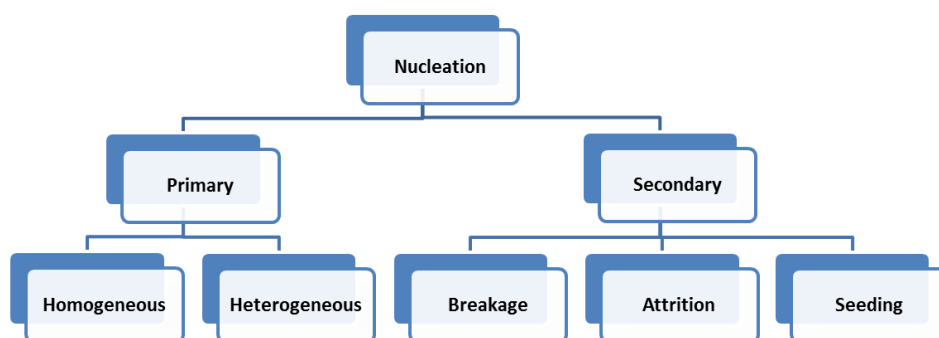


Figure 2.1 Nucleation mechanisms (adapted from Mullin, 2001)

Chapter 2

The driving force of nucleation is (Kashchiev & van Rosmalen, 2003):

$$\Delta\mu = \mu_s - \mu_c \quad (2.1)$$

where μ_s and μ_c are the chemical potentials of a molecule in the solution and in the bulk of the crystal phase respectively ($\text{m}^2 \text{ Kg s}^{-2}$). Using the thermodynamic definition $\Delta\mu$ is commonly expressed as:

$$\Delta\mu = k_B T \ln S \quad (2.2)$$

where k_B is the Boltzmann constant (approx. $1.38 \times 10^{-23} \text{ m}^2 \text{ kg s}^{-2} \text{ K}^{-1}$), T is the absolute temperature in K and S is the supersaturation ratio that for diluted binary solutions is expressed as the ratio between the actual concentration of the solution c and the equilibrium concentration c_{eq} :

$$S = \frac{c}{c_{eq}} \quad (2.3)$$

For $S < 1$, $S = 1$ or $S > 1$ the solution is said to be in undersaturated, saturated or supersaturated conditions, respectively. For $S > 1$ the equilibrium of solution is disrupted and nucleation can occur. The work associated with the formation of a cluster of n molecules is generally written as the contribution of two terms:

$$W(n) = n \Delta\mu + \Phi(n) \quad (2.4)$$

where the first term accounts for the free energy change related to the molecules aggregation, while the second term is related to the formation of the new interface between the cluster and the liquid solution. The definition of the surface term, $\Phi(n)$ depends on the nucleation mechanism, however it can be generally written as:

$$\Phi(n) = \gamma A_c \quad (2.5)$$

Chapter 2

where γ is the specific interfacial tension between the cluster and the solution (Kg s^{-2}) and A_c is the area of the cluster surface. In case of homogeneous nucleation, the cluster's shape is normally approximated to that of a sphere (Figure 2.2 a) so that A_c can be written as

$$A_c = (36\pi)^{1/3}(n v)^{2/3} \quad (2.6)$$

where n is the number of molecules in the cluster and v is the volume of a single molecule in crystalline state. Combining equations (2.2), (2.4), (2.5) and (2.6) we obtain the following expression for the work associated with the formation of a n -sized cluster

$$W(n) = -n k_B T \ln(S) + \gamma (36\pi)^{1/3}(n v)^{2/3} \quad (2.7)$$

The maximum of $W(n)$ corresponds to the energy barrier to form a critical size nucleus and can be simply obtained by setting

$$\left(\frac{dW(n)}{dn}\right)_{n=n^*} = 0 \quad (2.8)$$

where n^* is the number of molecules in a critical sized cluster. Thus, for homogeneous nucleation of a spherical cluster:

$$n^* = \frac{32\pi}{3} \left(\frac{\gamma}{k_B T \ln S}\right)^3 v^2 \quad (2.9)$$

$$W^* = \frac{16\pi}{3} \left(\frac{v}{k_B T \ln S}\right)^2 \gamma^3 = \frac{n^*}{2} k_B T \ln S \quad (2.10)$$

In case of heterogeneous nucleation, the crystalline nucleus forms on the surface of a foreign particle which acts as a sort of catalyst decreasing the energy barrier for the nucleation process. In this case, the cluster shape can be represented as a hemisphere (3D

heterogeneous nucleation, Figure 2.2 b) or as a thin disk (2D heterogeneous nucleation, Figure 2.2 c) depending on the specific crystal lattice arrangement.

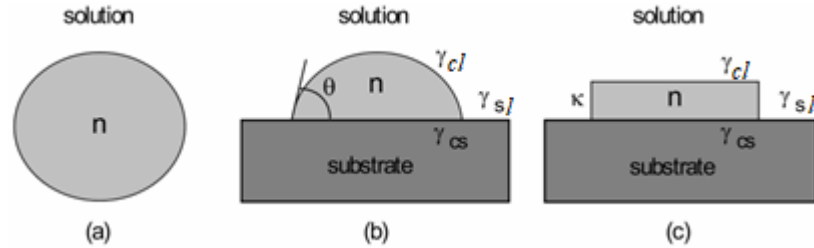


Figure 2.2 (a) Homogeneous nucleation of a spherical cluster; (b) heterogeneous nucleation of cap-shaped cluster; (c) heterogeneous nucleation of disk-shaped cluster. Adapted from (Kashchiev & van Rosmalen, 2003).

In this case, the term γ in equation (2.5) loses its physical meaning and is substituted with

$$\gamma_{ef} = \psi^{1/3}(\theta) \gamma \quad (2.11)$$

where $\psi(\theta)$ is a shape factor which is function of the contact angle, θ , between the crystalline deposit and the foreign solid surface where the heterogeneous nucleation occurs and it is given by (Volmer, 1939):

$$\psi(\theta) = \frac{(2 + \cos\theta) (1 - \cos\theta)^2}{4} \leq 1 \quad (2.12)$$

while the angle θ is a function of the interfacial tensions between the crystalline cluster, the liquid solution and the foreign particle (Figure 2.4) and it is given by Young's equation:

$$\cos \theta = \frac{\gamma_{sl} - \gamma_{cs}}{\gamma_{cl}} \quad (2.13)$$

where γ_{sl} is the solid substrate/liquid solution specific interfacial energy, γ_{cs} is the crystal/solid substrate specific interfacial energy and γ_{cl} is the crystal/liquid solution specific interfacial energy. The shape factor $\psi(\theta)$ increases with the contact angle, θ , between the forming crystal and the foreign particle (Figure 2.3). The condition θ equal to 180° (non-

Chapter 2

wetting), corresponds to the case of homogeneous nucleation, while for θ equal to 0° (wetting) the energy barrier vanishes completely. When θ lies between 0 and 180° , $\psi(\theta) < 1$; therefore:

$$W_{het} \leq W_{hom} \quad (2.14)$$

Equation (2.14) shows that the energy barrier to overcome in the case of heterogeneous nucleation is lower with respect to homogeneous nucleation, and its extent depends on the contact angle, θ , between the crystalline deposit and the foreign solid surface where the heterogeneous nucleation occurs.

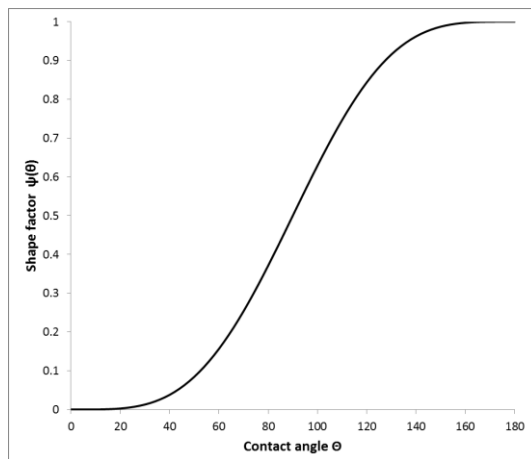


Figure 2.3 Dependence of the shape factor from the contact angle θ according to eq. (2.12).

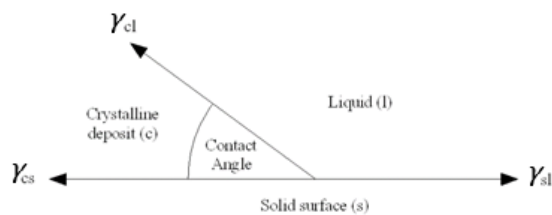


Figure 2.4 Interfacial tensions at the boundaries between three phases (two solids, one liquid), adapted from (Mullin, 2001).

In addition to the relative affinity between the forming crystal and the foreign particle, one should also consider the size and the concentration of the foreign bodies. Evidence

suggests that the optimum size of the foreign particle to initiate heterogeneous nucleation lies between 0.1 and 1 μm (Mullin, 2001).

2.1.2 Nucleation kinetics

In Classical Nucleation Theory (CNT), clusters formation is seen as a continuous process of attachment and detachment of molecules



Where C_k is a cluster of k molecules and M stands for monomer. As can be seen from equation (2.15), one of the main assumptions of Classical Nucleation Theory is that only single molecules can stick to or leave a cluster. The reason being that the concentration of molecules in solution is expected to be many orders of magnitude larger than the concentration of clusters, so the probability of collision of two clusters is considered negligible. The other fundamental assumption of CNT is that, as nucleation proceeds, the supersaturation stays constant. In practice, this means that nucleation is considered to happen in an infinite volume so an infinite number of molecules is available for the clusters formation to proceed. In general, the attachment and detachment frequencies are not constant but vary with time, however, at constant temperature and supersaturation, they can be considered time-independent. This also results in the nucleation rate being time-independent.

More recently Vekilov (2010) proposed the so-called Two-Step Nucleation Theory as an alternative to the well-established Classical Nucleation Theory. According to Vekilov's theory, fluctuations in the solution concentration can initiate the formation of a disordered liquid-like phase within the solution, solute molecules in this liquid-like phase then start to arrange themselves in a crystalline ordered way forming a sort of pre-nucleation cluster (PNC) which finally reaches a crystalline solid ordered form. However, the validity of the two-step nucleation theory is still a matter of debate within the scientific community. The classical nucleation pathway and the two-step nucleation are schematically represented in Figure 2.5.

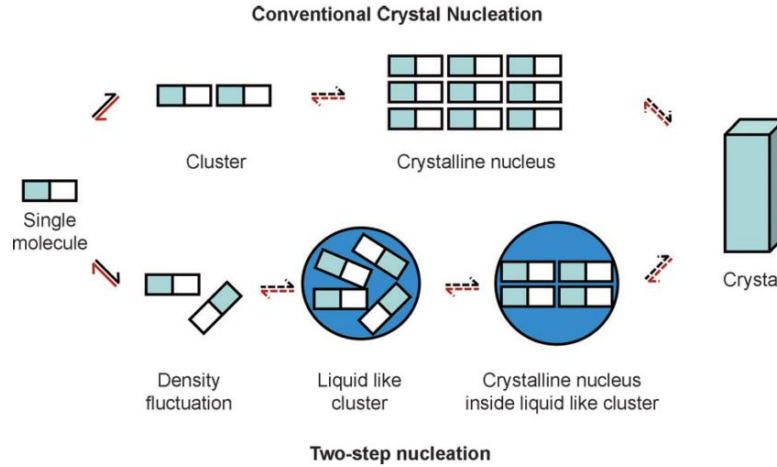


Figure 2.5 Schematic representation of the classical nucleation path-way (top) and two-step nucleation (Davey et al., 2013)

In Classical Nucleation Theory the nucleation process is treated as a sort of chemical reaction so that the nucleation rate J can be written in the well-known form (Kashchiev & van Rosmalen, 2003)

$$J = z f^* C^* \tag{ 2.16 }$$

where C^* is the equilibrium concentration of critical-sized clusters, f^* is the net frequency of attachment and z in the so-called Zeldovich factor that compensates for the assumption that the real clusters concentration in the system is different from the equilibrium concentration. In practice, z accounts for the fact that not all the nuclei that reach the critical size grow into stable crystals. In fact, they might redissolve due to Brownian motions (Kashchiev, 2000). The Zeldovich factor is only a weak function of $\Delta\mu$ and can be approximated by (Kashchiev, 2000)

$$z = \left[\frac{\left(-\frac{d^2W(n)}{dn^2} \right)_{n=n^*}}{2 \pi k_B T} \right]^{1/2} \tag{ 2.17 }$$

That, in case of homogeneous nucleation, it becomes

$$z = \left[\frac{W(n^*)}{3 \pi k_B T n^{*2}} \right]^{1/2} \quad (2.18)$$

Considering that it is reported that typically $1 < \frac{W(n^*)}{k_B T} < 80$ and $1 < n^* < 100$, then we can conclude that the Zeldovich factor is normally $0.01 < z < 1$. The equilibrium concentration of clusters follows a Boltzmann distribution

$$C^* = C_0 \exp\left(\frac{-W^*}{k_B T}\right) \quad (2.19)$$

where C_0 is the concentration of nucleation centres in the solution. In the case of homogeneous nucleation, it is equivalent to the concentration of monomers, while in the case of heterogeneous nucleation C_0 represents the concentration of possible nucleation sites. Its value generally ranges from $10^{10} - 10^{29} \text{ m}^{-3}$ depending on the nucleation mechanism (Kashchiev, 2000). The attachment frequency can take different forms depending on the controlling mechanism. In the case of homogeneous nucleation of spherical clusters, if the process is controlled by volume diffusion, f^* will depend on the diffusion flux of the monomers towards the cluster's surface; assuming that all the monomers hitting the cluster's surface incorporate to it, this approach leads to the following formula for f^* (Kashchiev & van Rosmalen, 2003)

$$f^* = (48 \pi^2 \nu)^{1/3} \mathcal{D} C n^{*1/3} = (48 \pi^2 \nu)^{1/3} \mathcal{D} C_e S n^{*1/3} \quad (2.20)$$

where \mathcal{D} is the monomer diffusion coefficient, C is the monomer concentration, C_e is the solubility and S is the supersaturation. On the other hand, if the attachment process is controlled by interface transfer, then Kashchiev & van Rosmalen (2003) propose the following formula for homogeneous nucleation of spherical clusters:

$$f^* = (6 \pi^2 \nu)^{1/3} \mathcal{D} C n^{*1/3} = (6 \pi^2 \nu)^{1/3} \mathcal{D} C_e S n^{*1/3} \quad (2.21)$$

Chapter 2

It should be noted that equations (2.20) and (2.21) differ significantly from the one proposed by Mersmann (2001) for homogeneous nucleation:

$$f^* = \left(\frac{243}{16} \pi v^2 \right)^{1/3} \mathcal{D} C^{4/3} n^{*2/3} \quad (2.22)$$

Indeed, equation (2.22) shows a dependence of f^* on $C^{4/3}$ that has been criticized by Kashchiev and van Rosmalen (2003) as it is considered in contrast with the law of mass action. Although equation (2.16) is accurate and can be used for all kinds of homogeneous and heterogeneous nucleation in one-component systems, for practical purposes nucleation rate is normally approximated as

$$J(S) = A S \exp\left(\frac{-B}{\ln^2 S}\right) \quad (2.23)$$

where A and B are called respectively kinetic and thermodynamic parameter. This form of the nucleation equation is particularly convenient as we can estimate the characteristic parameters A and B without any prior knowledge about the nucleation mechanism. In contrast, the explicit forms of A and B depend on the nucleation path (homogeneous, heterogeneous, volume or interface diffusion controlled, etc.). Although the kinetic factor A may take different forms, it is expected to be always proportional to number of nucleation sites according to the above considerations about the attachment frequency (Kashchiev & van Rosmalen, 2003). In case of homogeneous volume-diffusion and interface-transfer control, for example, we have respectively (Kashchiev & van Rosmalen, 2003):

$$A = \left(\frac{k_B T}{v^2 \gamma} \right)^{1/2} \mathcal{D} C_e \ln S \quad (2.24)$$

And

$$A = \left(\frac{4 \pi}{3 v} \right)^{1/3} \left(\frac{\gamma}{k_B T} \right)^{1/2} \mathcal{D} C_e \quad (2.25)$$

It can be shown that, typically, A ranges from 10^{13} to $10^{41} \text{ m}^{-3}\text{s}^{-1}$ in case of homogeneous nucleation and from 10^8 to $10^{31} \text{ m}^{-2}\text{s}^{-1}$ for heterogeneous 3D nucleation (Kashchiev, 2000). In case of 3D heterogeneous nucleation in solution the thermodynamic parameter B is given by:

$$B = \frac{16 \pi v^2 \gamma_{ef}^3}{3 (k_B T)^3} \quad (2.26)$$

where γ_{ef} is replaced by γ in case of homogeneous nucleation. In order to be able to directly obtain the nucleation rate, one should be able to experimentally measure the number of nuclei formed in a certain volume as function of time. If we assume constant temperature and that nucleation rate is time-independent as previously discussed, then we can describe nucleation rate $J(S)$ as (Kashchiev, 2000)

$$J(S) = \frac{N(t)}{V t} \quad (2.27)$$

where N is the number of nuclei formed in the crystallizing medium in an interval of time t , V is the volume of the crystallising solution and t is the time.

2.1.3 Metastable zone

As discussed in section 2.1.1, supersaturation is the driving force of nucleation; however, we can define a critical value of supersaturation S_c at which no new crystals can form before an acceptable time lapse has passed. This critical supersaturation defines the *metastable zone width* (Figure 2.6) in which the solution can remain in an equilibrium state for an arbitrary amount of time. It should be noted that the experimental definition of the metastable zone width (MZW) depends also on the “ability” to detect the onset of crystallization and on the definition of the “acceptable time lapse”. From a practical point of view, there is no experimental technique that is able to instantaneously capture the formation of a new supernucleus because of its very small dimensions. For this reason, all the techniques currently used are based either on detecting a decrease in the

concentration of the crystallizing substance in the solution or on detecting the appearance of grown nuclei. Popular experimental techniques to measure the solute concentration are: FTIR spectroscopy, ultrasound sensor, densitometer and electrical conductivity meter (Kubota, 2008). These methods rely on the accuracy, sensitivity and response time of the instrument used. On the other hand, naked eye, Focused Beam Reflectance Measurement (FBRM), turbidity measurements and particle counter are the most widely used techniques to detect the appearance of grown nuclei in the clear solution (Kubota, 2008).

It should be pointed out that MZW also depends on the dominating nucleation mechanism and it is narrowest for secondary nucleation and wider for primary homogeneous nucleation as qualitatively shown in Figure 2.7. However, in the reality of crystallization, nucleation mechanisms often overlap, for example nuclei formed by primary nucleation may induce secondary nucleation; in this case the resulting MZW may look narrower than expected. Although MZW is very important in industrial practice as it is used to control crystal nucleation and growth, it should be noted that it can be affected by a number of parameters: cooling rate (Wohlgemuth, 2012), agitation (Sullivan, 2015) impurities (Mullin, 2001), saturation temperature, working volume. For this reason, quantitative interpretation of MZW is complicated and has to be done with care.

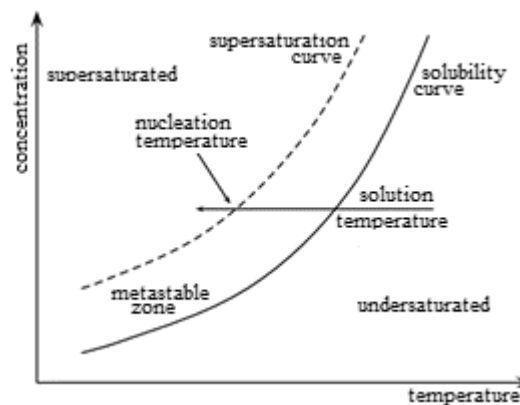


Figure 2.6 Supersaturation curve and metastable zone (Wohlgemuth, 2012).

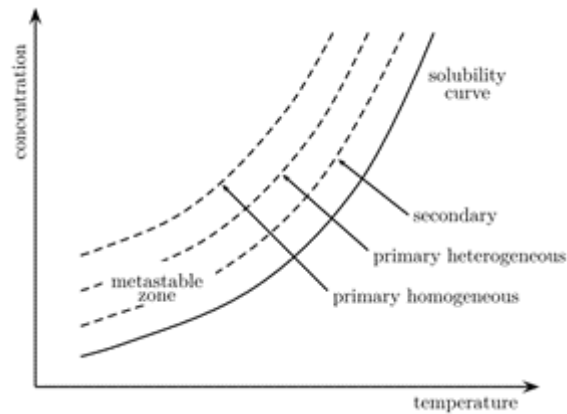


Figure 2.7 Qualitative dependence of MZW on the nucleation mechanism (Wohlgemuth, 2012).

2.1.4 Induction time

The induction time t_i is the time lapse between the instant in which the supersaturation is reached and the formation of the very first supernucleus. Conceptually, it is similar to the metastable zone width as it identifies a time interval for which the solution can stay stable and no crystals can form, for a given supersaturation level. It can be used to experimentally estimate nucleation rate by setting $N = 1$ in equation (2.27), so that (Kashchiev & van Rosmalen, 2003)

$$J(S) = \frac{1}{V t_i} \quad (2.28)$$

However, as discussed in the previous section, some time elapses between the formation of a new supernucleus and its detection, and therefore only the time t_n , that is the time needed to detect the onset of nucleation from the moment in which a specific supersaturation is achieved, can be measured experimentally. t_n is normally written as

$$t_n = t_i + t_g \quad (2.29)$$

where t_g is the time needed by the supernucleus to grow to a detectable size and it is generally unknown. It is worth noticing that t_i , that is the time needed to form the first

stable nucleus under the specific experimental conditions, is an intrinsic property of the system and therefore depends only on the supersaturation level and the specific system investigated, while t_g and t_n depend on the equipment used and the experimentalist.

2.1.5 Stochastic model of nucleation

Although nucleation is intrinsically a stochastic process, when large solution volumes are considered (as in the case of industrial and most laboratory scale batch crystallisers), nucleation rate appears to be an exclusive function of supersaturation and therefore can be modelled using a deterministic approach. As a consequence, for a given supersaturation level, the resulting experimental nucleation rate represents the mean number of nuclei formed per unit volume per unit time. However, when the crystallising volume is very small, the nucleation process appears stochastic and has to be described in terms of probability; in this case, a large number of independent, small-volume experiments is needed to obtain information about nucleation kinetics. The exact solution volume at which the nucleation process can no longer be described using deterministic models depends on the particular system studied (solvent and solute) and on the experimental conditions (supersaturation, temperature etc.), however, in the scientific research, volumes ranging from a few nanolitres (Sébastien Teychené & Biscans, 2011) up to 1 ml (Sullivan et al., 2014) have been used for these kind of studies. Despite its apparent complexity (large number of experiments needed, non-deterministic model), performing nucleation kinetics studies using a statistical modelling approach instead of traditional methods (large batch crystallisers), offers several advantages: thanks to the small volumes it is in fact possible to change the fluid temperature, and therefore the supersaturation, far more rapidly than in large-scale systems. The ability to effectively control the supersaturation in a uniform, rapid way allows in fact to apply specific supersaturation profiles to decouple the two steps of the crystallization process: nucleation and growth. It is reported that this approach, called *double pulse technique*, may also lead to a more accurate estimation of primary nucleation rate by decreasing the experimental uncertainty (Galkin & Vekilov, 1999).

In the last decades, there has been an increasing interest in microfluidic devices as they represent effective tools to perform fundamental studies on nucleation kinetics in well-

controlled conditions using the statistical modelling approach (Leng & Salmon, 2009; Rossi et al., 2015). In particular, two-phase flow can be used in these devices in order to produce and store hundreds or thousands of monodispersed droplets of the crystallising solution. Each droplet will then represent a single, independent small-volume experiment that can be used for the statistical modelling of the nucleation rate. This technique, called *droplet method*, is particularly convenient when one is interested in estimating the primary nucleation rate because, thanks to the small volume of each droplet (nl to μ l), it is possible to achieve temperature and concentration uniformity of the solution without the help of a stirrer. Finally, it is reported that the droplet method may potentially lead to a more accurate estimation of homogeneous nucleation if the number of droplets is larger than the impurities initially present in the solution (Laval et al., 2007).

In the literature (Jiang & Ter Horst, 2011; Laval et al., 2007; Rossi et al., 2015), it is suggested that nucleation rate in small volumes can be modelled using Poisson distribution, where the probability P_T to form at least one stable nucleus in a volume V during a time t at a certain supersaturation S is

$$P_T(t_i, V, S) = 1 - \exp(-J(S) V (t_n - t_g)) \quad (2.30)$$

where P_T is the probability, $J(S)$ is the deterministic nucleation rate at constant temperature, V is the solution volume, t_i is the induction time, t_g is the growth time, intended as the time the crystal nuclei need to reach a detectable size, t_n is the nucleation time and S is the supersaturation ratio. As discussed in section 2.1.4, t_i is the time needed to form the first stable nucleus from the moment the desired supersaturation level is achieved, while t_g is the time needed by the nuclei to reach a detectable size, and t_n represents the time lapse between the moment the desired supersaturation is achieved and the moment in which one is able to detect the first crystal. As a consequence, we are not able to experimentally measure t_i , but it has to be calculated from t_n and t_g . Experimentally, the probability distribution is calculated as the fraction of droplets that have nucleated after a time t_i

$$P_E(t_i, V, S) = \frac{M^+(t_n, V, S)}{M} \quad (2.31)$$

Where P_E is the experimental probability, M is the total number of droplets, and M^+ is the number of droplets containing at least one crystal at time t . By fitting the experimental data (equation (2.31)) with the theoretical distribution (equation (2.30)) it is possible to estimate the value of the nucleation rate for a given supersaturation level. Experimentally, we may adopt two strategies to determine nucleation rate using the above described methodology (statistical model based on Poisson distribution, equation (2.30)): we may set the nucleation time t_n a priori and apply a double pulse temperature profile, that consists in keeping the solution at a certain temperature, to which correspond a certain supersaturation level, for a time equal to t_n , and then raising the temperature until the solution enters the MZW to allow the growth of the formed nuclei; alternatively we may perform the experiment maintaining a single level of supersaturation and measure t_n as the time needed to detect the onset of nucleation. For the reasons discussed above (easiness to rapidly change the temperature of the solution), the first approach is mainly used with microfluidic devices (*droplet method*).

When the volume of the solution is small enough (e.g. droplets, vials), nucleation is considered to happen by the so-called *Mononuclear Nucleation Mechanism* (MNM). This mechanism assumes that growth rate is much faster than nucleation so the nucleation event is marked by the formation of the first stable nucleus that then grows until reaching a detectable size. Multiple crystals, however, can still be present due to secondary nucleation. In reverse, the *Polynuclear Nucleation Mechanism* (PNM) assumes that the time needed for the crystal to reach a detectable size is comparable with the time needed to form new stable nuclei; the result is that multiple nuclei are formed simultaneously in the solution. This model is normally used for larger volumes where nucleation rate is considered deterministic and volume-independent. The droplet method, briefly described above, is also used to effectively study polymorphism and explore new polymorphic forms; this is possible because when nucleation occurs via Mononuclear Nucleation Mechanism, as in the case of small droplets, polymorphic transformation is hindered so metastable forms can survive long enough to be detected (Leng & Salmon, 2009). For the above

Chapter 2

considerations, the limit for the applicability of the mononuclear mechanism should be set as

$$t_n^{mean} \gg t_g \quad (2.32)$$

where t_n^{mean} is the average induction time given by

$$t_n^{mean} = \frac{1}{VJ(S)} \quad (2.33)$$

and t_g is the time needed to reach a detectable size given by

$$t_g = \frac{(V_m)^{1/3}}{G} \quad (2.34)$$

where V_m is the volume fraction of crystals and G is the growth rate (m/s). It is worth noticing that equation (2.33) is obtained by substituting 1 to N in equation (2.28) to reflect the formation of the first nucleus in solution. Substituting equation (2.33) and (2.34) into equation (2.32) and defining α_v as the volume fraction of crystal to the total volume ($\alpha_v = V_m/V$) we obtain the criterion for Mononuclear Nucleation Mechanism applicability as (Kashchiev, 2000)

$$\frac{1}{VJ(S)} \ll \frac{(\alpha_v V)^{1/3}}{G} \quad (2.35)$$

As discussed in par. 2.1.2, the nucleation rate can be written as a function of three parameters: supersaturation S , a kinetic parameter A and a thermodynamic parameter B . We can rewrite nucleation rate equation derived from Classical Nucleation Theory (equation (2.23)) in the following form

$$\ln\left(\frac{J}{S}\right) = \ln A - B \cdot \frac{1}{\ln^2 S} \quad (2.36)$$

Equation (2.36) represents a linear equation with variables

$$y \equiv \ln \left(\frac{I}{S} \right) \qquad x \equiv \frac{1}{\ln^2 S}$$

So that

$$y = \ln A - B \cdot x \qquad (2.37)$$

By doing a linear fitting of the experimental data (equation (2.31)) with the theoretical distribution (equation (2.30)), we can estimate the values of the parameters A and B as the intercept and slope, respectively. The parameters A and B can be used to determine other important variables that describe the nucleation process such as the critical nucleus size n^* , the nucleation work W , the Zeldovich factor z , the attachment frequency f^* and the interfacial energy. Combining equation (2.34) with the equations from Classical Nucleation Theory (section 2.1.2) we obtain the following equations

$$n^* = \frac{2 B}{\ln^3 S} \qquad (2.38)$$

$$W(n^*) = \frac{1}{2} n^* k_B T \ln S \qquad (2.39)$$

$$z = \left[\frac{W(n^*)}{3 \pi k_B T n^{*2}} \right]^{1/2} \qquad (2.40)$$

$$f^* C_0 = \frac{A S}{z} \qquad (2.41)$$

$$\gamma_{ef} = k_B T \left[\frac{3 B}{16 \pi v^2} \right]^{1/3} \qquad (2.42)$$

While the corresponding interfacial energy for homogeneous nucleation can be calculated according to (Mersmann, 2001)

$$\gamma = \frac{0.514 k_B T}{v^{2/3}} \ln \left(\frac{1}{N_a v c_e} \right) \quad (2.43)$$

where the constant 0.514 is valid for a spherical nucleus and N_a is the Avogadro's number (about $6,022 \times 10^{23} \text{ mol}^{-1}$).

2.1.6 Secondary nucleation

When the solution already contains crystals of the solute, formation of new nuclei is possible at a relatively low supersaturation level when compared to the case in which the solution is clear (no crystalline material present). This phenomenon is called *secondary nucleation* and might occur following various mechanisms: crystals of the solute can be deliberately added to the solution (*seeding*), or it might arise from crystals fragmentation (*contact nucleation*). Seeding is often used in the industrial practice with the aim of obtaining a narrow crystal size distribution and to control the polymorphic form; however, it is reported that only crystals larger than a certain critical size are able to trigger secondary nucleation (Mullin, 2001). On the other hand, contact nucleation might occur due to crystal breakage caused by the crystals impacting the agitator or other solid surfaces inside the crystalliser, or by crystal-crystal attrition (Mullin, 2001). Depending on the crystalliser geometry, operating conditions, supersaturation level and solute-solvent properties, various approaches have been proposed in the literature to account for secondary nucleation, which mainly consist in adding extra terms to the classical primary nucleation rate equation (Mersmann, 2001).

2.1.7 Crystal growth

When a nucleus in solution has reached its critical size, it will start growing to a macroscopic size. The rate at which the crystal increases its size is called *growth rate* and

mainly depends on the supersaturation level. Between the various mechanisms proposed in the literature to describe the growth process, the most widely accepted is the *diffusion-reaction mechanism*. According to this mechanism, growth can be seen as consisting of two steps: i) diffusion, during which molecules of solute diffuse towards the crystal's surface and ii) reaction, which is the integration of the solute molecule into the crystal lattice. The diffusion step occurs through the stagnant film surrounding the crystal (its thickness is not expected to exceed 100 Å) under the driving force $(c - c_i)$, while the integration step occurs according to the r_i -order reaction under the driving force $(c_i - c^*)$. According to this model the two steps of the growth mechanism can be described by the following equations:

$$\text{i) } \quad \frac{dm}{dt} = k_d A_c (c - c_i) \quad (2.44)$$

$$\text{ii) } \quad \frac{dm}{dt} = k_r A_c (c_i - c^*) \quad (2.45)$$

where (dm/dt) is the mass flux of the solute molecules towards the crystal surface, c is the solute concentration in the bulk of the solution, c_i is the solute concentration at the boundary of the stagnant film surrounding the solution, c^* is the equilibrium concentration at the crystal interface, k_d is the diffusion mass transfer coefficient, k_r is the reaction rate of the integration process. A schematic representation of this mechanism is depicted in Figure 2.8. Usually, the crystal growth rate is limited by one of the two steps described above. If the growth rate is limited by the diffusion of the solute molecules towards the crystal surface then crystal growth is *volume-diffusion controlled*, while if the incorporation of the solute molecule into the lattice is the limiting step the growth process is *surface-integration controlled*. The limiting step is determined not only by the crystal properties but also by the particular solvent (Augustijns & Brewster, 2007).

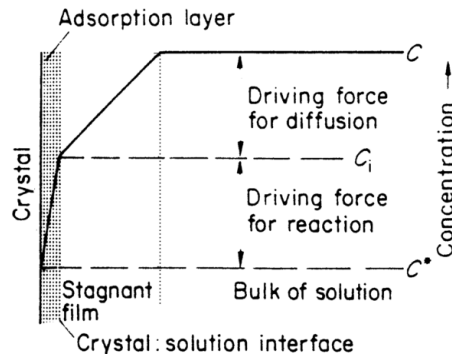


Figure 2.8 Concentration driving forces in crystal growth in solution according to the diffusion-reaction model (Mullin, 2001)

For practical purposes, we tend to combine equations (2.44) and (2.45) to obtain equation (2.46)

$$\frac{dm}{dt} = K_G A_c (c - c^*)^{g_i} \quad (2.46)$$

where K_G is the overall crystal growth coefficient and g_i is the overall order of the crystal growth process. Equation (2.46) is used in practice to model the growth of crystals in supersaturated solutions.

2.1.8 Crystal breakage and crystal agglomeration

Crystal size and size distribution is not only affected by nucleation and growth but also by other mechanisms, such as *crystal breakage* and *crystal agglomeration*, *aggregation* and *flocculation*. In case of aggregation or flocculation, crystals are kept together by weak forces, like van der Waals forces; due to the labile nature of these bonds, aggregates and flocculates can be easily destroyed. In the case of agglomerates, crystals are kept together by stronger forces (e.g. crystalline bridges), therefore they are much more difficult to destroy without affecting the crystals shape or size. Agglomeration is only possible in supersaturated solutions and can arise as a consequence of malgrowth of crystals (*primary agglomeration*), or as a result of crystal-crystal collision (*secondary agglomeration*); however, it is difficult to distinguish between aggregates originated by these two mechanisms just by microscopic observations. *Secondary agglomeration* is normally

expected to take place only for particles smaller than a certain critical size (micron range) (Mullin, 2001).

Crystal breakage in an agitated crystalliser is mainly due to crystal-crystal attrition or crystal-agitator attrition and is one of the causes of secondary nucleation; the number and the size of the crystals resulting from the breakage process depends obviously on the energy of the impact and the crystal characteristics (size, shape etc.). Various models have been proposed in the literature to account for the effect of crystal attrition and breakage; however, their discussion is beyond the scope of this work.

2.2 Fundamentals of mixing

2.2.1 Mixing time scales

Mixing is a very complex process that acts at different scales. According to the scale considered, one can talk about macro, meso or micro mixing. Chemical reaction and crystal nucleation are molecular-scale processes and for this reason they can only be influenced by what happens at the molecular level (McLeod et al., 2010). Macromixing describes the motion of large scale fluid packets generated by the fluid flow, it represents the mixing process at the largest possible scale, i.e. reactor scale. Macromixing can be estimated relatively easily by adding a tracer to the fluid and measuring the time needed to disperse it. This can be done for example using a dye and measuring how quickly the colour of the fluid becomes spatially uniform again, or adding a substance with different pH or temperature and monitoring the pH/temperature fluctuations: when the fluctuations fall below a set value (usually $\leq 5\%$) then the system is considered homogeneous again and the time lapse between the tracer injection and the end of fluctuations can be taken as the macromixing time.

Usually, in agitated tanks, the macromixing time is taken as 3 to 5 time the circulation time. Circulation time depends of course on the impeller type and reactor configuration, however for a Rushton turbine can be roughly estimated as (Espuny Garcia del Real et al., 2014):

$$\tau_c = \frac{0.85}{N} \left(\frac{D}{d} \right)^2 \quad (2.47)$$

where τ_c is the circulation time, D is the tank diameter, d is the impeller diameter and N is the rotational rate of the impeller, in s^{-1} . Macromixing also influences the meso and micro mixing by transporting fluid packets in different position of the reactor, where they can experience different fluid dynamic conditions. Macromixing influence over mixing at smaller scales (meso and micro) becomes more relevant as the fluid dynamic conditions in the reactor become less uniform. Because of its nature, the specific definition of macromixing depends on the dimension of the reactor and the agitation system used.

Mesomixing describes mixing at a scale much larger than the molecular scale but significantly finer than the reactor scale. It induces the breakup of large eddies into smaller eddies due to inertial-convective forces, and it is responsible for plume dispersion in processes such as anti-solvent crystallization, where a solvent is injected in the fluid through a feed pipe. Mesomixing time can vary over many orders of magnitude, depending on the local fluid dynamic conditions. It does not directly affect mixing at molecular level, however, as macroscopic mixing, it could have an indirect influence by changing the environmental conditions of the smallest eddies. The dispersion time of a plume in a turbulent environment can be estimated by (Baladyga & Pohorecki, 1995)

$$\tau_p = \frac{Q_p}{u_t \mathcal{D}_t} \quad (2.48)$$

where Q_p is the feed rate, u_t is the velocity of the bulk fluid at the feed point, and \mathcal{D}_t is the diffusivity in turbulent conditions that can be calculated as (Baladyga & Bourne, 1999)

$$\mathcal{D}_t = 5.84 \times 10^{-3} \varepsilon^{1/3} d^{4/3} \quad (2.49)$$

where ε is the local energy dissipation rate (W/kg) and will be discussed later in this chapter, and d is the impeller diameter.

Micromixing describes the mixing process at the smallest possible scale, i.e. molecular scale. At high Reynolds numbers, the fluid flow can no longer be considered as an ordered motion of molecules but it breaks up forming a number of eddies of various dimensions.

Chapter 2

According to the theory of turbulence, the large eddies transfer their kinetic energy to the smaller eddies in an energy cascade; the energy that reaches the smallest eddies, where the viscous forces are dominant, is then dissipated into heat. The characteristic length scale of the smallest possible eddies is called Kolmogorov length scale. The dimension of the energy dissipating eddy is

$$\eta = \left(\frac{\nu^3}{\varepsilon} \right)^{1/4} \quad (2.50)$$

Where η is the size of the energy dissipating eddy (m) ν is the kinematic viscosity of the fluid (m^2/s) and ε is the rate of energy dissipation (W/Kg). Turbulent micromixing refers to the stage of mixing where viscous forces become important and involves the stretching of fluid packets of scale approximately equal to the Kolmogoroff scale and the subsequent molecular diffusion within the fluid elements and with the adjacent elements.

The micromixing time t_μ can be related to the local energy dissipation rate using the Kolmogorov theory of turbulence (Assirelli et al., 2002; Bałdyga, 2016; Espuny Garcia del Real et al., 2014)

$$t_\mu = 17.24 \sqrt{\frac{\nu}{\varepsilon}} \quad (2.51)$$

where ε is the energy dissipation rate (W/kg) and ν is the kinematic viscosity (m^2/s). While the shear rate (s^{-1}) generated within the energy dissipating eddy can be estimated as (Angst et al., 1982)

$$\dot{\gamma}_T = 0.5 \left(\frac{\varepsilon}{\nu} \right)^{1/2} \quad (2.52)$$

where $\dot{\gamma}_T$ is the so-called *turbulent shear rate*, ε is the energy dissipation rate per unit mass and ν is the kinematic viscosity. Depending on the system analysed, local fluid dynamic conditions can vary a lot spatially, as a consequence, local energy dissipation rate and turbulent shear rate can exhibit a strong dependence on the position in which is measured.

For example, it is reported in the literature that stirred tanks are quite anisotropic from the point of view of local fluid dynamic conditions, therefore the local energy dissipation rates can differ from the average values up to 2 order of magnitude (Assirelli et al., 2002; Espuny Garcia del Real et al., 2014).

In laminar flow, eddies and whorls are of course not present, but micromixing is still possible. In this case, however, micromixing is typically much slower than in turbulent conditions as it essentially relies on the diffusion across the interface of the stretching fluid lamellae. In order to improve micromixing in devices that operate in laminar flow (microreactors, micromixers etc.), chaotic flow is usually employed; however, this is beyond the aim of this work.

2.2.2 Micromixing characterization through chemical reaction methods

Micromixing can be estimated experimentally using chemical methods since physical methods are shown not to be accurate enough (Monnier et al., 1999a). In particular, one could use consecutive–competing reactions



or parallel– competing reactions



Where reaction (i) is considered to be instantaneous with respect to (ii). In order to obtain micromixing information using one of the above reaction schemes, typically a solution containing all the reactants except *B* is prepared, and then species *B* is introduced in a selected point of the reactor. Because the reaction schemes include two competing reactions then the product distribution will depend on the local micromixing condition at the injection point. In particular, reaction (i) can be regarded as instantaneous with respect to (ii), therefore if the feed plume containing *B* is dispersed instantaneously only *R* will be

formed. In contrast, if micromixing is not instantaneous, a certain amount of B can react to from S. The result is that the yield of S will depend on the degree of mixing of the reactants: the better the micromixing the less S will form. The most common reaction schemes for micromixing characterization are the iodate/iodate method, first introduced by Villermaux et al. (1994), and the *Bourne reactions*, developed by Bourne and his co-workers (Bourne & Yu, 1994; Kozicki et al., 1981). Although these chemical methods are relatively easy to use, they only give information about the product distribution of the reactions and can be used to compare the segregation level of different systems only when the exact same experimental procedure is used; while quantitative interpretation of the results in terms of micromixing time and local specific energy dissipation relies on modelling of the reaction and mixing progression. Different models to estimate the micromixing time will be presented in the following section.

2.2.3 Micromixing models

The reaction schemes presented above can provide information about micromixing performance based on the reaction product distribution obtained. However, the specific product distribution obtained experimentally is strictly linked to the reactants concentration chosen; therefore, comparing micromixing performance of different systems with literature data might be difficult. For this reason, usually, the micromixing process is modelled in order to extract the *micromixing time* t_μ which is of course independent of the particular experimental procedure employed. For this purpose, different models have been proposed in the literature. Between them, the most used are: the IEM model (*InterExchange with the Mean*), the *Incorporation model* and the EDD model (*Engulfment Deformation Diffusion*) (Monnier et al., 1999a). In this work, we used the IEM model, however, a brief overview of all three methods is provided below. It should be noted that the micromixing times derived from the models are local estimates. Consequently, the energy dissipation rate ε calculated from equation (2.51) refers to the local fluid dynamic conditions as well.

2.2.3.1 Incorporation model

The Incorporation model proposed by Fournier et al. (1996) assumes the presence of two fluids into the system, where one fluid (fluid 2 in Figure 2.9) is broken down into smaller aggregates and starts growing by incorporating the surrounding fluid (fluid 1 in Figure 2.9).

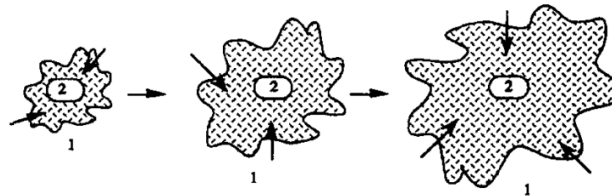


Figure 2.9 Schematic of the incorporation model, where 2 indicates a fluid aggregate and 1 indicates the surrounding fluid incorporating in the aggregate (Fournier et al., 1996)

The growing process is described according to the following equation (Guichardon & Falk, 2000)

$$g(t) = \frac{v(t)}{v_0} \exp\left(\frac{t}{t_\mu}\right) \quad (2.53)$$

where $g(t)$ is the incorporation function, $v(t)$ is the volume of the growing aggregate at time t , v_0 is the volume of the aggregate at $t = 0$. Equation (2.53) shows that the micromixing time t_μ is assumed to be equal to the “incorporation time”. By applying this method and solving the mass balance, it is normally found that the micromixing time t_μ depends on the micromixedness ratio according to

$$t_\mu \propto \alpha^{-p} \quad (2.54)$$

where the proportionality constant and the exponent p are function of the reactants' concentration and α is the micromixedness ratio, which is function of the reaction product distribution and will be further discussed later. The relation above is only valid for small ranges of α .

2.2.3.2 Engulfment Deformation Diffusion Model

The Engulfment Deformation Diffusion model, first proposed by Baldyga & Bourne (1983), describes the micromixing process into three steps:

- *Deformation*: a fluid element approximately equal to the Kolmogorov scale is deformed and elongated as a result of shear;
- *Engulfment*: envelopment of one fluid layer with another due to vorticity;
- *Diffusion*: molecular diffusion between the two fluid elements;

Figure 2.10 schematically shows the EDD model: due to the viscous-convective forces, a fluid element rich in species B that is in an environment rich in species A, stretches in a certain direction while thinning in a perpendicular direction (Figure 2.10, t1), then the slab formed starts to rotate due to velocity fluctuations (Figure 2.10, t2) causing the engulfment of A (Figure 2.10, t3), then diffusion takes place and the process is repeated in another direction (Figure 2.10, t4, t5, t6).

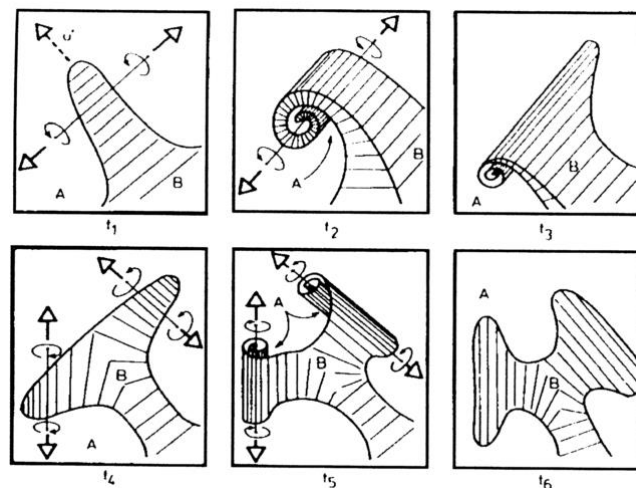


Figure 2.10 Stretching of a fluid element and engulfment model for micromixing (Baldyga & Bourne, 1983)

This model is quite complex, however, in a paper published in 1989 (Baldyga & Bourne, 1989), the authors showed that for Schmidt number $Sc \ll 4000$ engulfment is the limiting step, so they modified the EDD model in a way that only the engulfment step is considered. The modified model is called the *Engulfment model* (E model). In the E model, the growth of a fluid element due to engulfment can be described as

$$\frac{dV_{ei}}{dt} = E V_{ei} \quad (2.55)$$

where V_{ei} is the volume of the fluid element, t is the time and E is the engulfment rate (s^{-1}) that can be calculated as (Baldyga & Bourne, 1989)

$$E = \frac{\ln(2)}{12} \left(\frac{\varepsilon}{\nu} \right)^{1/2} \quad (2.56)$$

where ε is the local specific energy dissipation (W/kg) and ν is the kinematic viscosity (m^2/s). Assuming that the diffusion inside the fluid element is much faster than the engulfment, then the mass balance for species i within the growing-reaction area reads

$$\frac{dV_{ei}c_i}{dt} = E V_{ei} \langle c_i \rangle + R_i V_{ei} \quad (2.57)$$

where c_i and $\langle c_i \rangle$ is the instantaneous concentration of species i in the reaction zone and the surroundings near the reaction zone respectively, R_i is the reaction rate referred to component i . By combining equation (2.55) and (2.57) we obtain

$$\frac{dc_i}{dt} = E (\langle c_i \rangle - c_i) + R_i \quad (2.58)$$

which is the constitutive equation of the E model. The solution of the above equation gives the micromixing time associated with a certain product distribution.

2.2.3.3 InterExchange with the Mean model

Villermaux and his co-workers developed a relatively simple model for micromixing characterization which is called the InterExchange with the Mean (IEM) (Rousseaux et al., 1999). This model assumes that the fluid is divided into two volumes and mixing proceeds by mass exchange between the two fluid compartments. The change in concentration of

each chemical species within each compartment can be described by equations (2.59) and (2.60):

$$\frac{dc_{i,1}}{dt} = \frac{\langle c_i \rangle - c_{i,1}}{t_\mu} + R_{i,1} \quad (2.59)$$

$$\frac{dc_{i,2}}{dt} = \frac{\langle c_i \rangle - c_{i,2}}{t_\mu} + R_{i,2} \quad (2.60)$$

where $c_{i,1}$ and $c_{i,2}$ are the concentrations of species i in compartment 1 and 2 respectively, $R_{i,1}$ and $R_{i,2}$ are the reaction rates of species i in compartment 1 and 2 respectively, $\langle c_i \rangle$ is the mean concentration of species i in the two compartments which can be calculated as:

$$\langle c_i \rangle = \alpha c_{i,1} + (1 - \alpha) c_{i,2} \quad (2.61)$$

where α is the volume fraction of fluid in compartment 1 with respect to the total. The equations presented must be solved for each component involved in the mixing process by first assuming a mixing time and then calculating the final concentrations of all the species; when this procedure is repeated for different micromixing times we obtain a correlation between the product distribution and the micromixing time.

This model will be used in Chapter 3 for the specific concentration set used in order to estimate the micromixing time from the product distribution obtained using the Villermaux-Dushman reaction system.

2.2.4 Mixing and energy dissipation in agitated vessels

In agitated vessels, fluid dynamic conditions depend strongly on the geometry of the vessel and the type of impeller used. Different kinds of impellers find different applications: axial flow impellers (e.g. propellers, pitched-blade turbine etc.) for example are normally used to achieve good solid suspension, while radial flow impellers (e.g. flat-blade impellers, disk turbine etc.) are good for gas dispersion. Figure 2.11 A and B schematically depicts the flow

pattern generated by an axial flow and radial flow impeller, respectively, in a baffled tank; while Figure 2.11 C shows the typical flow pattern produced in case of unbaffled vessels.

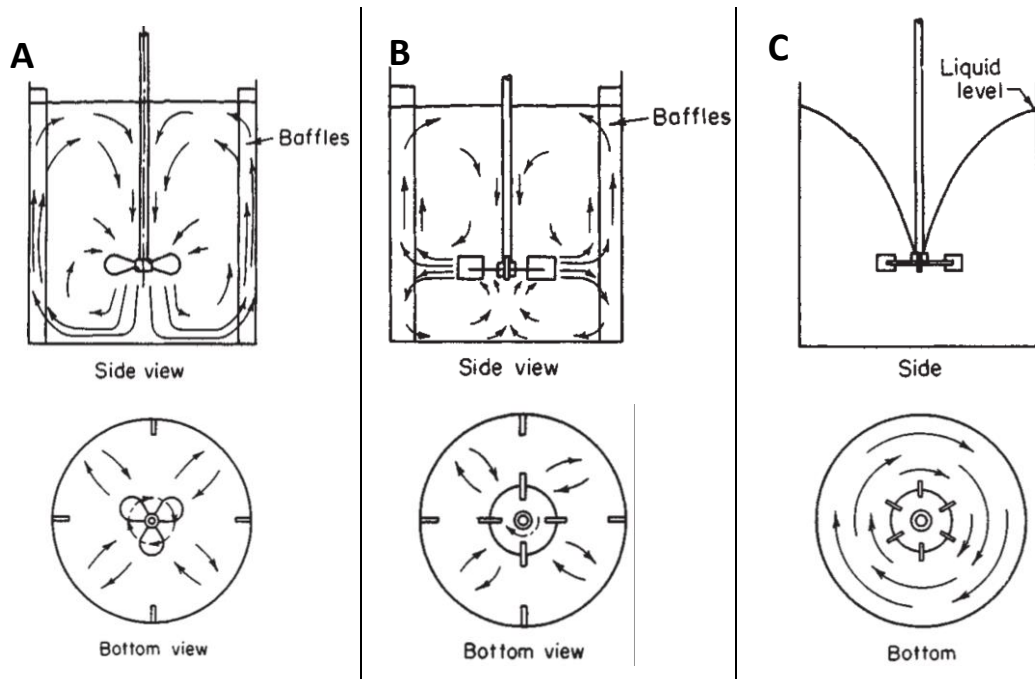


Figure 2.11 Typical flow pattern produced by: an axial flow impeller in a baffled tank (A), a radial flow impeller in a baffled tank (B) and either an axial or radial flow impeller in an unbaffled tank (C) (Priday et al., 1999)

In stirred tanks, Reynolds number is a function of the stirring rate and impeller diameter as (Priday et al., 1999)

$$Re = \frac{N d^2}{\nu} \quad (2.62)$$

where N is the stirring speed in s^{-1} , d is the impeller diameter and ν is the kinematic viscosity (m^2/s). The exact value of the Reynolds number that marks the start of the turbulent regime depends on the impeller type; for a 6-blades disk turbine in a standard configuration for example this value is approximately equal to 10^3 (Norwood & Metzner, 1960). The efficiency of the impeller in transferring energy to the fluid is normally estimated using the so-called *power number*, which represents the ratio between the

Chapter 2

power used to operate the impeller and the actual energy transferred to the fluid. In particular, the power number N_p for stirred tanks is defined as follow

$$N_p = \frac{P}{\rho N^3 d^5} \quad (2.63)$$

where P is the power input (W), ρ is the fluid density, N is the stirring rate (1/s) and d is the impeller diameter. In fully baffled conditions, the power number for Rushton turbines is normally in the range 4 – 6, depending on the system geometry. In contrast, the absence of baffles causes the formation of a vortex at the centre of the vessel where the axial velocities are almost negligible while tangential velocities are predominant; in this configuration the power number reduces to 1 – 2 (Assirelli et al., 2008; Furukawa et al., 2012; D. J. Gray et al., 1982). The power number can be either established experimentally by measuring the torque, or calculated using one of the many correlations reported in the literature (e.g. Furukawa et al., 2012). From the power input P , it is possible to calculate the average specific energy dissipation or specific power input for stirred tanks $\bar{\epsilon}_T$ according to the following relation (Assirelli et al., 2002; Fournier et al., 1996; Guichardon & Falk, 2000)

$$\bar{\epsilon}_T = \frac{P}{\rho V} \quad (2.64)$$

where P is the power input (W), ρ is the fluid density and V is the total volume of the fluid. The specific power input can be used to estimate the mixing performance as it gives an indication of the energy transferred to a unit volume of fluid; however, there is a risk to oversimplify the problem, especially in highly anisotropic systems like stirred vessels. Therefore, to have a more accurate estimation of the mixing environment, usually other techniques are used (e.g. Particle Image Velocimetry). Empirical evidence (Robertson & Ulbrecht, 1987) and theoretical reasoning (Pérez et al., 2006) show that in turbulent regime the average shear rate associated with $\bar{\epsilon}_T$ is proportional to $N^{3/2}$, where N is the rotational rate of the impeller in s^{-1} .

The ratio between the local value of the energy dissipation rate for stirred tanks ε_T (introduced in equation (2.51)) and the specific power input $\bar{\varepsilon}_T$, as defined in equation (2.64), represents the dimensionless energy dissipation rate, φ_T .

$$\varphi_T \equiv \frac{\varepsilon_T}{\bar{\varepsilon}_T} \quad (2.65)$$

This parameter represents a measure of the anisotropy of the energy dissipation rate within the system and is especially important to assess the mixing performances in different parts of the reactor with respect to the specific energy transferred to the fluid. In stirred vessels, usually its maximum value ($\varphi_{max} = \varepsilon_T^{max} / \bar{\varepsilon}_T$) is found in the trailing vortex next to the impeller, but its exact location is still a matter of discussion in the literature (Assirelli et al., 2002). The exact assessment of ε_T^{max} is quite challenging from the experimental point of view due to the great sensitivity to the measurement location. In addition, different methods (optical or chemical) may lead to slightly different results which affect the final value of φ . For this reason, a large variability is found in the literature regarding this parameter. For example, for a Rushton turbine, values ranging from 6 to 100 have been reported (Assirelli et al., 2002; Huchet et al., 2009).

2.2.5 Energy dissipation in a bubble column

The turbulence generated in a bubble column is inherently very different from what is generated in single flow and it is called *bubble induced turbulence*. The reasons for this difference mainly lie in the intermittent nature of the bubble dynamics. In particular, in single phase flow, turbulence is generated at a constant rate and only at large length scales; while turbulence at small scales arises due to the energy cascade that transfers the energy from large eddies to small eddies. In contrast, in bubble columns, turbulence is directly generated at various scales: the bubbles movement and circulation inside the reactor is responsible for the large scale turbulence (Joshi & Sharma, 1976), while the bubbles formation and the fluctuation in bubbles velocity directly generates turbulence at small scales (Alm eras et al., 2015). This results in turbulence being generated over a wide range of length scales if compared with single phase flow. It should also be noted that in single

phase flow turbulence generation is constant while the intermittent nature of the bubble generation process causes the turbulence generation being intermitted as well (Sathe et al., 2013). Because of these characteristics, bubbly flow also has the potential of being used for mixing purposes in place of traditional mixers (Alméras et al., 2015). In case of bubble columns the average energy dissipation rate due to the sparged gas can be calculated as (Krishna & Ellenberger, 1996; Li et al., 2014)

$$\bar{\varepsilon}_G = \frac{Q_g \rho_L g H_L}{\rho_L V} \quad (2.66)$$

where Q_g is the gas flow rate, ρ_L is the liquid density, g is the gravitational constant (approx. 9.81 m/s^2), H_L is the liquid height above the gas sparger and V is the volume of the liquid. In practice, $\bar{\varepsilon}_G$ (W/kg) represents the energy to raise a mass of water corresponding to $Q_g \rho_L$ through a height H_L . Similar to the case of the stirred tank, we can define the dimensionless energy dissipation rate φ_G as the ratio between the local energy dissipation rate ε_G and the specific power input $\bar{\varepsilon}_G$.

$$\varphi_G \equiv \frac{\varepsilon_G}{\bar{\varepsilon}_G} \quad (2.67)$$

$\bar{\varepsilon}_G$ and φ_G can be used to have a rough idea about the fluid dynamic conditions and the intensity of energy dissipation inside the reactor, however a more accurate assessment of the local hydrodynamic conditions is necessary to fully characterise the mixing performances of the bubble column.

2.2.6 Influence of fluid dynamics on small particles motion and aggregation

A lot of scientific research focuses on the influence of fluid dynamics and mixing on particle motion, collision and aggregation as it is of interest for many industrial and laboratory applications (e.g. multi-phase stirred reactors, bubble columns etc.). Despite the large number of studies dedicated to this topic, the complex interaction between fluid flow and particle dynamics is not well understood, especially in turbulent conditions. The way the

fluid dynamic and mixing processes influence particles motion depends greatly on the dimensions of the particles. It has in fact been reported that particles heavier than the fluid tend to move out of the eddies due to their inertia and centrifugal forces, while particles lighter than the fluid tend to follow the stream lines and remain trapped inside the eddies (Sundaram & Collins, 1997) as illustrated in Figure 2.12.

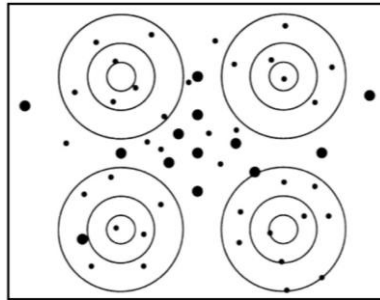


Figure 2.12 Schematic representation of particle distribution (the circles represent the turbulent eddies, while the black dots represent particles of different dimensions) (Sundaram & Collins, 1997).

Particles present in an agitated fluid collide due to their relative velocity which can be caused by different mechanisms (Liao & Lucas, 2010):

- Random motion of the particles due to turbulent fluctuations in the surrounding continuous phase;
- Mean-velocity gradients in the flow: a particle in a high velocity area may collide with a particle moving in a slower velocity region;
- Different rise velocities induced by buoyancy or body forces (this mainly applies to gas bubbles);
- Particles being captured in an eddy may collide due to turbulent shear inside the eddy;
- Wake interactions or helical/zigzag trajectories;

It is well known that particles smaller than a certain critical size closely follow the streamlines and their velocity broadly mirrors that of the fluid. For these particles, the collision process is mainly governed by turbulent shear inside the eddies and the collision frequency which can be estimated as (Liao & Lucas, 2010)

$$\omega = h (r_1 + r_2)^3 \dot{\gamma} \quad (2.68)$$

where h is a proportionality constant, r_1 and r_2 are the radii of the colliding particles and $\dot{\gamma}$ is the shear rate (1/s). For turbulent flow, the shear rate can be estimated as from equation (2.52), while the coefficient h is taken equal to 0.618 for particle smaller than the Kolmogorov length scale (equation (2.50)) and $4\pi/3\sqrt{1.61}$ for particles larger than the Kolmogorov length scale. However, equation (2.68) can be applied also in case of laminar flow, where $\dot{\gamma}$ represents the laminar shear rate and h is taken equal to 4/3 (Liao & Lucas, 2010).

It should be noted that the fluid flow has a significant effect on the particles collision frequency only for particles sufficiently large and when exceeds certain level of the shear rate. In other words, the number of collisions caused by the shear field should be at least of the same order of magnitude of those caused by Brownian motion in order to make a difference in the collision frequency. This can be estimated using the Péclet number defined in terms of shear rate as (Wagner & Brady, 2009)

$$Pe = \frac{\dot{\gamma} r^2}{\mathcal{D}} \quad (2.69)$$

Where r is the average radius of the particles, \mathcal{D} is the diffusion coefficient and $\dot{\gamma}$ is the shear rate. We can estimate the diffusion coefficient of small particles using the Stokes-Einstein equation (Edward, 1970; Wagner & Brady, 2009)

$$\mathcal{D} = \frac{k_B T}{6 \pi \mu r} \quad (2.70)$$

where k_B is the Boltzmann constant (approx. $1.38 \times 10^{-23} \text{ m}^2 \text{ kg s}^{-2} \text{ K}^{-1}$), T is the absolute temperature (K), μ is the dynamic viscosity (Pa s) of the fluid where the particles are immersed and r is the radius of the particle. For particles in the order of nanometres, the theoretical value of \mathcal{D} obtained is quite close to the experimental one.

The Péclet number is therefore a measure of the relative importance of particle dispersion caused by random Brownian motion and shear flow. For low Pe , it can be assumed that the effect of shear flow is negligible compared to that of diffusion. On the other hand, for $Pe \geq 1$ we can assume that the frequency of collision is significantly enhanced by the flow. Tanthapanichakoon et al. (2006) used a modified Péclet number to investigate laminar mixing in liquid slugs travelling in microchannels. When the slugs are motionless, mixing is controlled by molecular diffusion. When the slugs are moving, two counter-rotating vortices are generated within the slugs which cause the fluid layers to stretch and interlayer so that the diffusion distance is reduced, thereby accelerating the mixing process. Their work shows that two different mixing regimes can be encountered in the slugs: *diffusion-dominated* and *convection-dominated*. In the diffusion-dominated regime, mixing proceeds essentially by random molecular motions. On the other hand, in the convective-dominated regime, mixing is enhanced by axial dispersion in the direction of flow and interlayering. Based on these observations, the authors defined a new Peclet number Pe' as

$$Pe' = \frac{U_s d_s^2}{l_s \mathcal{D}} \quad (2.71)$$

Where U_s , d_s and l_s are the velocity, the diameter and the length of the slug respectively, and \mathcal{D} is the diffusivity. According to the authors, the Péclet number as defined in equation (2.71) can be used to distinguish between the two mixing regimes in liquid-liquid slug flow in straight channels.

2.2.7 Effect of agitation on the nucleation rate of crystals in solution

As discussed in section 2.1, the first step of crystallization is nucleation, which is the formation of a new solid crystalline phase via self-assembly of molecules in solution. As nucleation is considered a molecular-level activated process, in the literature it is suggested that mixing at molecular level can provide energy to the system to overcome this barrier and initiate nucleation (Bałdyga, 2016; McLeod et al., 2010). Evidence that mechanical perturbations in supersaturated solutions can trigger nucleation in a clear solution can indeed be found since the beginning of the 20th century; however, systematic studies about

the effect of fluid dynamics on nucleation kinetics only started in the 60s, when Mullin & Raven (1962) measured the metastable zone width (MZW) of a number of aqueous salt solutions as a function of the speed of the stirrer used to agitate them. The authors found that experimentally the MZW decreases as the agitation rate increases, reaches a minimum and then increases again. The trend found is qualitatively reported in Figure 2.13 and suggests that the critical supercooling required to initiate nucleation is a result of the combined effect of diffusion and attrition.

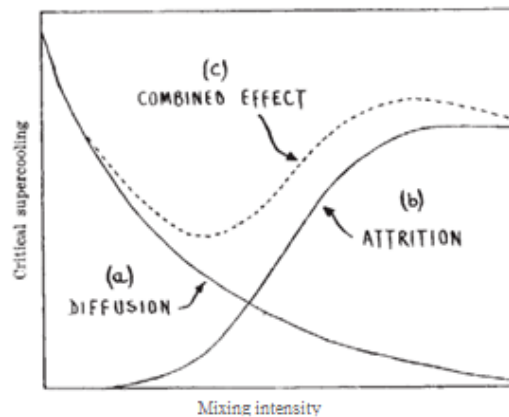


Figure 2.13 Qualitative representation of the effect of diffusion and attrition on the critical supercooling needed to initiate nucleation in a clear solution (Mullin & Raven, 1962).

This non-monotonic behaviour was more recently observed by Liu & Rasmuson (2013) and Liu et al. (2014, 2015) who performed a series of experiments to evaluate the effect of agitation on the primary nucleation rate of m-hydroxybenzoic acid and butyl paraben from organic solvents using various experimental systems such as traditional stirred crystallizers, small vials agitated with a magnetic stir bar and a Couette flow system. Their results also show that the induction time strongly depends on the fluid dynamic conditions in the system; however, no definitive relation between fluid shear and nucleation rate was found. Forsyth et al. (2015, 2016) performed similar experiments with the aim of correlating the induction time to the average shear rate in laminar conditions: their results suggest that the induction time can be significantly reduced by increasing the shear rate. To explain these results, Liu & Rasmuson (2013) proposed an interesting range of possible mechanisms:

- Molecular alignment
- Secondary nucleation
- Enhanced mass transfer
- Shear-enhanced cluster aggregation

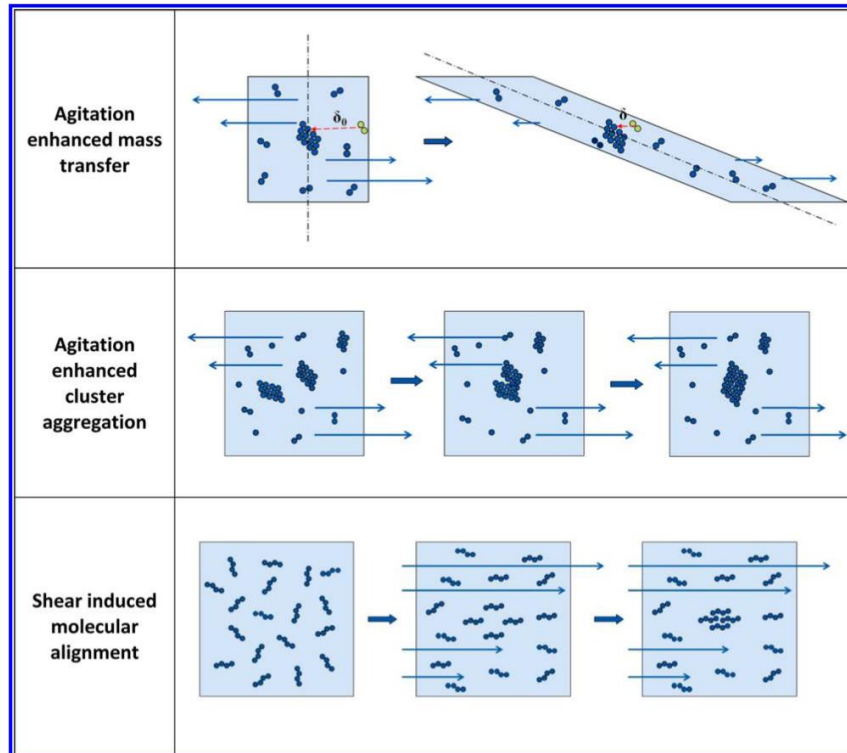


Figure 2.14 Summary of different possible mechanisms explaining agitation-enhanced nucleation of crystals (Liu & Rasmuson, 2013)

Molecular alignment is one of the most popular hypothesis used to explain enhanced nucleation in polymeric materials, however it is unlikely to have an effect on such small molecules like those involved in nucleation from solution as it is reported that atoms and small molecules only align when subject to very strong shear fields ($> 10^{10} \text{ s}^{-1}$) (R. A. Gray et al., 1995).

Secondary nucleation might also play a role by decreasing the time delay from the moment the first crystal is formed to the moment when the nucleation event is detected. However, secondary nucleation is normally much faster than primary, therefore it is unlikely to play a dominant role (Liu & Rasmuson, 2013).

The *enhanced mass transfer* theory, suggested by Nyvlt et al. (1966), is based on the idea that in an agitated system, solute molecules travel faster towards sub-critical nuclei. The solid-liquid mass transfer in agitated liquid containing fine solid particles can be described using the following empirical model

$$Sh = \frac{k_{SL} d_p}{\mathcal{D}} = 2 + 0.52 Re_T^{0.52} Sc^{1/3} \quad (2.72)$$

where Sh is the Sherwood number, k_{SL} is the solid particle-liquid mass transfer coefficient, d_p is particle diameter, \mathcal{D} is the diffusivity, $Re_T = (\varepsilon d_p^2 / \nu^{1/3})^{1/3}$ is the Reynold's number calculated using the Kolmogoroff's theory of isotropic turbulence and $Sc = (\mu / \rho \mathcal{D})$ is the Schmidt number. However, this model can only be used to explain the movement of particles larger than 1 μm as for smaller particles the effect of turbulence becomes negligible and the equation reduces at

$$Sh = \frac{k_{SL} d_p}{\mathcal{D}} = 2 \quad (2.73)$$

Therefore, this model also seems unsuitable to explain the effect of agitation on crystal nucleation from solution. However, it should be recognised that nucleation and mass transfer are significantly different phenomena and might be hard to find a simple correlation between them. In particular, the correlation presented above for mass transfer is based on volume-averaged parameters that describe the fluid flow (e.g. average velocity); while nucleation is an activated phenomenon which is statistically expected to take place in the point of the reactor that has the most favourable conditions. If one considers the level of energy dissipation generated for example at the tip of a turbine or of a magnetic stir bar, then the local increase in mass transfer might have a significant effect and promote the formation of a stable nucleus (Liu & Rasmuson, 2013).

The *shear-enhanced cluster aggregation* theory is based on the idea that the fluid flow is unlikely to enhance the probability of collision of single solute molecules, however, the velocity gradients may significantly increase the probability of collision of the larger meso-

scale clusters. The existence of a significant number of meso-scale clusters in supersaturated solution is not universally accepted by the scientific community as it contradicts one fundamental assumption of the Classical Nucleation Theory (CNT), namely, that nuclei formation proceeds through a process of addition and subtraction of single solute molecules to a sub-critical size cluster. However, it finds support within the Two-Step Nucleation Theory introduced by Velikov in 2010. Despite it being far from proved, recent papers introduced more experimental evidence to support the existence of meso-scale clusters. As a result, the shear-enhanced cluster aggregation theory remains at present the most widely accepted explanation of the effect of agitation on crystal nucleation (Chattopadhyay et al., 2005; Jawor-Baczynska et al., 2015, 2013; Kumar et al., 2006; Pan et al., 2010).

2.3 Microfluidics

The term *microfluidic* is used to refer to a wide range of flow systems characterised by small channel dimensions (in the order of hundreds of microns). However, the classification of microchannels does not merely depend on the dimension of the channel itself, but on a number of factors that determine the behaviour of the fluid flow inside the channel. In particular, fluid flow in microfluidic systems is characterised by low values of Reynolds and Péclet numbers such that the viscous forces are dominant over the inertial forces and the resulting flow inside the channel is laminar. In addition, the high surface to volume ratio that characterises these systems produces fast heat and mass transfer. The predictable and regular flow pattern, the enhanced mass transfer and the ability to easily control the temperature of the fluid make these devices highly attractive both to industry and academic research. In particular, microfluidic devices have found wide application in the study of the crystallization process of proteins or small molecules in solution. One reason of their success in the crystallization field is the possibility to easily decouple the nucleation and the growth step by applying a specific temperature profile, thereby making it easier to perform accurate nucleation kinetics studies in controlled fluid dynamic conditions (Jiang & Ter Horst, 2011; Laval et al., 2007; Rossi et al., 2015; S. Teychené & Biscans, 2012).

Initially, microfluidic chips were produced by means of silicon microfabrication, however nowadays various techniques have become available so that it is possible to produce microchips from metals, ceramics, silicon, glass and plastic (Gavriilidis et al., 2002). Despite their advantages, the fabrication of microfluidic chips is usually very expensive as it requires costly equipment and trained personnel. In addition, they have a fixed geometry, which cannot be modified once the chip is sealed. Microfluidic layouts obtained from flexible tubings represent a relatively inexpensive alternative to microchips as they maintain all the advantages of microfluidic silicon or PDMS chips while providing the experimenter with some additional flexibility (microfluidic layout and length of the channel can be easily adjusted). In this regard, polymeric capillaries or hollow fibres have been successfully used in crystallization studies of paracetamol and alpha-lactose (Dombrowski et al., 2007; Zarkadas & Sirkar, 2007).

Handling particulate flow inside such small channels represents one of the biggest challenges both for industrial and research applications (continuous fine chemical manufacturing, particle screening, crystallization studies etc.) as solid particles can easily obstruct small channels and cause clogging. This is especially true when the process involves generation of solid particles, as it is the case for cooling crystallization from solution, because the channel walls can act as sites for heterogeneous nucleation, thereby causing crystals to grow until they completely block the channel. However, continuous cooling crystallization in millichannels has been successfully carried out by seeding thereby avoiding primary nucleation which is the main cause of channel blocking (Hohmann et al., 2018). In order to avoid or limit clogging of microchannels when conducting primary nucleation studies, the following aspects should to be taken into account (Hartman, 2012):

- The use of non-sticky materials, such as fluoropolymers, or superhydrophobic and superoleophobic surfaces can reduce the risk of particle deposition;
- High surface roughness and inhomogeneous temperature can drastically increase the chances of clogging due to particle deposition and heterogeneous nucleation on the channel walls, and they should be therefore avoided;
- Bottlenecks, edges, cavities and tight curves in the channel geometry should also be avoided as they are likely to cause obstruction or complete blockage of the channel;

A common solution adopted to prevent clogging is to use a two-phase flow pattern so that the main flow is divided into small plugs or droplets which are kept separated by an immiscible inert phase (called carrier phase or continuous phase). The choice of the carrier phase depends on the nature of the main fluid and the channel material but it is normally chosen to have similar wetting properties as the channel walls (hydrocarbon or fluorocarbon oils are generally used when the main fluid is an aqueous phase) (Anna et al., 2003; Thorsen et al., 2001). When appropriately chosen, the carrier phase will form a thin film separating the droplets of the main fluid from the channel walls. As this film actively prevents the main fluid from being in contact with the channel walls, it reduces the risk of clogging due to particle deposition and crystals growing on the solid surfaces. In addition, it is beneficial in the nucleation kinetics studies as it reduces the chances of heterogeneous nucleation on the channel walls, leading to a more accurate estimation of primary nucleation rate.

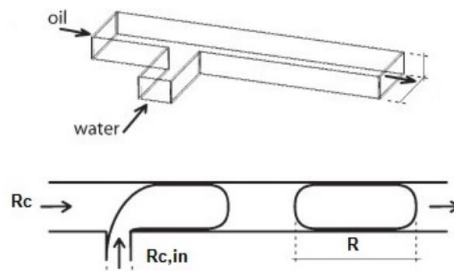


Figure 2.15 Schematic of a microfluidic T-junction and droplet formation inside the channel (adapted from Garstecki et al., 2006)

The segmented flow is normally obtained using a simple T-junction as schematically shown in Figure 2.15. Formation of two-phase flow in microchannels has been extensively studied in the literature; in particular, Garstecki et al. (2006) identified two mechanisms that could describe the formation of droplets and bubbles in a T-junction, these mechanisms are named *squeezing* and *dripping*. The authors found that, if the interfacial forces dominate over the shear stress, i.e. at low Capillary numbers ($Ca = \mu_d U_{mix}/\sigma$, where μ_d is the viscosity of the droplet, U_{mix} is the mixture velocity of the two-phase and σ is the interfacial tension), the breakup mechanism is regulated by the *squeezing regime* (pressure dominated regime). In this case the bubble tip grows until it occupies the whole cross

section of the channel; as consequence the upstream pressure of the continuous phase increases and causes the bubble detachment. On the other hand, if Capillary number is higher than a critical value, the shear stress effect becomes important and the break-up mechanism switches to the *dripping regime* (shear dominated regime), typical of unconfined flow regimes.

Due to the presence of a second phase (carrier phase) that confines the flow of the main fluid, often an internal recirculation is observed inside the plugs. In his pioneering study, Taylor (1960) suggested that for segmented gas-liquid flow, three different flow patterns might be observed inside the liquid plugs depending on Capillary number and m values ($m = (v_b - U_{mix})/v_b$, where v_b is the bubble velocity and U_{mix} is the mixture velocity calculated as the flow rate divided the cross section of the channel). For high capillary number and $m > 0.5$, no recirculation is expected as the flow experiences only one stagnation point at the front of the bubble (Figure 2.16 a), while for $m < 0.5$ two recirculation flow patterns are possible (Figure 2.16 b & c). The intensity of recirculation and the position of the stagnation points depend on various factors, such as the length of the plug, the mixture velocity, the thickness of the film and the channel geometry.

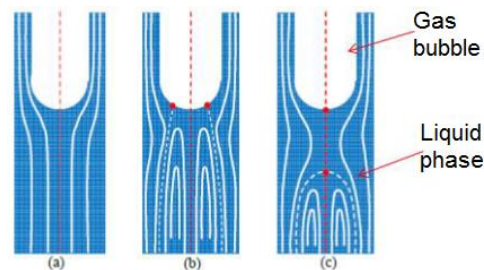


Figure 2.16 Schematic representation of the possible recirculation flow patterns that can be observed in two-phase gas-liquid flow in capillaries; (a) $m > 0.5$, (b)(c) $m < 0.5$, where $m = (v_b - U_{mix})/v_b$ (Adapeted from Taylor, 1960).

Thulasidas et al. (1997) proposed a simple correlation to estimate the position of the stagnation points shown in Figure 2.16:

$$r_0 = \frac{R}{\sqrt{2}} \sqrt{2 - \psi} \quad (2.74)$$

$$r_1 = R\sqrt{2 - \psi} \quad (2.75)$$

where R is the channel radius, $\psi = v_b/U_{mix}$, r_0 is the position of the centre of the vortex, r_1 is the position of the stagnation streamline. For small values of the capillary number it is expected $v_b \approx U_{mix}$, therefore $\psi \approx 1$; while for $\psi = 2$, results $r_0 = r_1 = 0$, that corresponds to the condition of total bypass depicted in Figure 2.16.

More recently, studies have been performed to experimentally resolve the recirculation flow pattern in liquid-liquid slug flow using Particle Image Velocimetry (PIV), which consists in adding μ -particles to one or both the liquid phases and tracking them using a high speed camera system. Once the flow field has been experimentally obtained, one has to subtract the velocity at which the plug is moving in order to reveal the structure of the internal recirculation (Figure 2.17).

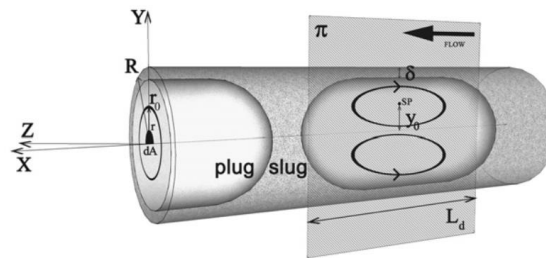


Figure 2.17 Schematic of liquid-liquid slug flow in a microchannel (Dore et al., 2012).

Dore et al. (2012) performed a series of experiments using PIV to visualise the flow structure inside water droplets in a circular microchannel and they found that the main flow direction is along the horizontal axis with the maximum velocity at the centre of the channel. In addition, they showed that a fully developed parabolic Poiseuille profile is established at the centre of the droplet (along the horizontal axis) with the maximum velocity being twice the mixture velocity, while the maximum velocity gradually decreases as we approach the liquid-liquid interface (at the front of the back of the droplet) (Figure 2.18). Encouragingly, their results agree with the current published literature (Kurup & Basu, 2012).

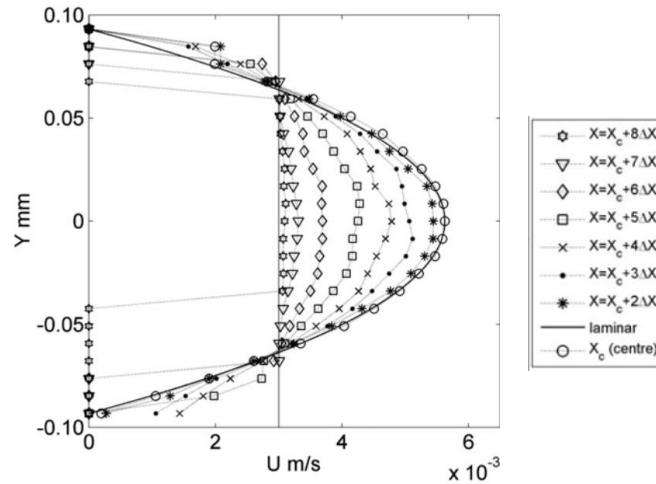


Figure 2.18 Samples of the horizontal component of velocities inside the plug; Y is the vertical direction (parallel to the channel radius) and X is the horizontal direction (parallel to the flow direction); x_c is the axial location of the plug centre; $\Delta x \approx 24$ mm. (Dore et al., 2012).

The importance of the above described recirculation flow pattern in crystal nucleation will be explored in Chapter 5 where droplets containing the crystallising solution under study were generated in a millichannel with the aid of an immiscible carrier phase. The study will try to find a link between fluid shear and nucleation rate.

Chapter 3

MICROMIXING EFFICIENCY AND LOCAL ENERGY DISSIPATION IN STIRRED TANK AND BUBBLE COLUMN REACTORS

3.1 Introduction

Stirred reactors and bubble column reactors are normally used in many industrial applications as mixers, crystallizers, bioreactors etc. Fluid dynamics inside these reactors is usually quite complex and difficult to characterise especially because they usually operate in fully turbulent conditions in order to ensure uniformity of temperature and concentration. Chemical methods, like Villermaux-Dushman method, represent a quick and cheap method to assess local mixing at molecular scale. This technique has been successfully used in the past to investigate the mixing characteristics of single phase stirred tanks (Assirelli et al., 2002; Fournier et al., 1996) and micromixers (Falk & Commenge, 2010), however fewer studies have been conducted on aerated tanks due to the higher complexity and inhomogeneity of the system (Cui et al., 1996). As a result, the role of gas sparging in the micromixing process is still unclear (Li et al., 2014). One of the reasons is that often gas spargers are coupled with stirring turbines with the aim of producing a more uniform fluid dynamic environment, so the effect of the two cannot be distinguished and the contribution of the gas to the local micromixing results unclear. As discussed in section 2.2.1, the micromixing process can be modelled using various approaches and the characteristic micromixing time associated with the local fluid dynamic conditions can be calculated. Assessing mixing characteristic at a molecular level is very important as it has a profound influence over processes based on molecular-molecular interaction such as chemical reactions, crystal nucleation and growth (Bałdyga, 2016) or processes that rely on quick and efficient dispersion of the feed plume (e.g. anti-solvent crystallization). Also, microorganisms and cells growing in bioreactors may be damaged depending of the local fluid dynamic conditions and associated shear stress (Chisti, 2001).

In this chapter, I apply a well-established technique to measure the micro-mixing time in a cylindrical unbaffled vessel. Unbaffled vessels are often used in food or pharmaceutical industry for preliminary laboratory-scale investigations or, at larger scale, where cleaning in-place is needed (Assirelli et al., 2008). The liquid is either agitated by means of a Rushton turbine or by bubbles produced with a gas sparger and the results obtained in the two experimental systems are compared in terms of micromixing time and energy dissipation rate. The results obtained here will be also used in Chapter 4 to investigate the effect of

micromixing and energy dissipation on primary nucleation of para-amino benzoic acid in water.

3.2 Experimental setup and procedure

3.2.1 Reaction system

The Villiermaux-Dushman reaction system is commonly used in the literature for micromixing characterisation and consists of two parallel competitive reactions.



Because reaction (i) can be regarded as instantaneous with respect to reaction (ii), the amount of I_2 formed will depend on the mixing condition. The better the mixing, the less I_2 is formed. Reaction (ii) is found to be a 5th order reaction and its kinetics has been experimentally determined by Guichardon & Falk (2000)

$$r_{ii} = k[H^+]^2[I^-]^2[IO_3^-] \quad (3.3)$$

where the kinetic constant, k , depends on the ionic strength, μ (Guichardon & Falk, 2000)

$$\mu < 0.166 M \quad \log_{10}(k) = 9.28105 - 3.664\sqrt{\mu} \quad (3.4)$$

$$\mu > 0.166 M \quad \log_{10}(k) = 8.383 - 1.5112\sqrt{\mu} + 0.23689 \mu \quad (3.5)$$

It should be noted that the formation of iodine through reaction (ii) will induce production of triiodide through the equilibrium reaction



where the equilibrium constant is calculated according to Guichardon & Falk (2000)

$$\log_{10} K_B = \frac{555}{T} + 7.355 - 2.575 \log_{10} T \quad (3.7)$$

where T is the absolute temperature (K) and K_B is in l/mol

3.2.2 Segregation index

The micromixing efficiency is usually quantified through the *segregation index*, X_s , which represents the yield of iodine with respect to the total amount of acid used, which, for the experimental procedure used here, is the limiting reagent. The segregation index is therefore defined as

$$X_s = \frac{Y}{Y_s} \quad (3.8)$$

where Y is the yield of I_2 with respect to H^+

$$Y = \frac{2(n_{I_2} + n_{I_3^-})}{n_{H^+}^0} = \frac{2 V_R ([I_2] + [I_3^-])}{V_{H^+} [H^+]_0} \quad (3.9)$$

where the subscript 0 indicates the initial condition values, V_R is the reaction volume and V_{H^+} is the volume of acid injected. Note that I_2 and I^- in solution form an equilibrium with I_3^- according to equation (3.6), therefore, experimentally the total amount of I_2 produced through reaction (ii) has to be calculated as the sum of the number of moles of I_2 and I_3^- present in solution.

Y_s represents the value of Y in case of total segregation, that corresponds to the condition when the micromixing time is much longer than reaction time of reaction (ii).

$$Y_s = \frac{6 n_{IO_3^-}^0}{6 n_{IO_3^-}^0 + n_{H_2BO_3^-}^0} = \frac{6 [IO_3^-]_0}{6 [IO_3^-]_0 + [H_2BO_3^-]_0} \quad (3.10)$$

Equation (3.10) is obtained considering that the product distribution depends only on the stoichiometry of the reaction. As a consequence of the above considerations relative to Y and Y_s , it follows that the segregation index represents the non-dimensional yield of I_2 with respect to H^+ and it can vary between 0 and 1; in particular

$$X_s = X_s^{PM} = 0 \quad \text{for perfect micromixing} \quad (3.11)$$

$$X_s = X_s^{TS} = 1 \quad \text{for total segregation} \quad (3.12)$$

In order to estimate the amount of iodine formed, and therefore calculate Y , we should experimentally determine I_3^- concentration by measuring the absorbance of the final solution (details of the procedure for measuring triiodide concentration are presented in Appendix A). Once the amount of I_3^- present in solution has been determined, we can calculate back the amount of iodine originally formed through reaction (ii) through the following mass balance

$$[I^-] = [I^-]_0 - \frac{5}{3}([I_2] + [I_3^-]) - [I_3^-] \quad (3.13)$$

where $[I^-]$ can be calculated from the equilibrium relation

$$K_B = \frac{[I_3^-]}{[I_2][I^-]} \quad (3.14)$$

By substituting equation (3.14) into equation (3.13) we obtain a quadratic equation that allows us to determine the final concentration of iodine, $[I_2]$.

$$-\frac{5}{3}[I_2]^2 + \left([I^-]_0 - \frac{8}{3}[I_3^-]\right)[I_2] - \frac{[I_3^-]}{K_B} = 0 \quad (3.15)$$

where the equilibrium constant, K_B , is given by equation (3.7). From equation (3.15) we can easily calculate iodine concentration, $[I_2]$, and substitute it into equation (3.9) to calculate the segregation index, X_s , from equation (3.8). To quantify the efficiency of

mixing, Villermaux (1986) also suggests an alternative parameter to the segregation index: the *micromixedness ratio* or *micromixing efficiency* α which is derived from X_S by ideally dividing the reactor volume into two areas: one perfectly mixed and the other totally segregated. Using these assumptions, one can write

$$(V_{PM} + V_{TS}) X_S = V_{PM} \cdot X_S^{PM} + V_{TS} \cdot X_S^{TS} \quad (3.16)$$

where V_{PM} and V_{TS} are the volumes characterised by perfect micromixing and total segregation respectively, X_S^{PM} is the segregation index in perfect micromixing conditions and X_S^{TS} is the segregation index in total segregation conditions. Substituting equations (3.11) and (3.12) into equation (3.16) we can define the micromixedness ratio α as

$$\alpha = \frac{V_{PM}}{V_{TS}} = \frac{1 - X_S}{X_S} \quad (3.17)$$

The micromixedness ratio α can be used as an alternative to the segregation index and represents the efficiency of micromixing: the better the micromixing the higher the micromixedness ratio parameter.

3.2.3 Experimental procedure

The experimental procedure consists of adding a small quantity of diluted sulphuric acid in stoichiometric deficiency to the aqueous solution. The injection is done through a 1 mm inner diameter glass pipe. The sulfuric acid quantity has to be in sub-stoichiometric with respect to the other reactants so that, in perfect micromixing conditions, the acid plume is instantaneously dispersed and all the protons are neutralised by the borate ions according to reaction (i); while, in perfect segregation conditions, the time needed to disperse the acid plume is larger than the reaction time of reaction (ii,) so after reacting with nearby borate ions, the acid molecules start to react with iodide and iodate ions producing iodine through reaction (ii). By measuring the selectivity to iodine Y as shown in the previous section, we can then quantify the level of local micromixing. A simplified representation of

the reaction scheme in the two micromixing conditions described above is presented in Figure 3.1.

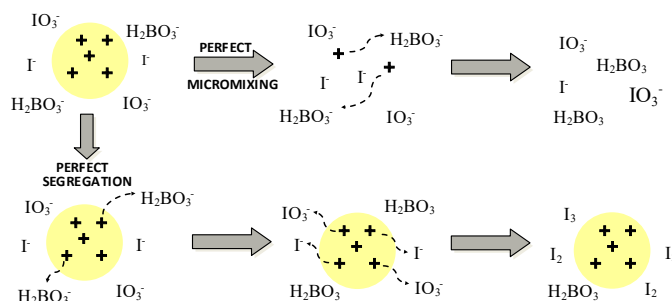


Figure 3.1 Simplified representation of the reaction scheme in perfect micromixing conditions and perfect segregation conditions.

The sequence of mixing and the concentrations of the reactants used here have been chosen according to the recommendation of Guichardon & Falk (2000) (Table 3.1 and Table 3.2) and all the reactants have been used without further purification. The sulfuric acid solution was obtained by diluting a commercial concentrated solution (6 N) of sulfuric acid with DI water (conductivity < 0.2 $\mu\text{S}/\text{cm}$). The borate-iodate-iodide solution was prepared by mixing four separate aqueous solutions: borate aqueous solution was prepared by dissolving a known amount of H_3BO_3 powder ($\geq 99.5\%$ pure, Sigma-Aldrich) in DI water; the NaOH aqueous solution (2 M) was purchased from Sigma-Aldrich and used without further purification; KI and KIO_3 aqueous solutions were prepared by separately dissolving each powder ($\geq 99.5\%$ pure, Sigma-Aldrich) in DI water before each experiment. H_3BO_3 and NaOH solutions were mixed first in the reactor, then KIO_3 and KI solutions were added and the final solution was stirred for 1 min to ensure that all the reactants were uniformly mixed. pH of the final solution was then checked using a standard pH-meter in order to ensure that was in the range 8.5 – 9.5 as recommended by Guichardon & Falk (2000) to avoid iodine dismutation. After that, either the turbine or the gas flow (depending on if we wanted to measure the micromixing for the stirred tank or the bubble column) was activated and we started the acid injection using a syringe pump (Harvard PHD 2000, programmable). The location of the acid injection will be discussed in the following section. 1 ml of liquid was collected from the reactor with a plastic pipette 1 min after the end of

the acid injection in order to ensure uniformity of the solution. The absorbance spectrum was measured immediately by means of a spectrophotometer and the triiodide concentration was derived from the value of the absorbance at 353 nm as suggested in the literature (Guichardon et al., 2000). The set of initial concentrations used has been chosen carefully so that it yields an optical density within the validity range of Beer-Lambert law for triiodide. The experimental procedure used to determine extinction coefficient to calculate the triiodide concentration and typical spectra obtained are presented in Appendix A.

Table 3.1 Initial reactant concentrations in the buffer solution (total volume of the solution: 1.5 L)

	KI	KIO₃	H₃BO₃	NaOH
Concentration [M]	0.0233	0.0047	0.1818	0.0909

Table 3.2 Experimental parameters relative to the sulfuric acid injection (concentration is calculated based on the volume of acid injected).

Volume	1 ml
Concentration	1 M
Pipe diameter	1 mm
Injection time	120 s

3.2.4 Experimental setup

The experimental setup used for this work consists of a cylindrical unbaffled transparent vessel of 2.3 L volume that contained the borate-iodate-iodide solution described above. To provide agitation, two devices could be used: a stainless-steel turbine and a ring-shaped gas sparger. The stirrer, depicted in Figure 3.2, is a traditional Rushton turbine with 6 vertical blades placed at the centre of the reactor; turbine dimensions are reported in Table 3.3. The sparger, depicted in Figure 3.2, is a stainless steel ring which exhibits 17 holes of 250 μm nominal diameter and is placed at the bottom of the reactor; dimensions of the sparger are also reported in Table 3.3. In order to avoid oxidation of the reactants, we used nitrogen as sparging gas.

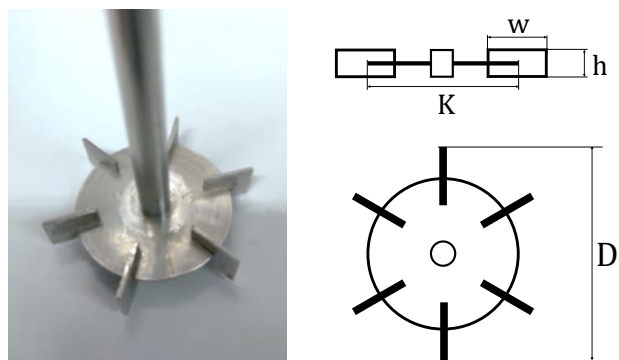


Figure 3.2 Rushton turbine used in this work (dimensions are listed in Table 3.3)

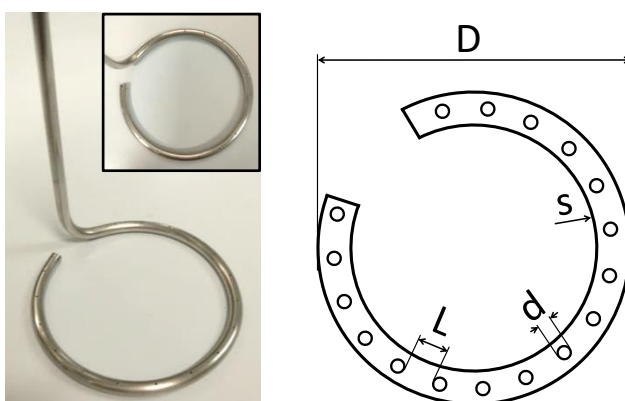


Figure 3.3 Gas sparger used in this work (dimension listed in Table 3.3)

The complete reactor configurations are schematically shown in Figure 3.5 for the *stirring* experiments and the *bubble column* experiments, respectively; a picture of the complete experimental setup is reported later in the thesis (Figure 4.3), however it should be noted that the conductivity probe shown in Figure 4.3 was not present for the experiments presented here. The lid of the reactor has been purposely designed to hold the glass pipette (glass pipettes used is shown in Figure 3.4) used to inject the sulfuric acid (the acid injection procedure is described in Appendix B). As it can be noted from Figure 3.4 (left), the glass pipe used for the experiments with the gas sparger has been bent in a way that the acid comes out from the pipe in a direction which is perpendicular to the gas flow. This has been done in order to avoid backmixing inside the pipe which could result in a segregation index higher than the real one. For the same reason, the glass pipe used for the experiments with the Rushton turbine has been left unbent Figure 3.4 (right) so that the acid comes out of

the pipe in a direction perpendicular to the main fluid flow direction. This ensures that no backmixing is taking place and that the Villermaux-Dushman reactions start only when the acid is in the bulk of the fluid.



Figure 3.4 Glass pipette used for the acid injection for the experiments with the gas sparger (left) and Rushton turbine (right).

Two different injection positions have been used for the experiments in order to estimate the micromixing efficiency in different points of the reactor using the experimental technique described in sections 3.2.1 and 3.2.2. The exact coordinates of the injecting positions are denoted as <1> and <2> and are showed in Figure 3.5.

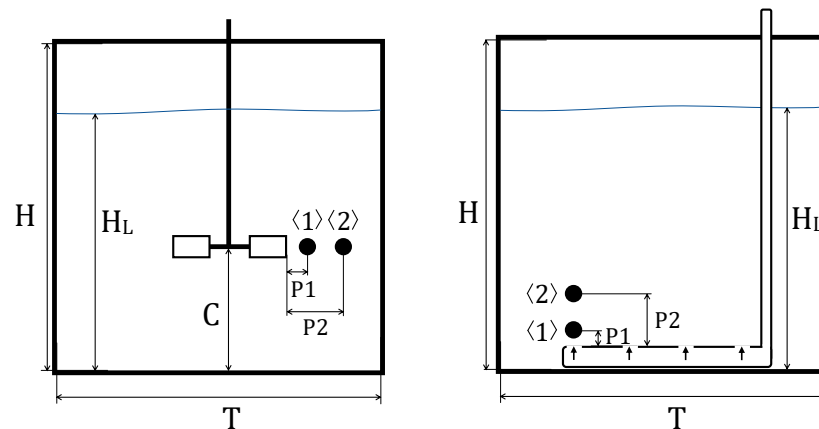


Figure 3.5 Schematic of reactor configuration for the *stirring* experiments with the Rushton turbine (left) and the *bubble column* experiments with the gas sparger (right).

Table 3.3 Dimensions of the equipment shown in Figure 3.2 and Figure 3.5 (all dimensions in millimetres)

Tank	T	C	H	H_L
	120.3	30	200	132
Injection position – <i>stirring</i> experiments	P1	P2		
	3	33		
Injection position – <i>bubbling</i> experiments	P1	P2		
	3	33		
Rushton turbine	w	K	h	D
	10.2	31.4	8.3	41.9
Gas sparger	D	s	d	L
	76	4	0.25	12.5

3.3 Results and discussion

3.3.1 Results from micromixing model

The IEM model for micromixing presented in section 2.2.3 has been applied to the concentration set used in this work in order to find the relation between the segregation index obtained from the experiments and the micromixing time associated with it. The set of equations presented (equations (2.59)-(2.61)) had to be solved for each chemical species involved in the mixing process by first assuming a micromixing time and solving the system of equations taking into account also the reactions rates until all the acid is converted; in this way we obtain the final concentrations of all species which we used to calculate the segregation index, X_s (equation (3.8)) associated with the particular micromixing time chosen. The procedure was then repeated for a number of micromixing times and the graph shown in Figure 3.6 is obtained. This graph is specific for the concentration set used in this work and was used to estimate the micromixing time from the segregation index obtained experimentally. Reactions' kinetics have been obtained from Guichardon et al. (2000).

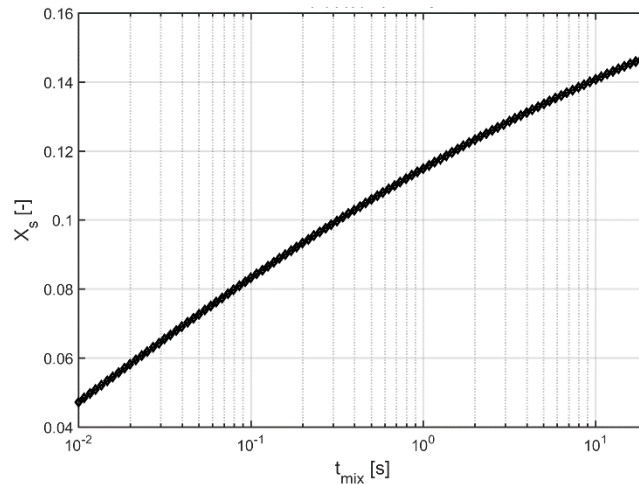


Figure 3.6 Segregation index versus micro-mixing time calculated according to the IEM model for the concentration set used in this work (see Table 3.1 and Table 3.2).

3.3.2 Injection time and mesomixing considerations

In order to correctly estimate the micromixing, it was important to exclude the effect of mixing at other length scales on the micromixing process. Indeed, if the acid is injected faster than the characteristic dispersion time of the plume, the reaction takes place at coarser scales and the measured segregation index results higher than expected (Baldyga & Pohorecki, 1995; Monnier et al., 1999b). In order to avoid this effect and ensure that the experimental results are independent from the macro and meso-mixing, the injection time has to be larger than a critical value. This value has to be determined experimentally. Figure 3.7 shows the measured segregation index at different acid injection times for the reactant concentrations reported in Table 3.1. These graphs were obtained using the worst micromixing conditions (lower stirring rate or gas flow rate). In both cases, the critical injection time was clearly identifiable at 18 s, therefore, to eliminate the dependence of the segregation index on the feed rate, we chose an injection time much larger than the critical value: 120 s, that corresponds to a feed rate of 0.5 ml/min. This value was used for all the experiments presented in this chapter.

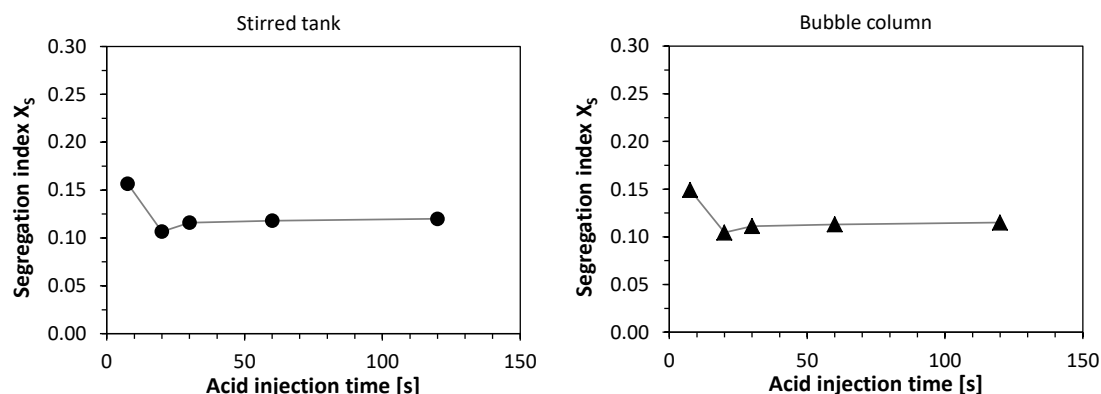


Figure 3.7 Effect of acid injection time on segregation index obtained for the stirred tank (120 rpm) (left) injection point <2>, and the bubble column (1 l/min) (right), injection point <2>.

3.3.3 Loss of iodine due to stripping

Since iodine is a substance with high volatility, we had to account for a possible decrease of its concentration due to stripping. For this reason, in order to validate the experimental procedure described above and to ensure that no significant loss of the reaction products was taking place, we measured the absorbance of the final solution at various times after the end of acid injection. The first measurement is taken after about 2 minutes from the end of the acid injection as recommended by Guichardon et al. (2000) to ensure the homogenization of the solution. Results of the measurements are presented in Figure 3.8 for various gas flow rates in terms of segregation index X_s . The graph shows a slight decrease of the segregation index over time which suggests that iodine is slowly evaporating from the liquid solution due to the gas flow; as a consequence, the equilibrium results shifted towards the right-hand side of equation (3.6) and some triiodide had to transform into iodine to restore the equilibrium.

The rate of decrease of the segregation index was approximately the same for the three flow rates shown, therefore we assumed that the rate of evaporation of iodine was the same regardless of the gas flow rate. Because of the relatively high gas flow rate used in this work, the rate of evaporation of iodine causes a non-negligible decrease of the segregation index if long time intervals are considered (> 30 mins). However, the time lapse from the moment in which the formation of iodine (I_2) was possible (injection of the acid plume) to the moment in which the measurement was taken was no longer than 4 minutes.

According to our measurements, for such a short time lapse, the decrease in the segregation index is expected to be less than 1%, which can be considered within the experimental error. This result is in agreement with what observed by Cheng et al. (2012) and Hofinger et al. (2011) who found that the deviation in the segregation index is negligible compared to the ungasged case. Therefore, we assumed that iodine stripping did not have a significant effect over the experimental results and no correction was made in this regard.

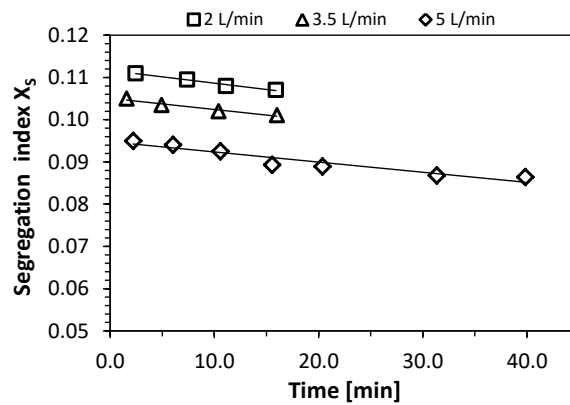


Figure 3.8 Decrease of segregation index X_s (calculated from absorbance measurements) due to iodine stripping over time (injection position <2>); measurements are taken at various times after the end of the acid injection while the solution was sparged continuously.

3.3.4 Stirred tank: effect of agitator speed and feed position

The results of the experiments described above are reported in Figure 3.9 in terms of micromixedness ratio α , defined in equation (3.17), for the stirred tank. It can be noticed that the micromixing efficiency increases linearly with agitation speed at both measurement locations while it is consistently higher at position <1>. This result is in agreement with data present in the literature that show that the region next to the impeller's blades exhibits the highest micromixing performance (Assirelli et al., 2002).

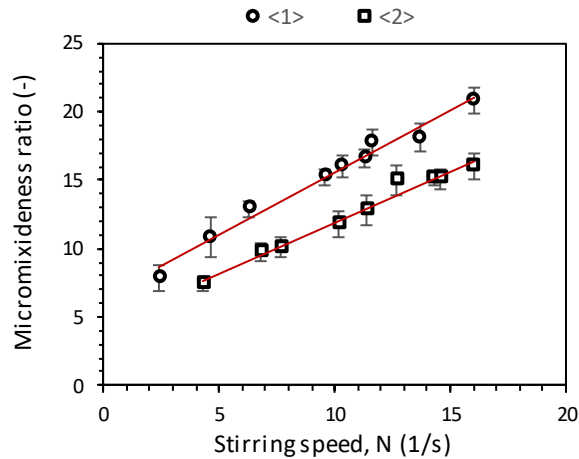


Figure 3.9 Micromixedness ratio α versus stirrer speed N obtained for measuring position <1> (R^2 of linear fitting 0.98) and <2> (R^2 of linear fitting 0.98).

The micromixing time was calculated from the micromixedness ratio α according to the IEM model presented above, and the results are reported in Figure 3.10. In order to compare our results with the literature data, micromixing time was plotted both against the stirring speed (Figure 3.10, left) and the average energy dissipation rate (Figure 3.10, right) calculated according to equation (2.64). It can be observed that micromixing time varies by approximately two orders of magnitude within the present experimental conditions: from 10^{-0} s for the lowest stirring speed, to 10^{-2} s at the maximum impeller velocity. These are typical values obtained using laboratory-scale stirred tanks (Fournier et al., 1996; Monnier et al., 1999b). Since micromixing performance strongly depends on the measurement location and system geometry, limited comparison can be made with existing literature data, however, the values of mixing time obtained for specific impeller velocities are in the same order of magnitude as those obtained by Assirelli et al. (2008) who measured micromixing time in unbaffled vessels at various distances from the impeller. In particular, between the various injection positions investigated in their work, we identified two of them as being analogous to those used in this work. Comparing the micromixing time for these two cases reveals a very good agreement in terms of orders of magnitude with those obtained in this work at similar stirring rates. It can be also noted that the micromixing time dependence on the average energy dissipation rate can be described by a straight line on a

log-log plot (Figure 3.10, right) that corresponds to a power-law evolution. In particular, for the experimental data obtained in this work we can write

$$t_{\mu} \propto \bar{\varepsilon}_T^{-0.95} \quad \text{position } \langle 1 \rangle \quad (3.18)$$

$$t_{\mu} \propto \bar{\varepsilon}_T^{-1.22} \quad \text{position } \langle 2 \rangle \quad (3.19)$$

where t_{μ} is the micromixing time and $\bar{\varepsilon}_T$ is the average energy dissipation rate (W/kg) associated with the stirred tank and calculated from equation (2.64). The same kind of dependence was found by Fournier et al. (1996) and Monnier et al. (1999b) who used the Villiermaux-Dushman reaction scheme to measure micromixing performance in stirred tanks and estimate micromixing time from the segregation index using the incorporation model (briefly described in section 2.2.3). My results also show that micromixing time can be effectively reduced by adjusting the injection position, therefore potentially improving processes such as antisolvent crystallization or reactive mixing.

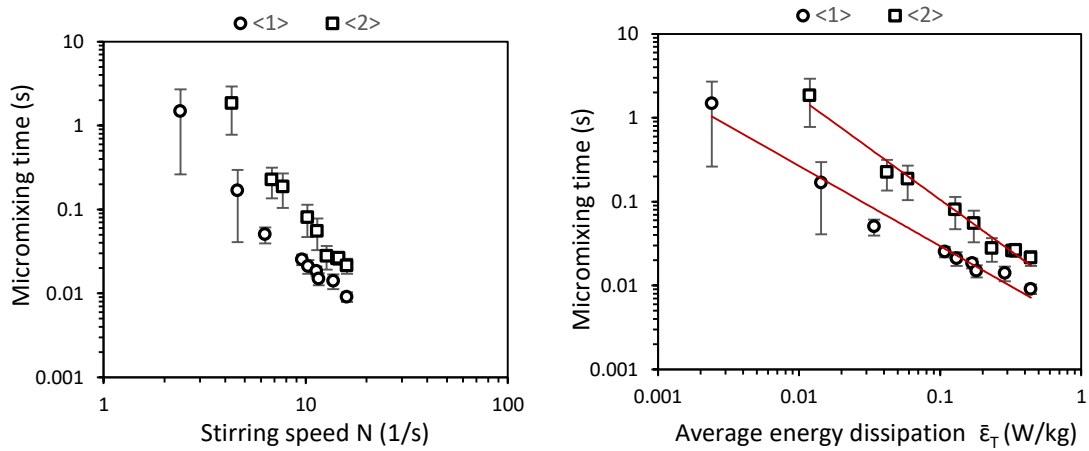


Figure 3.10 Micromixing time as function of the stirrer speed (left) and the average energy dissipation (right) for position $\langle 1 \rangle$ (R^2 of fitting 0.98) and $\langle 2 \rangle$ (R^2 of fitting 0.98); the corresponding standard deviations are reported as error bars.

The local energy dissipation rate for the stirred tank ε_T was calculated from the micromixing time according to equation (2.51). Figure 3.11 shows ε_T as function of stirring speed N : as expected, it is consistently higher for position $\langle 1 \rangle$ with respect to position $\langle 2 \rangle$, and the magnitude of the difference between the two feeding positions increases with the stirring

speed. This suggests that the energy is dissipated at quite different rates throughout the tank and this inhomogeneity increases with the stirring rate.

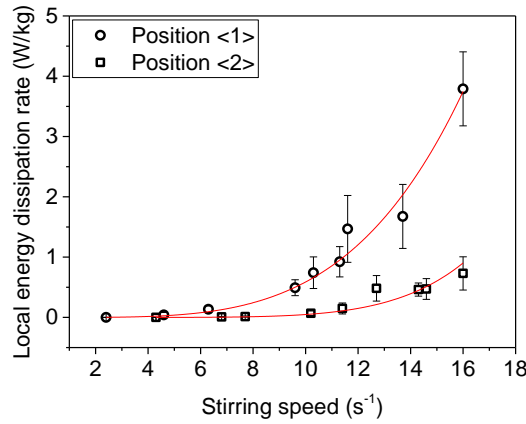


Figure 3.11 Local energy dissipation versus stirring speed at position <1> and <2>.

The data of the local energy dissipation rate versus the stirring rate were fitted using a power law equation such that

$$\varepsilon_T = a N^b \quad (3.20)$$

where a and b are fitting parameters whose values are reported in Table 3.4 both for position <1> and <2>. The empirical equation obtained above will be used in Chapter 4 to calculate ε_T for each crystallization experiment performed; this will allow to investigate the relation between local fluid dynamic conditions and crystal nucleation.

Table 3.4 Experimental fitting parameters of equations (3.20) for the stirred tank

	Position <1>	Position <2>
a	$6.7 \times 10^{-5} \pm 2.8 \times 10^{-5}$	$2.7 \times 10^{-8} \pm 2.0 \times 10^{-8}$
b	3.9 ± 0.17	6.2 ± 0.28

We calculated the dimensionless local energy dissipation rate φ_T defined in equation (2.65), as the ratio between the experimental local energy dissipation rate (Figure 3.11), and the specific energy input, $\bar{\varepsilon}_T$ (equation (2.64)). Figure 3.12 reports the values of φ_T obtained

in this work for feeding position <1> and <2>. The dimensionless local energy dissipation parameter helps to assess the distribution of energy dissipation throughout the vessel with respect to the specific power input and provides information about the energy dissipation homogeneity inside the vessel. As expected, φ_T is found to be larger than 1 close to the impeller's blades (position <1>), ranging from 10^0 to 10^1 , while it ranges from about 10^{-1} to 10^0 at position <2>; the φ_T values relative to position <1> and <2> differ by about one order of magnitude for the whole range of stirring speed analysed. However, as reported by Assirelli et al. (2002), the exact value of φ_T varies a lot in the literature even for similar systems due to its high sensitivity to the measurement position.

In general, the energy dissipation is expected to be higher than the average value in the areas near the impeller, while it should fall below the average value in areas far from the impeller (Assirelli et al., 2002). The distance from the impeller at which the energy dissipation approaches the average value is dependent on the stirring speed, fluid type, impeller and tank geometry. Also, the difference between the values found at position <1> and <2> suggests that micromixing efficiency is very high in the vicinity of the impeller where most of the energy is dissipated, while it drops at a small distance from it. Therefore, we can conclude that micromixing is efficient only in the areas close to the impeller, while other regions of the reactor experience a much lower energy dissipation rate.

Our results show an increase of φ_T when the specific energy input, $\bar{\varepsilon}_T$, is increased both for position <1> and <2>; this result is in agreement with Baldyga & Bourne (1983) who report that, when the feed position is located very close to the impeller's blade, an increase of φ is expected when the stirring speed is increased. However, some authors (Assirelli et al., 2002; Li et al., 2014) observed exactly the opposite trend. The reason for this discrepancy is not completely clear and the authors attributed it to the fact that at high impeller speeds the reactants might be pushed towards areas characterised by worse micromixing conditions. In contrast, our experimental results report an increased inhomogeneity in the energy dissipation rate when the stirring rate is increased, in accordance with the theory by Baldyga & Bourne (1983), while gentler stirring conditions result in more homogeneous energy dissipation.

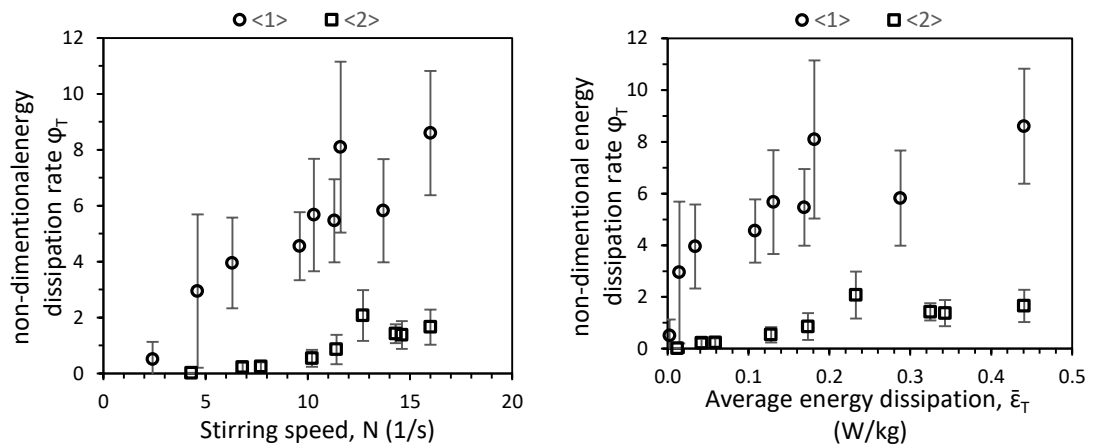


Figure 3.12 Non-dimensional energy dissipation rate, $\phi_T = \epsilon_T / \bar{\epsilon}_T$ at position <1> and <2> as function of the stirring speed N (left) and average energy dissipation $\bar{\epsilon}_T$ (right).

3.3.5 Bubble column: effect of gas flow rate and feed position

Figure 3.13 depicts the micromixedness ratio α as function of the gas flow rate at both investigated positions. It can be noted that α increases linearly with gas flow rate showing that a higher gas flow is effective in increasing the local micromixing performances. Also, α is found to be significantly higher when feeding at position <1>; this suggests that micromixing efficiency improves the closer we move towards the bubble generation point. This is interesting as it suggests that the process of bubble formation, growth and detachment from the gas ring is probably responsible for the observed enhanced micromixing.

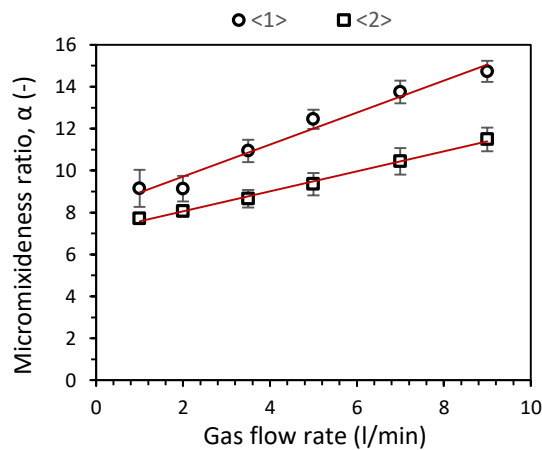


Figure 3.13 Micromixedness ratio α versus gas flow rate calculated for position <1> and <2>.

Figure 3.14 (left) shows the micromixing time calculated from the micromixedness ratio (Figure 3.6) using the IEM method described in section 2.2.3.3 as function of the gas flow rate. Micromixing time measured for the bubble column falls in the same range obtained in case of the stirred vessel ($10^{-1} - 10^0$ s) and decreases with the gas flow rate increase. For the gas flow rate range analysed, the micromixing time drops by about one order of magnitude, showing a significant effect of the gas flow rate on micromixing even at low specific power inputs (Figure 3.14 right).

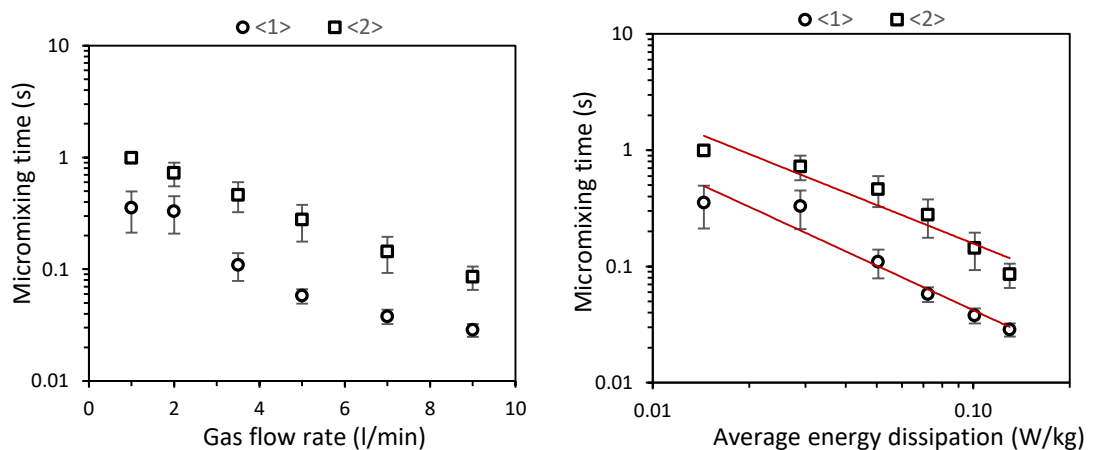


Figure 3.14 Micromixing time versus gas flow (left) and average energy dissipation $\bar{\varepsilon}_G$ (right) rate calculated for position <1> and <2>.

The plot of the local energy dissipation rate as function of the gas flow rate (Figure 3.15) shows a power law evolution similar to that observed for the stirred vessel. Therefore, data can be fitted in a similar way using the following empirical equation

$$\varepsilon_G = a Q_G^b \quad (3.21)$$

where a and b are the fitting parameters whose values are reported in Table 3.5; equation (3.21) can be used to calculate the local energy dissipation rate associated with the gas flow rate used for the experiments. This equation will allow to explore the relation between local fluid dynamic conditions and crystal nucleation in Chapter 4.

Table 3.5 Experimental fitting parameters of equation (3.21) for the bubble column.

	Position <1>	Position <2>
a	$10.0 \times 10^{-4} \pm 3.1 \times 10^{-4}$	$2.8 \times 10^{-4} \pm 6.4 \times 10^{-5}$
b	2.7 ± 0.15	1.8 ± 0.32

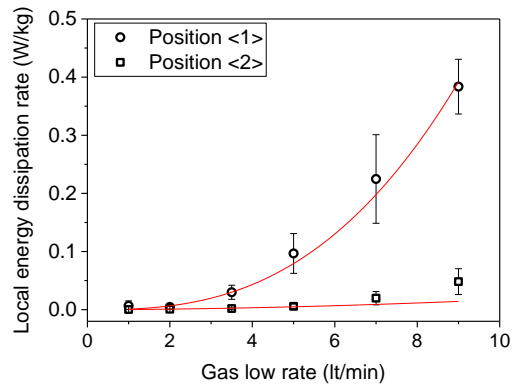


Figure 3.15 Local energy dissipation rate versus gas flow rate for position <1> and position <2>.

The data presented above for the local energy dissipation rate were used to calculate the non-dimensional energy dissipation rate φ_G defined in equation (2.67) as the ratio between ε_G and $\bar{\varepsilon}_G$, where $\bar{\varepsilon}_G$ depends on the gas flow rate as shown in equation (2.66). Results of φ_G are reported in Figure 3.16. Similar to what was observed for the stirred tank, φ_G tends to increase as the average input energy $\bar{\varepsilon}_G$ is increased for both positions. The increase in φ_G confirms that the inhomogeneity in the local energy dissipation rate increases at higher gas flow rates similar to what was observed for the stirred tank. Although a quantitative discussion around this parameter is difficult due to fluctuations in its value, we register relatively high values of φ_G when the feed is located very close to the bubble generation point (position <1>), while farther from it (position <2>), φ_G is one order of magnitude lower. This data suggests that most of the energy is dissipated near the bubble generation point where the energy dissipation rate is relatively high compared to the average value within the vessel; however, such anisotropy is less marked than that observed for the stirred tank as the absolute values of φ_G are lower in the case of the

bubble column. Therefore, we can conclude that the energy dissipation rate calculated is closer to the average value in the bubble column suggesting a more homogeneous energy dissipation rate throughout the vessel with respect to the stirred tank.

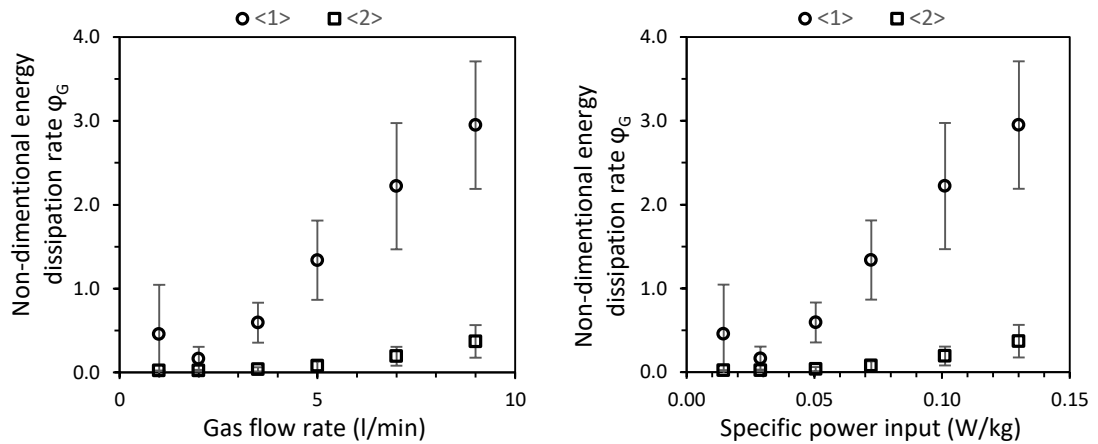


Figure 3.16 Non-dimensional energy dissipation rate, $\varphi_G = \varepsilon_G / \bar{\varepsilon}_G$ at position <1> and <2> as function of gas flow rate (left) and average energy dissipation (right)

3.3.6 Comparison between the stirred tank and the bubble column

In order to compare the micromixing performance of the two systems analysed in this work, namely stirred tank and bubble column, micromixing time data for both setups were plotted together in Figure 3.17 as function of the specific power input. This kind of representation allows a direct comparison of the performance of the two systems. Because in the case of the stirred tank, we performed experiments over a wider range of specific power input $\bar{\varepsilon}$ than for the bubble column, we restrict the following analysis to the $\bar{\varepsilon}$ values common to both systems. A careful observation of Figure 3.17 (left) shows that micromixing times measured at position <1> are at about the same range for the two experimental setups. Such observation suggests that if we consider the average energy dissipation rate $\bar{\varepsilon}$, a very similar micromixing time can be obtained for a given value of $\bar{\varepsilon}$ regardless of whether the agitation is provided by means of a stirrer or a bubble column. As a consequence, the value of the maximum micromixing efficiency in the reactor appears to be governed by the average energy dissipation rate, although slightly lower values are registered for the stirred tank.

Interestingly, in this work, the micromixing times obtained when the feeding position is located very close to the turbines' blades or the bubble generation point are comparable to what other authors (Rousseaux et al., 1999, 2000) achieved using devices especially designed to enhance micromixing. The micromixing times obtained using these special micromixers are indeed in the same order of magnitude ($10^{-2} - 10^{-1}$ seconds) to those obtained here, using a traditional stirred tank or a bubble column. Remarkably, this could be achieved by simply injecting the acid plume in the point of highest turbulence even at a relatively low mean specific energy input compared to average industrial conditions (Liu & Rasmuson, 2013). For completeness, a graph depicting the local energy dissipation rate for both our experimental systems is reported in Figure 3.18. Again, it can be noted that local ϵ for the stirred tank and bubble column is in the same range for position <1> and <2>, while it seems that the maximum measured values of the local energy dissipation rate are slightly larger in the stirred tank.

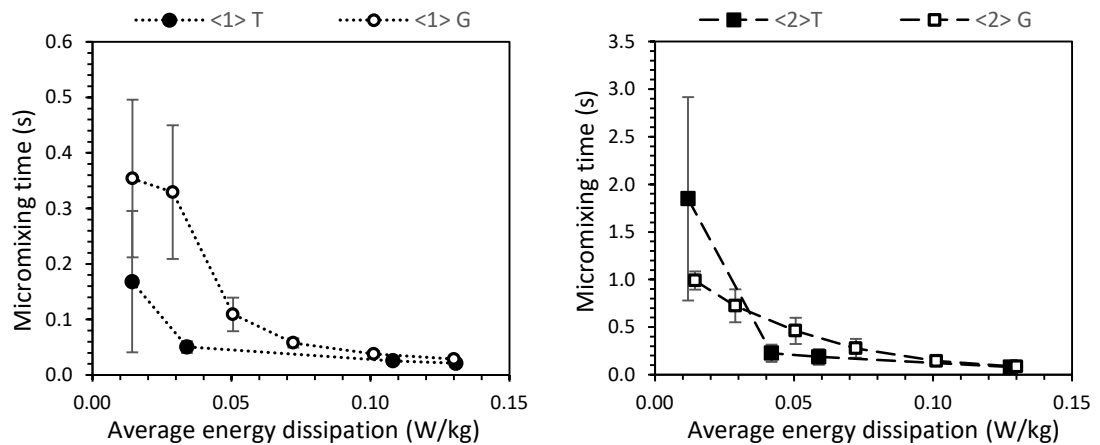


Figure 3.17 Micromixing time versus specific power input at feed position <1> (left) and <2> (right) for the bubble column (G) and the stirred tank (T).

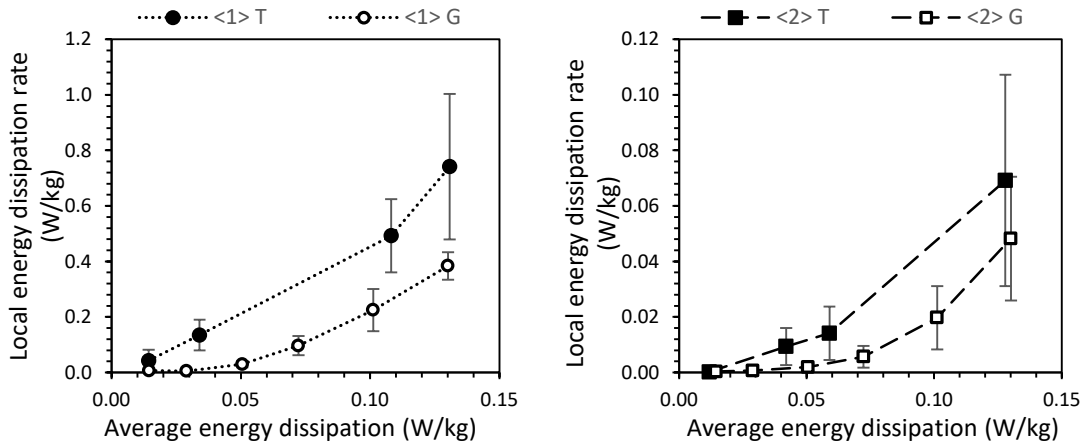


Figure 3.18 Local energy dissipation rate versus average energy dissipation rate at feed position <1> (left) and <2> (right) for the bubble column (G) and the stirred tank (T).

3.4 Conclusion

In this chapter, the Villermaux-Dushman reaction scheme was used to assess the micromixing performance of two systems: (i) a stirred tank equipped with a traditional Rushton turbine, and (ii) a bubble column equipped with a ring-shaped gas sparger. We measured the micromixing efficiency at two different points for each system, over a range of specific power inputs. One of the measuring points for each system is located in the area of the reactor which is expected to have the better micromixing performances, that is, into the trailing vortex generated by the Rushton turbine and right above the gas sparger, for our two investigated systems, respectively. The micromixing time has been estimated using the IEM model proposed by Villermaux and his co-workers. The system of equations describing the model was solved for the specific reactants' concentration set used in this work and for each chemical species involved in the mixing process. In this way, a relation between the segregation index and the micromixing time was found. Preliminary experiments were also performed for both systems in order to choose the suitable acid injection rate and eliminate the effect of meso-mixing on the final results. In addition, the volatility of the reactants was taken into account and the possible effects of their evaporation on the final results were assessed through additional preliminary experiments. In this regard, the outcome of the preliminary studies shows that evaporation has a negligible impact on the final results of the experiments.

The resulting micromixing times fall within the range typically reported for the stirred tanks ($10^{-2} - 10^{-1}$ s), for both systems. Interestingly, however, these values have been obtained at a relatively low power input and using simple experimental apparatuses when compared to other works present in the literature. This result was achieved by simply by feeding the reactants right next to the impeller's blades (for the stirred tanks) or to the bubble generation point (for the bubble column). This suggests that a very good micromixing can be achieved by carefully choosing the feeding point inside the reactor.

For both systems, we calculated the dimensionless energy dissipation rate by combining the experimental results and correlations from the literature. Our results show that the dimensionless energy dissipation rate increases with the specific power input in agreement with the theory that predicts an increased inhomogeneity in the energy dissipation when the average energy input is increased (in our case, when the stirring speed or the gas flow rate is increased). Comparison between the micromixing performance of the stirred tank and the bubble column leads to an interesting observation: although the turbine seems to produce a higher maximum energy dissipation, this effect is limited to the immediate vicinity of the impeller, while the presence of the gas produces a lower but more uniform energy dissipation. Therefore, in case of the bubble column, the micromixing efficiency seems to vary more gradually throughout the vessel.

Despite the inherent differences between the two systems analysed (stirred tank and bubble column), a careful analysis of the micromixing performance shows that the minimum micromixing time achievable (which corresponds to the best micromixing performance) is within the same order of magnitude for the stirred tank and the bubble column. This suggests that the value of minimum micromixing time that can be obtained in these two experimental configurations depends mostly on the average energy input provided, regardless of whether the agitation is provided by means of the stirrer or gassing.

Chapter 4

EFFECT OF FLUID

DYNAMICS ON NUCLEATION

OF PABA IN STIRRED

TANKS AND BUBBLE

COLUMNS

4.1 Introduction

Many crystalline compounds in pharmaceutical industry are produced through cooling crystallization in agitated tanks. Fluid dynamic conditions inside these reactors have profound influences on the crystallization process and can affect the metastable zone width, polymorphic form and crystal size distribution (Liu et al., 2015). In particular, although it is well known that mechanical perturbations can initiate nucleation in a clear solution, the role of fluid dynamics on primary nucleation is still unclear in the scientific community.

In this chapter, I aim to investigate the role of fluid dynamics on the crystallization process in unseeded solutions. For this purpose, I performed a series of cooling crystallization experiments using a batch crystallizer. The crystallizing solution inside the batch was mixed using two different devices: i) a mechanical stirrer, ii) bubbles produced by means of a gas sparger. This was to compare how different mixing techniques influence nucleation. The intensity of micromixing and local maximum energy dissipation rate for each system (stirred tank and bubble column) was evaluated in Chapter 3 and the results will be used in this chapter in order to investigate a possible link between energy dissipation rate and primary nucleation in agitated vessels. This will provide useful information for the understanding of the effect fluid dynamics on primary nucleation in solution.

4.2 Experimental

4.2.1 Materials

In order to investigate the effect of fluid dynamics on nucleation of molecules in solution, para-amino benzoic acid (PABA) was used as model compound; all the experiments were performed using water as solvent. PABA is a small organic molecule that has a carboxylic group and an amine group in para position, separated by an aromatic ring (Figure 4.1). It is mainly used in pharmaceutical industry, however it is also used in perfumes and dyes (Gracin & Rasmuson, 2004).

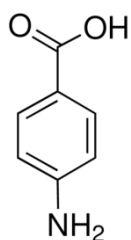


Figure 4.1 Para-amino benzoic acid (PABA) structure

PABA can crystallise into two well-known enantiotropic polymorphic forms: α , that crystallises in needle form (Figure 4.2 left), and β which has a prism shape (Figure 4.2 right); owing to their characteristic shapes, the polymorphs can be easily identified using a standard optical microscope. It is reported that α -PABA can be obtained from a number of solvents: water, acetonitrile, 2-propanol, ethyl acetate, methanol, ethanol etc.), while the β -form crystallises only from water and ethyl acetate (Gracin et al., 2005).

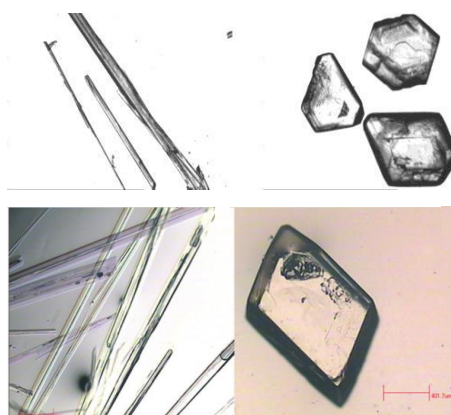


Figure 4.2 α (left) and β (right) para-amino benzoic acid (Gracin & Rasmuson, 2004; Sullivan & Davey, 2015)

Solubility of PABA in water was measured by Gracin & Rasmuson (2004). For this work, their solubility data was used (Table 4.1). It should be noted that, for all the crystallization experiments performed in this work, only the α -polymorph was obtained; therefore, all the results presented are relative to this polymorphic form. This result is consistent with what obtained by (Gracin & Rasmuson, 2004) who found that β -PABA forms spontaneously in the aqueous solution only at extremely slow cooling rates ($< 1^\circ\text{C/h}$).

Table 4.1 Solubility of α and β PABA in water (g_{PABA}/kg_{water}) (Gracin & Rasmuson, 2004).

Temperature [°C]	α -form	β -form
5	2.5	2.3
10	3	2.7
15	3.7	3.4
20	4.5	4.2
24	5.1	5.0
28	5.9	6.0
32	6.7	7.1
40	9.1	10.1
45	10.9	12.6
50	12.8	

4.2.2 Experimental setup

Figure 4.3 shows the experimental setup used: it consists of a batch cooling crystallizer. The crystallizer is a 2.3 L cylindrical transparent vessel (described in section 3.2.4) equipped with a cooling jacket. Water from a thermostatic bath (Huber MPC-K6, programmable) was circulated through the jacket to control the temperature. This allowed the crystallizing medium to cool down from 27 to about 16°C at a programmable cooling rate (0.1 °C/min for all the experiments performed in this chapter). The temperature of the solution was recorded to monitor the temperature profile. Two different mixing devices were used, i.e. a turbine and a gas sparger. The turbine is a standard 6-blades Rushton turbine (described in section 3.2.4); while the gas sparger (also described in section 3.2.4) provided agitation by generating a bubbles in the reactor. For sampling purposes, a plastic pipette was immersed into the suspension allowing to collect a few millilitres of solution. A conductivity meter (Mettler-Toledo, S230 SevenCompact) was used to measure the conductivity of the solution throughout the experiment. Figure 4.3 shows the complete reactor configuration used for the cooling-crystallization experiments for stirred tank and the bubble column reactor.



Figure 4.3 Reactor configuration for the crystallization experiments in the stirred tank (left) and bubble column (right); internal cylinder height is 200 mm; note that this setup is identical to the one described in Chapter 3 except for the conductivity probe which was not present for the experiments reported in Chapter 3.

4.2.3 Experimental procedure

For the experiment, the desired amount of PABA powder (purchased from Sigma-Aldrich in powder form) was dissolved into 1.5 L of DI filtered water (conductivity < 0.2 $\mu\text{S}/\text{cm}$, filter size 0.2 μm) and kept above the saturation temperature for 3 h to ensure complete dissolution of the crystals. After 3 hours had elapsed, we started to cool the medium at the selected cooling rate. Also, the electrical conductivity of the solution was recorded to monitor the progress of crystallization. For the experiments performed in the stirred tank, the rotational speed of the agitator was set and kept constant for the whole length of experiments; while in case of the bubble column experiments, the gas (nitrogen) was fed through the ring-shaped gassing unit, described in section 3.2.4, at constant flow rate for the whole length of the experiment. It was assumed that the bubbles moving inside the reactor provided enough agitation to ensure uniformity of temperature. This was verified by recording the temperature profile of the solution during each cooling crystallization experiment to confirm that it followed the desired one (a linear cooling rate profile was applied to all the experiments).

The electrical conductivity of the solution was measured online and recorded every minute using a conductivity probe immersed into the medium with the aim of monitoring the concentration of the solution (see section 4.3.1). For comparison purposes, for the experiments conducted in the bubble column, the conductivity was also measuring offline by collecting a few ml of the solution and filtering it (filter pore size 0.45 μm); the filtered liquid was transferred into a 4 dram vial and its conductivity and temperature were measured. This information was later used to calculate the solution concentration (the calculation procedure is presented in the next section) which was compared with the one obtained from the online measurements at the same point in time. From the comparison, it was concluded that the two techniques (online and offline conductivity measurements) gave the same result in term of concentration, therefore only online measurements were used. As soon as enough crystalline material had formed in the reactor, we collected a few ml of the slurry using a plastic pipette, the material was then filtered and dried in a ventilated laboratory fume cupboard. Crystals were then observed under an optical microscope in order to identify the polymorphic form obtained. For all the experiments described in this chapter only the α polymorph was obtained, therefore all the results refer to the α -PABA.

Table 4.2 Experimental conditions for the crystallization experiments

Solution volume	1.5 L
Solution concentration	5.744 $\text{mg}_{\text{PABA}}/\text{ml}_{\text{H}_2\text{O}}$
Cooling rate	0.1 $^{\circ}\text{C}/\text{min}$
Stirring rate	200-1000 rpm
N₂ flow rate	1 – 9 L/min

4.3 Results and discussion

4.3.1 Concentration determination from conductivity measurements

The electrical conductivity of diluted aqueous solutions of electrolytes is a function of both concentration and temperature. This property offers a relative simple way to monitor the

concentration of a crystallising solution. In order to determine the dependence of electrical conductivity on concentration and temperature, we measured the electrical conductivity of PABA aqueous solution of known concentrations over a range of temperatures. The results, shown in Figure 4.4, indicate that conductivity is linearly dependant on temperature, and the slope and the intercept of the fitting curves depend linearly on the concentration of the solution. Therefore, we used the following empirical equation to calculate the solution concentration from conductivity measurements

$$[PABA] = \frac{C - aT - b}{a'T + b'} \quad (4.1)$$

where [PABA] is para-amino benzoic acid concentration in $\text{mg}_{\text{PABA}}/\text{ml}_{\text{H}_2\text{O}}$, C is the electrical conductivity in $\mu\text{S}/\text{cm}$, T is the temperature in $^{\circ}\text{C}$ and a, a', b, b' are experimental parameters and are reported in Table 4.3. Using equation (4.1), it was possible to calculate concentration profile of PABA in solution for each experiment.

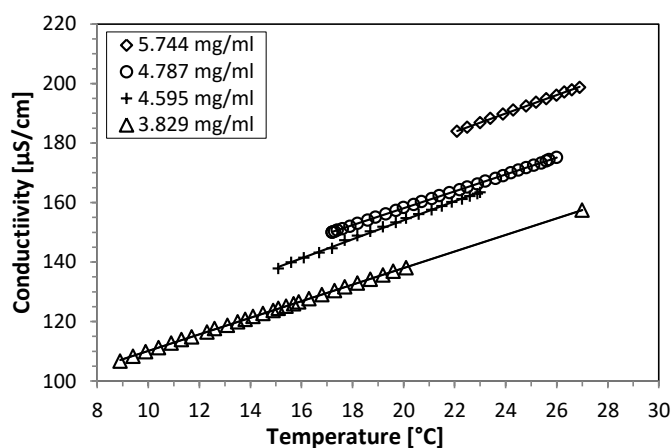


Figure 4.4 Electrical conductivity ($\mu\text{S}/\text{cm}$) of para-amino benzoic acid aqueous solution as function of temperature ($^{\circ}\text{C}$) and concentration (R^2 of fittings > 0.99); solution concentrations are reported in the legend as mg of PABA per ml of water.

Table 4.3 Fitting parameters of equation (4.1)

a	$2.2 \pm 0.26 \text{ mg}_{\text{PABA}} / ^{\circ}\text{C ml}_{\text{H}_2\text{O}}$
b	$35.6 \pm 6.6 \text{ mg}_{\text{PABA}} / \text{ml}_{\text{H}_2\text{O}}$

a'	1.5 ± 0.05 °C
b'	140 ± 1.4

Figure 4.5 (left and right) qualitatively shows the conductivity and concentration profiles obtained for each cooling crystallization experiment. It can be noticed that, as the temperature decreases the conductivity gradually decreases, while the concentration stays constant; on the other hand, the solution experiences a gradually increasing supersaturation. When the temperature reaches a critical value, the conductivity decreases more abruptly, and the corresponding concentration starts to decrease. This corresponds to the maximum supersaturation S_{max} reached by the solution, while the corresponding temperature is called *nucleation temperature* T_n and it identifies the metastable zone limit. The corresponding metastable zone width (MZW) and the maximum supersaturation are therefore defined as

$$MZW = T_{sat} - T_n \quad (4.2)$$

$$S_{max} = S(T_n)/S(T_{sat}) \quad (4.3)$$

where T_{sat} is the saturation temperature, that for the present work was kept constant and equal to 27°C, while T_n is the nucleation temperature. The nucleation temperature is taken as the temperature at which the decrease in concentration is larger than its random measurement fluctuations, calculated as the deviation from the nominal value observed before the onset of nucleation (constant section of the curve in Figure 4.5 right). As these fluctuations are estimated to be below 1%, and the nominal concentration of the solution at the beginning of each experiment is fixed at 5.744 mg_{PABA}/ml_{H₂O}, then the nucleation temperature is taken as the temperature at which the measured concentration drops below 5.687 mg_{PABA}/ml_{H₂O}.

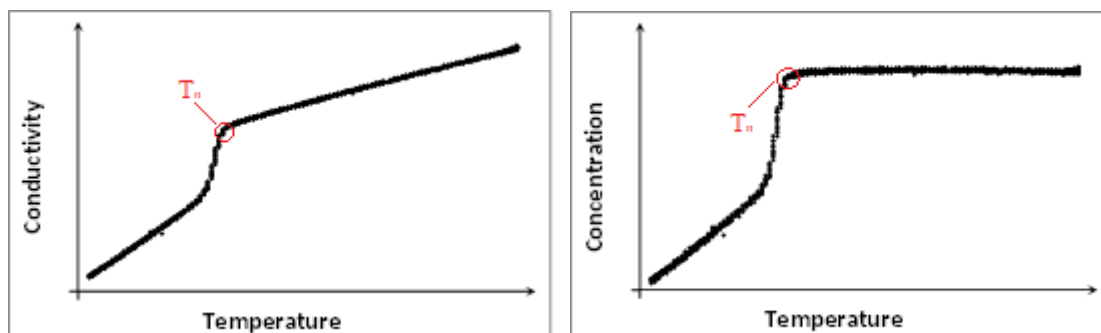


Figure 4.5 Qualitative trend of measured conductivity vs solution temperature (left), qualitative trend of solution concentration vs temperature calculated from the conductivity measurements using equation (4.1)

As the presence of crystals might alter the conductivity measurements by interfering with the probe used, offline measurements were also performed and compared with online measurements. In particular, for each experiment, a few ml of solution were withdrawn using a plastic pipette and filtered with a $0.2 \mu\text{m}$ filter in order to remove the crystals present, the samples taken were then kept at 28°C for one hour before measuring the electrical conductivity of the solution. Finally, the corresponding concentration values were calculated using equation (4.1) and compared to the ones obtained from the online measurements. As it is found that the difference in concentration from the online and the offline measurements is less than 1%, then we decided to use the online measurements for the MZW estimation.

4.3.2 Temperature profile

The temperature of the solution was recorded for the whole length of the experiment to ensure that the actual temperature profile corresponded to the desired one. In particular, for all the experiments we aimed to cool down the crystallising medium at a constant rate of $0.1^\circ\text{C}/\text{min}$. Figure 4.6 reports the measured temperature profile of the solution inside the crystalliser for the highest and lowest rotational rate of the impeller and the highest and lowest gas flow rate used in this work. It can be noticed that the experimental cooling rate closely follows the set one.

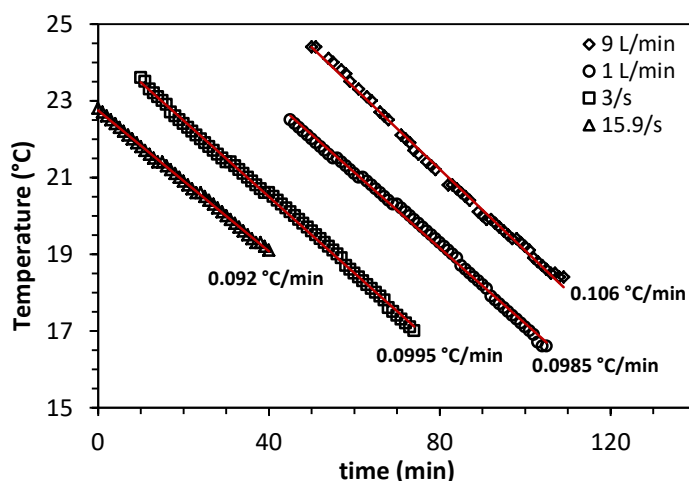


Figure 4.6 An example of the temperature profile of the solution during the cooling crystallization experiments measured for the highest and lowest stirring speed and highest and lowest gas flow rate used in this work; the slope of the best linear fit represents the experimental cooling rate and it is reported at the bottom of each curve (R^2 of fitting > 0.99).

4.3.3 Metastable zone width

As discussed in section 2.1.3, the determination of the metastable zone width is very dependent on the device used to detect the onset on crystallization. Because of sensitivity limitations, the conductivity probe is only able to detect a decrease in solution concentration after a significant amount of crystalline material has formed. Some authors suggest naked eye observations as a suitable method for MZW determination as, for slow cooling rates, it produces results very similar to the ones obtained using more complex techniques such as FBRM and ATR-FTIR with a good reproducibility (Nagy et al., 2008; Wohlgemuth et al., 2009). However, it should be noted that FBRM, ATR-FTIR, naked eye observations, conductivity measurements and so on are all indirect techniques that allow to detect the presence of crystals only after the nuclei have reached a certain size, or a certain amount of solute has crystallised. Despite this, it is reported that the ratio between the MZW determined using one of these indirect methods and the MZW that would arise if we would be able to detect the *true nucleation event* is constant as long as the same detection technique is used consistently (Kubota, 2008). For comparison purposes, in this work the nucleation temperature was recorded both using the conductivity measurements, described in section 4.3.1, and by naked eye technique; the corresponding metastable zone

widths are identified as MZW_C and MZW_E respectively. Some differences are obviously expected between the experimental MZW obtained with these two detection techniques due to the different sensitivity of the human eye and the conductivity meter. In particular, as discussed above, at least 1% change in concentration is required in order to detect the onset on crystallization from the conductivity measurements; on the other hand, it is estimated that the resolution of human eye is about $50 \mu\text{m}$ (depending on the light, contrast etc.), which is order of magnitudes larger that the critical nucleus size. However, the ratio between MZW_E and MZW_C is expected to be constant for the reasons discussed above.

4.3.4 Effect of impeller rotational speed

Using the experimental procedure described above, a number of crystallization experiments have been performed using a Rushton turbine as means to provide agitation in the reactor. Figure 4.7 (left) shows the concentration profiles for experiments performed at different agitation rates. Concentration measurements have been performed by means of a conductivity probe as described in section 4.3.1. Figure 4.7 (right) shows the corresponding supersaturation profile during the cooling-crystallization experiments.

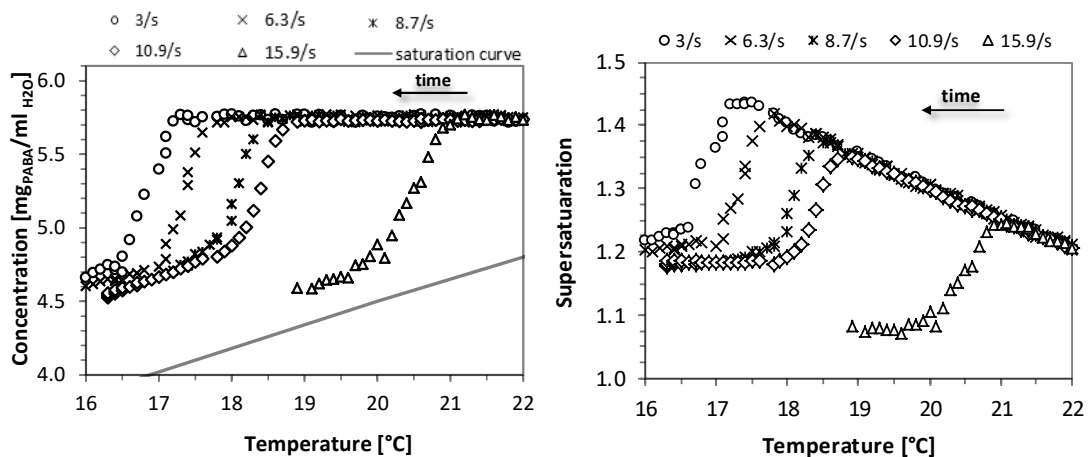


Figure 4.7 Solution concentration, in mg of PABA per ml of water (left), and supersaturation (right) vs temperature for the cooling crystallization experiments performed in the stirred tank for various stirring rates.

Based on the results shown in Figure 4.7, the concentration profiles show the following trend: the concentration of the solution stayed unchanged and equal to the initial concentration for a certain amount of time after the beginning of cooling; when a certain amount of crystalline material formed, the concentration started to decrease below the nominal value, this event corresponds to the onset of nucleation and the corresponding nucleation temperature was used to calculate the MZW_c (eq. (4.2)); at this point the concentration decreased quite abruptly approaching the solubility curve, while supersaturation reached an “equilibrium” final value. This final “equilibrium” value of the supersaturation results from a balance between the cooling rate and rate at which new crystalline material was formed in the solution. It can be noticed that there was not a significant difference between the way the concentration profile approached the saturation curve for the different stirrer speeds used in the experiments, showing that, once the first crystallites were formed, secondary nucleation caused a crystallization avalanche that quickly brought the solution in an equilibrium condition, close to the saturation point. However, we can notice that the final supersaturation value reached by the solution decreased as the stirrer speed was increased showing that a higher agitation intensity is beneficial in bringing the solution closer to the equilibrium point so that a larger amount of crystalline material is formed. It is reported in the literature that growth rate of α -PABA in water is not controlled by mass transfer but rather by the rearrangement of the solute molecules on the crystal surface (Turner et al., 2016), therefore it is not expected to be affected by fluid dynamics. For this reason, the decrease of the final supersaturation level reached here when the stirring speed is increased has been attributed to a larger number of nuclei being formed rather than to an increased growth rate (i.e. larger crystals). Figure 4.8 shows three different moments of the crystallization experiment: the clear solution at the start of the experiment, when the temperature is still above the saturation level; the solution at the *cloud point*, when a considerable amount of crystalline material has formed; and the solution when about 20% of the solute is present in crystalline form, at the end of the experiment.

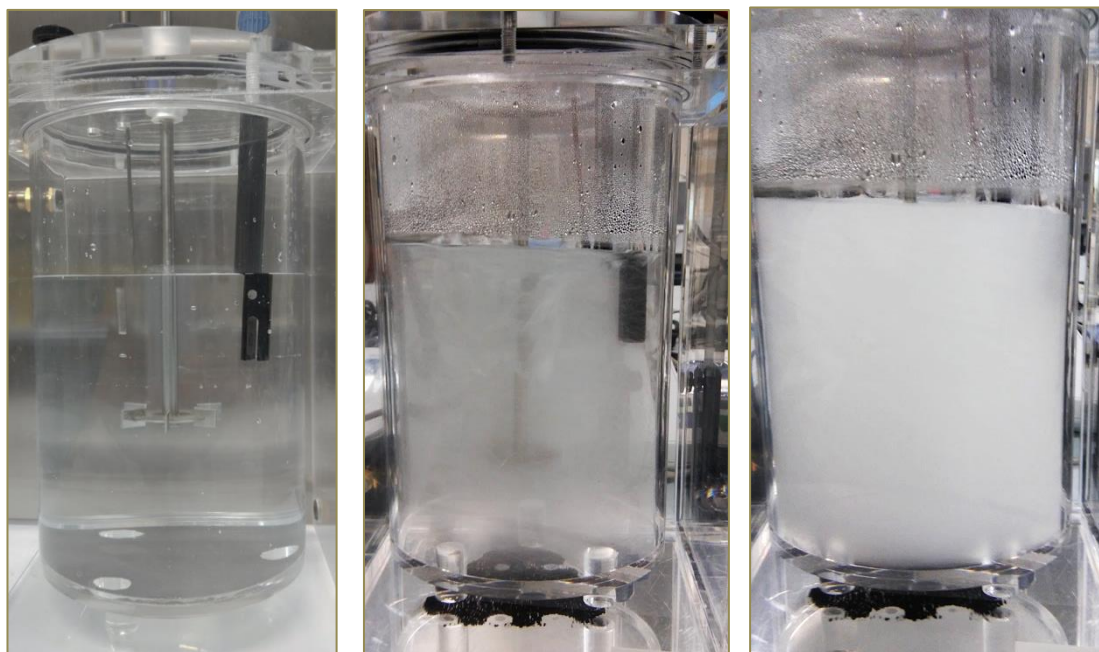


Figure 4.8 Batch reactor containing: clear, uncrystallised solution (left); crystallizing solution at *cloud point* (centre); crystallization solution after $\sim 20\%$ of solute has crystallized (right).

Microscope images of the crystals produced during the experiments are depicted in Figure 4.9. The polymorph obtained is clearly identifiable as the α -polymorph due to its distinctive needle shape, as opposing the prism shape that characterises the β -polymorph. The crystals were mainly present as agglomerates.

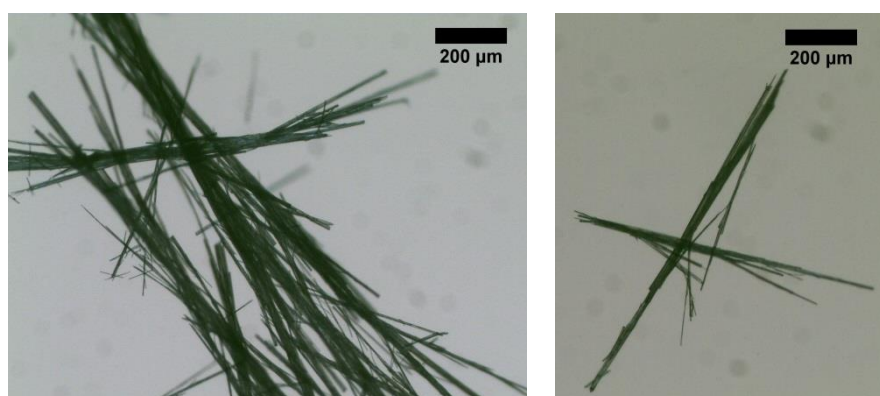


Figure 4.9 Microscope images of α -PABA crystal obtained via cooling crystallization.

Figure 4.10 summarises the values of the metastable zone width obtained through conductivity measurements and naked eye observations for the experiments conducted in the stirred tank; each point is obtained as the average of three repeated experiments. In both cases (MZW_C and MZW_E), I observed a decrease of MZW as the stirring rate was increased. This result is similar to that obtained by other authors (e.g. Kubota, 2008; Mitchell et al., 2011) who observed that the metastable zone width narrows as agitation in the system is increased. Figure 4.10 also shows that the metastable zone widths evaluated from naked eye observations (MZW_E) are narrower than the ones obtained from the conductivity measurements (MZW_C). However, the difference between these values (MZW_C and MZW_E) is small, and suggests that the time lapse between the true nucleation event and the so-called *cloud point* (Figure 4.8, right) is small. Despite this, as expected, they both follow the same trend, showing that both methods give consistent results. It is worth noticing that MZW_E experimental values exhibit a slightly higher variability (as shown by the error bars) than MZW_C ; that indicates that, although we are able to detect the nucleation event earlier by naked eye observations, conductivity measurements give more consistent results as they are less dependent on the operator and environmental conditions (light, reflection, eye sensitivity etc.). For this reason, in section 4.3.6 we will only use the values obtained from the conductivity meter to discuss the relation between shear rate and nucleation.

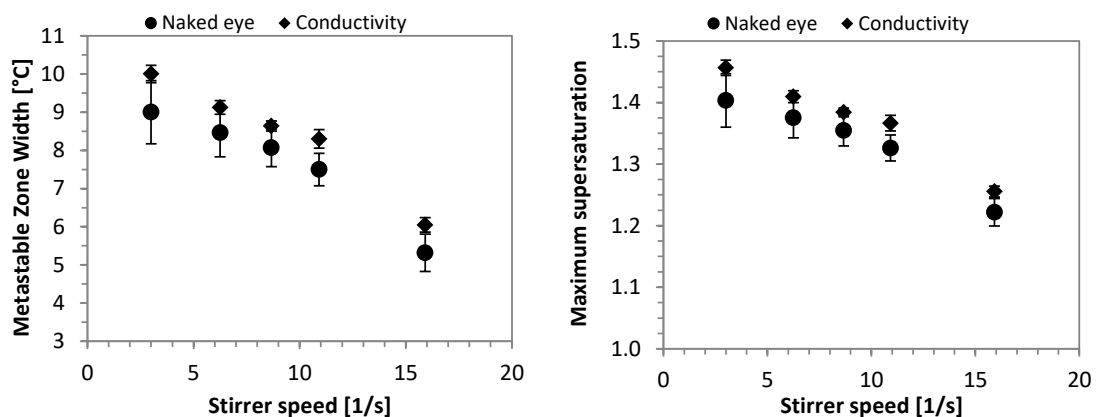


Figure 4.10 Metastable zone width (left) and maximum supersaturation S_{max} (right) measured by *naked eye* and *conductivity meter* for different stirrer speeds.

4.3.5 Effect of the gas flow rate

Figure 4.11 shows the concentration profiles for the experiments performed in the bubble column. As in the previous case, the solution stays stable for a certain period after the temperature drops below the saturation point; when the solute starts to crystallise, the solution concentration starts to decrease and the experimental curve approaches the saturation curve (Figure 4.11 left). It can be noticed that the decrease in concentration is less sharp than the one observed when the system is agitated by means of a Rushton turbine, particularly for the lowest gas flow rate used in this work; this is particularly evident when comparing Figure 4.11 (right) and Figure 4.7 (right). This result is probably due to the fact that bubbles produce a gentler agitation, so secondary nucleation is hindered, producing a more gradual decline of supersaturation. However, as the agitation is increased, by adjusting the gas flow rate, the concentration profile shows a sharper decline, similar to that observed for the experiments conducted in the stirred tank, showing that higher agitation is increasing the effect of secondary nucleation leading to a faster drop in the solute concentration. For the reasons discussed above, this effect cannot be attributed to an increased crystal growth rate because it has been demonstrated that growth rate of α -PABA in water is controlled by the incorporation of the solute molecules to the crystal lattice and is, therefore, expected to be independent from the fluid dynamic surrounding the crystal (Turner et al., 2016). Figure 4.12 summarises the results obtained in terms of metastable zone width and maximum supersaturation as function of the gas flow rate. Overall, a general decrease of MZW is observed as agitation is increased, however, unlike the previous case, when the gas flow rate is increased beyond a certain level, metastable zone width seems to reach a plateau and stay approximately constant; the same trend is obviously observed for the dependence of critical supersaturation on gas flow rate. This suggests that beyond a certain point, the increase in the gas flow rate is no more beneficial in reducing the MZW. Because a plateau is not reached in case of the stirred tank, it is unclear if the minimum value of the MZW observed here for both cases (about 5 °C) represents a physical limit of the system or it could be possibly reduced further by increasing the stirring speed. As regards the different MZW detection methods, we observe again a small difference between MZW_E and MZW_C due to the different sensitivity of the two detection techniques; however, the ratio between the two stays approximately

constant as the two variables follow a similar trend. At high gas flow rates (≥ 5 lt/min), the error bars show a higher variability in the MZW values when they are determined by naked eye; this is due to an increased difficulty in spotting the crystals inside the reactor as the amount of bubbles increases.

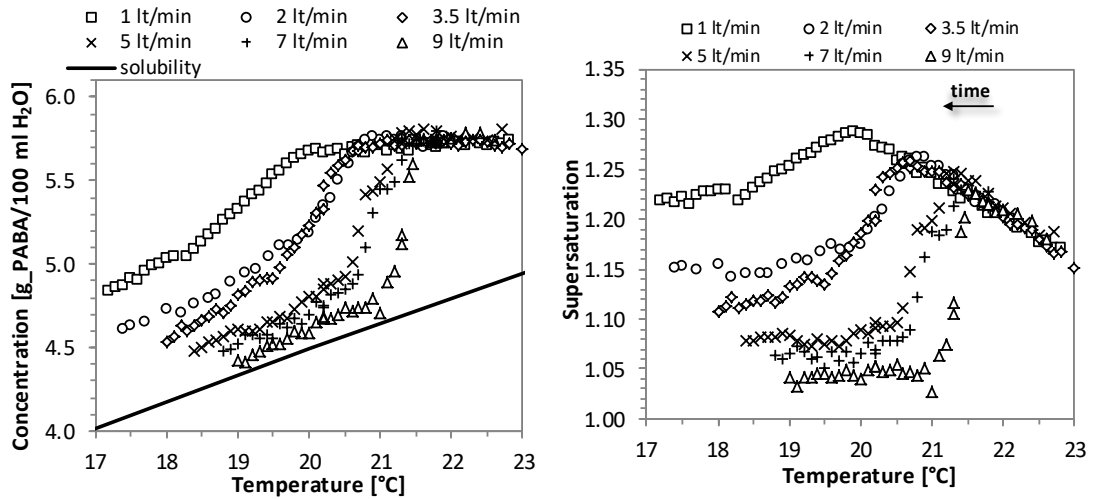


Figure 4.11 Concentration profile (left) and supersaturation profile (right) vs temperature for the experiments performed in the bubble column.

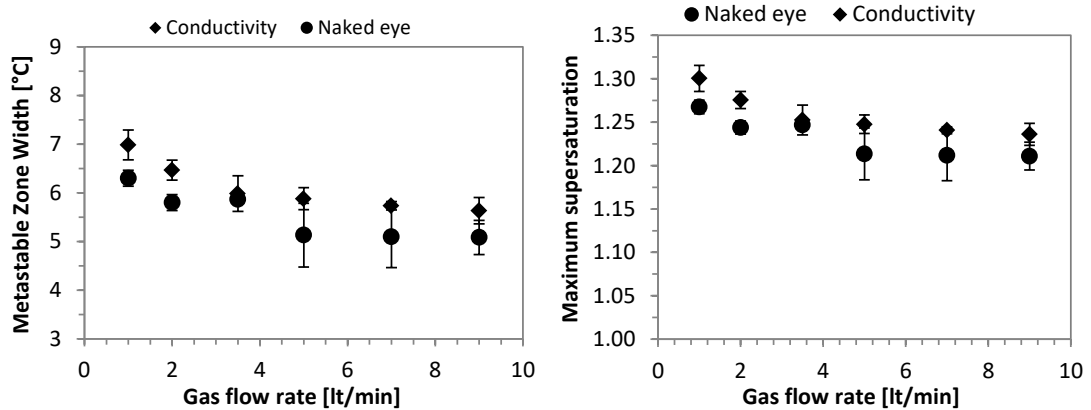


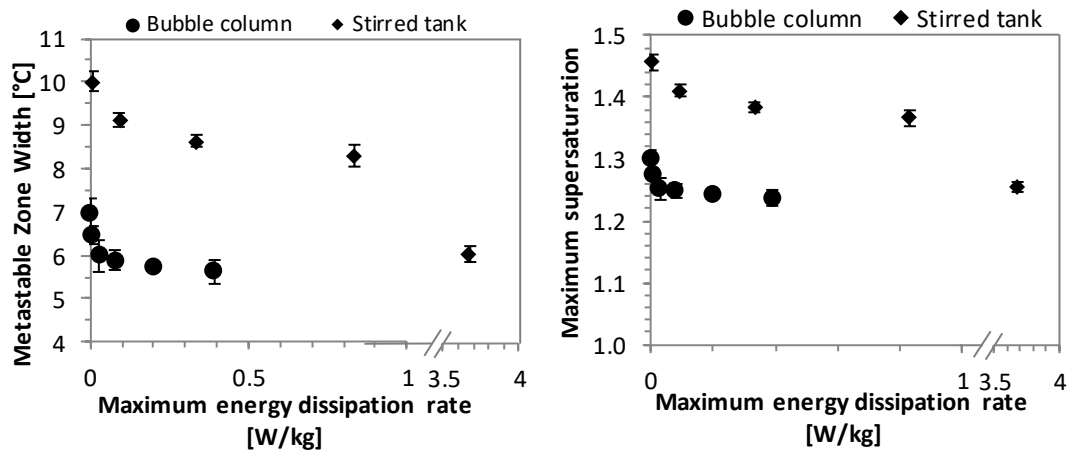
Figure 4.12 Metastable zone width (left) and maximum supersaturation (right) measured by *naked eye* and *conductivity meter* for different gas flow rates.

4.3.6 Effect of local fluid dynamic conditions

In the attempt to identify the parameters controlling nucleation in agitated system I used the information about the micromixing and local energy dissipation rate ε obtained in Chapter 3 for the stirred tank and the bubble column used. In particular, in Chapter 3, I showed that the local energy dissipation rate strongly depends on the local fluid dynamic conditions. In particular, in the stirred tank ε was about 1 order of magnitude larger when measured very close to the stirrer tip than when I measured a few centimetres away in the radial direction, within the impeller speed range analysed. This confirms that the fluid dynamic conditions in the stirred vessel are quite non-uniform. In contrast, when the system is agitated by means of bubbles the local energy dissipation rate seems vary more gradually, suggesting that the system is more uniform from the fluid dynamic point of view. As pointed out by (Liu et al., 2014), nucleation is considered to be an activated process and it is, therefore, expected to take place in the point of the reactor that has the most favourable conditions. For this reason, if we assume that the intensity of micromixing and the local fluid dynamic conditions are governing the process, as suggested in the literature (e.g. Forsyth et al., 2015; Liu & Rasmuson, 2013; Liu et al., 2014, 2015) and discussed in section 2.2.7, we can expect that crystals will first form in the area of the reactor characterized by the highest local energy dissipation rate. On the other hand, it must be pointed out that these conditions (high turbulence) is only experienced by a small fraction of the total solution volume; in such a small volume, nucleation might assume a stochastic nature and the probability that a stable nucleus will form in the time lapse considered might be relatively low. To investigate this hypothesis, Figure 4.13 shows the results of the experiments performed in this chapter for the stirred tank and the bubble column in terms of metastable zone width and maximum supersaturation as function of both average energy dissipation rate (specific power input) and maximum local energy dissipation rate (corresponding to position <1> in the experimental apparatuses characterised in Chapter 3 and used here to perform the cooling crystallization experiments). For the reasons previously discussed, the MZW values reported here refer to the conductivity measurements. Maximum local energy dissipation rate is calculated through equations (3.20) and (3.21) (relative to position <1>) for the stirred tank and bubble column

respectively; while average energy dissipation rate instead is calculated through equations (2.64) and (2.66) for the stirred tank and bubble column respectively.

Although the results clearly show that the metastable zone width narrows as agitation is increased, both in case of the stirred tank and the bubble column experiments, energy dissipation rate seems not to be the parameter that controls the onset of nucleation as the MZW measured in the two systems appears to be significantly different for the two systems at similar values of the energy dissipation rate. This is true both when the results are plotted against the maximum (equations (3.20) and (3.21), position <1>) and the average values (equations (2.64) and (2.66)). Therefore, these results seem to contradict the hypothesis that the local fluid dynamic conditions and micromixing controls nucleation. If the hypothesis was correct, I would in fact expect that the metastable zone width measured would be the same for a certain value of energy dissipation rate (either local maximum or average), regardless if agitation is provided by means of bubbles or a stirrer. However, it is interesting to notice that the decrease in the MZW is approximately the same (about 1.5 °C) in the two systems if the same energy dissipation rate interval (local maximum or average) is considered, showing that when the turbulence is intensified the MZW narrows in a similar way regardless if agitation is provided by means of two different devices (Figure 4.13).



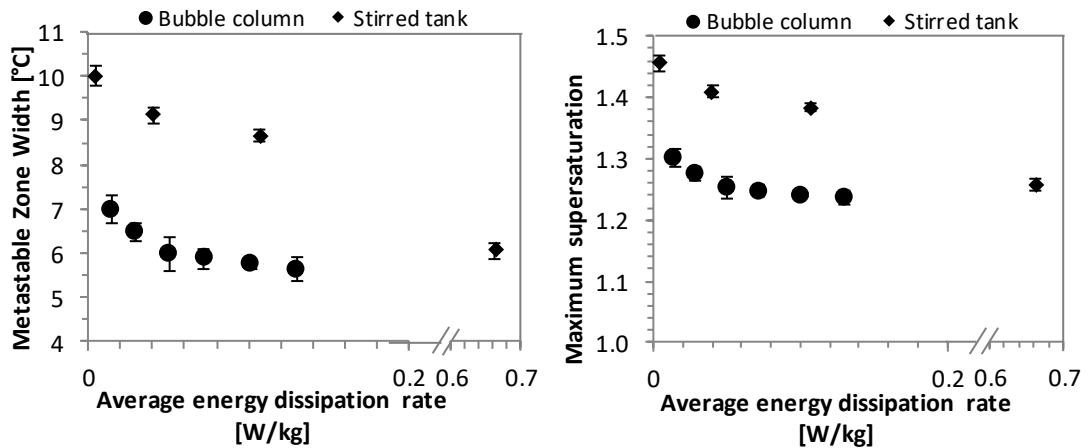


Figure 4.13 Metastable zone width and maximum supersaturation for the *stirred tank* and *bubble column* crystallization experiments vs local maximum energy dissipation rate (left) (equations (3.20) and (3.21)), and average energy dissipation rate (right) (equations (2.64) and (2.66))

These our results seem not to confirm the hypothesis that energy dissipation rate is the factor that controls the onset of nucleation in mixed vessels, it is difficult to draw a definitive conclusion based on these data because, as discussed in Chapter 3, the systems studied are highly non-uniform, so different areas of the vessel experience very different fluid dynamic conditions. In particular, energy dissipation rate is very high in the vicinity of the impeller, while it decreases abruptly only a few centimetres from it (Figure 3.11 and Figure 3.15 for stirred tank and bubble column respectively), showing that only a small portion of the solution is actually experiencing intense turbulence. In addition, as discussed in section 2.2.5, the turbulence generated in a bubble column is inherently very different from that found in a stirred tank; in particular, the intermittent nature of *bubble induced turbulence* can influence crystals formation in an unpredictable way.

As inferred by some authors (e.g. Wohlgemuth et al., 2009), the reduction of metastable zone width observed in presence of bubbles might be attributed to the enhancement of heterogeneous nucleation triggered by the bubble surface. If we assume that the gas-liquid interface has the potential to act as a heterogeneous surface for nucleation, we might indeed expect a significant reduction of the MZW in presence of the bubbles. This explanation seems to be compatible with what was observed in the experiments performed here, where the MZW was significantly reduced by injecting bubble in the system whilst the shear rate does not exhibit a significant change. As the gas flow rate is increased, more gas-

liquid surface becomes available thereby increasing the chances of nucleation; therefore, the higher the gas flow rate the narrower the MZW is expected. However, it should be considered that, as the gas flow rate was increased, the number of bubbles actually present in the solution is expected to reach a plateau (Murugesan, 1998), and a further increase in the gas flow rate is not beneficial in creating more gas-liquid surface. For this reason, if we assume that nucleation is triggered by the gas-liquid interface, then we would expect that the MZW is independent of the gas flow rate when that is increased beyond a certain point. This reasoning is in agreement with these results that show that the MWZ narrows as the gas flow rate is increased but then it reaches a plateau, where a further increase of gas flow rate does not translate in an additional reduction of the MZW.

Thus my observations seem to be in agreement with the hypothesis that the gas-liquid interface acts as a heterogeneous nucleation site, however, it is difficult to draw a definitive conclusion based on these data. The reason is that, on one hand, it should be kept in mind that fluid dynamic conditions inside a stirred tank or a bubble column are extremely complex and non-uniform and it is challenging to find a link between fluid dynamics and nucleation, while on the other hand, direct observations of nucleation on a gas-liquid surface are extremely difficult; therefore, it is not possible to exclude either hypothesis on the basis of the results presented above.

4.4 Conclusion

In this chapter, I investigated how agitation can influence nucleation in cooling crystallization experiments of PABA in water. For this purpose, I employed a Rushton turbine and a gas sparger as means to agitate the crystallising solution. In order to determine the onset of nucleation, which marks the metastable zone limit, I used conductivity measurements coupled with naked eye observations. The results show that, although both techniques represent indirect methods to determine the nucleation event, they provide similar results. However, the conductivity measurements proved to be more reliable as they are less prone to experimenter-dependant errors.

The results obtained show that metastable zone width can be effectively reduced by increasing the agitation in the system, in my case by increasing the stirrer speed or the gas

flow rate for the stirred tank and bubble column respectively. By looking at the concentration profile curves after the nucleation point for the two systems analysed (stirred tank and bubble column), a sharper decrease in the solution concentration was observed when the system was agitated via the Rushton turbine, probably caused by a strong effect of secondary nucleation triggered by the stirrer; while the concentration decreases more gradually when the solution is agitated by means of a gas phase (bubble column). However, as we increase the gas flow rate we can notice a more abrupt decrease in the solution concentration, showing an increasing impact of secondary nucleation, similar to that observed for the stirred tank. This effect cannot be attributed to an increased growth rate as, for a PABA-water system, growth rate is not mass transfer limited and therefore it cannot be affected by fluid dynamics (surface-integration controlled growth mechanism). By combining the results obtained here with the ones obtained in Chapter 3, I have investigated the hypothesis that micromixing and energy dissipation rate are the parameters controlling primary nucleation in agitated systems. In particular, in Chapter 3, I estimated the maximum local value of the energy dissipation rate as well as its average value both for the stirred tank and the bubble column; while in this chapter, I aimed to find a correlation between those parameters and the metastable zone limit of the system. The results relative to the cooling crystallization experiments, however, did not show any significant relation between energy dissipation rate, either maximum or average, and the metastable zone limit. In fact, I observed that when the two systems (stirred tank and bubble column) are subject to the same values of ε (either average or maximum), the metastable zone width is significantly different. Although on the basis of these results one cannot conclude that either local micromixing or energy dissipation rate are the parameters controlling primary nucleation in agitated systems. However, it is clear that fluid dynamics in a stirred tank or a bubble column is very complex and highly non-uniform (as also shown in Chapter 3) and therefore, it is difficult to assess its influence on the nucleation process. For this reason, I cannot discard the hypothesis that the intensity of turbulence and local micromixing phenomena play a fundamental role in determining the MZW during cooling crystallization. Another possible explanation for the different MZW measured for the two experimental systems is that, as some authors have hypothesised, the gas-liquid interface provided by the bubbles might act as a site for heterogeneous nucleation, thereby lowering

Chapter 4

the energy barrier needed to initiate nucleation and leading to a narrower MZW. Although this hypothesis seems plausible and in agreement with these results, this cannot be confirmed without further investigation that allows to untangle the effect of the various parameters (shear field and gas bubbles) on primary nucleation. This hypothesis will be investigated in Chapters 5 and 6.

Chapter 5

EFFECT OF SHEAR RATE ON NUCLEATION KINETICS OF PABA IN MILLICHANNELS

5.1 Introduction

In the previous chapter, I investigated the effect of agitation on the primary nucleation of PABA dissolved in water. In particular, I showed that increased agitation leads to a narrower metastable zone width; however, it is unclear whether this effect can be attributed to an increased energy dissipation rate and micromixing phenomena affecting the crystals formation mechanism, heterogeneous nucleation on gas-liquid surface or the inherently different nature of turbulence (*true turbulence versus bubble induced turbulence*) generated in the two systems analysed. In this regard, microfluidic devices represent a useful tool to study primary nucleation in well-controlled fluid dynamic conditions (Leng & Salmon, 2009) using the *double pulse* technique (separation of nucleation and growth stages) introduced in section 2.1.5. In addition, owing to the small volume of fluid they hold, temperature in these devices can be uniformly controlled, and so, rapid changes of supersaturation can be achieved much more easily than in large scale systems. Microfluidic chips, however, often lack of flexibility as they have a fixed geometry and their fabrication process is expensive; lately some authors have proposed polymeric flexible capillaries as a valid alternative to microfluidic chips (Rossi et al., 2015) as they have all the advantages of conventional microfluidic chips but they are relatively inexpensive and offer a much greater flexibility to the experimenter.

Therefore, I decided to investigate primary nucleation of PABA in water under quiescent-stagnant conditions and low shear-laminar conditions using a polymeric transparent capillary crystalliser applying the *droplet method* briefly described in section 2.1.4, together with the *double pulse technique*. The results were then compared with the ones obtained by Sullivan (2015) under high-shear turbulent flow using stirred vials. This permitted investigation of primary nucleation under a wide range of shear rates and will contribute to the understanding of the role of fluid dynamic in the nucleation of small molecules in solution.

The material for this chapter has been published in Chemical Engineering Research and Design:

Nappo, V., Sullivan, Davey, R., Kuhn, S., Gavriilidis, A., Mazzei, L. (2018) Effect of shear rate on primary nucleation of para-amino benzoic acid in solution under different

fluid dynamic conditions. *Chemical Engineering Research and Design*, 136, 48-56. doi.org/10.1016/j.cherd.2018.04.039.

5.2 Experimental

5.2.1 Materials

In this chapter I investigated the effect of shear rate on primary nucleation rate of para-amino benzoic acid (PABA) dissolved in water. PABA chemical structure and crystal habit was discussed in section 4.2.1. As for Chapter 4, I used the solubility data of Gracin & Rasmuson (2004) while the MZW has been measured again for my experimental setup and procedure; the results obtained showed that for a PABA-water solution saturated at 27 °C the MZW is 4 °C. This means that we can assume that at 23 °C no nucleation or dissolution occurs in the time interval considered. Details about the experimental procedure used to determine the MZW can be found in Appendix C. Aqueous solutions of PABA (Sigma-Aldrich, 99% purity) were prepared using filtered deionized water (filter pore size 0.2 µm, conductivity < 0.2 µS/cm). Heptane (CH₃(CH₂)₅CH₃, Sigma Aldrich, anhydrous, 99% pure) was used as carrier phase for droplet formation in the capillary tube and was also used without further purification. The segmented flow pattern was obtained using a PEEK T-junction (IDEX, internal diameter 0.5 mm) and the droplets were stored in a transparent PTFE flexible capillary (IDEX, internal diameter 1 mm, outer diameter 1.58 mm).

5.2.2 Experimental setup and procedure

Crystallization experiments of PABA in water were performed using *droplet method*, briefly described in section 2.1.5 where primary nucleation is studied using a large number of small droplets of supersaturated solution produced by means of a microfluidic system. Each droplet represents an independent batch crystalliser where nucleation exhibits its stochastic nature due to the small volumes of solution considered and it is, therefore, modelled using a statistical approach. In these conditions, nucleation rate is assumed to follow a Poisson distribution, therefore it is modelled according to equation (2.30). Experiments were performed under *stagnant conditions* (motionless droplets) and *flowing*

conditions (droplets flowing inside the channel at constant speed). As discussed in section 2.3, when a liquid droplet is moving inside a microchannel surrounded by an immiscible phase, two counter-rotating vortices arise inside the droplet so that a gentle shear is generated. A PABA aqueous solution saturated at 27°C was prepared by dissolving 574.4 mg of PABA in 100 ml of filtered deionised water; the solution was kept at about 50°C for several hours in order to ensure the complete dissolution of the material. After that, monodispersed droplets of the solution were generated with the aid of a carrier phase (heptane) using a PEEK T-junction connected to long PTFE capillary (about 4 m). Heptane has been chosen because it is completely immiscible with water.

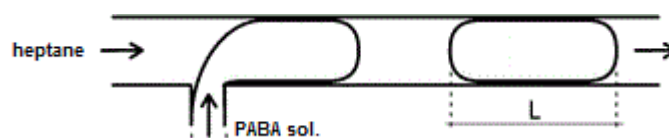


Figure 5.1 PABA aqueous solution droplet formation (carrier phase: heptane)

The fluids (PABA aqueous solution and heptane) were filtered using online PCTFE (polychlorotrifluoroethylene) filters (filter size 2 μ m) positioned before the T-junction and fed into the PTFE capillary using a Harvard syringe pump (PHD 2000 programmable). The T-junction allowed creation of a segmented pattern in which the droplets of the crystallising solution were kept separated by the carrier phase (heptane) as shown in Figure 5.1. Due to the hydrophobic nature of the channel, the heptane forms a thin liquid layer around the aqueous droplets preventing them from touching the channel walls. The absence of solid surfaces in contact with the crystallizing solution is beneficial as it decreases the chances of heterogeneous nucleation leading to a more accurate estimation of the primary nucleation rate; in addition, it prevents the clogging of the channel that can be caused by crystals growing on the channel walls during the experiments in flow conditions (moving droplets). Due to the channel wettability and the fluids properties the water droplets assume the characteristic bullet shape shown in Figure 5.2.

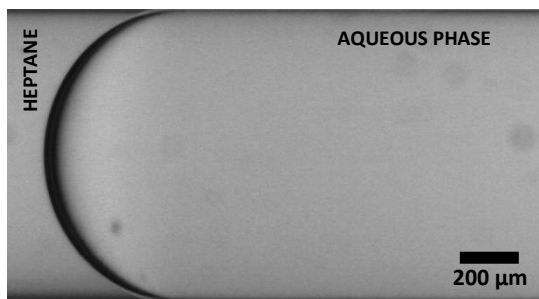


Figure 5.2 Water droplet in a 1 mm I.D. PTFE channel (heptane carrier phase)

Figure 5.3 shows the schematic of the experimental setup. The droplets were generated within a Perspex enclosure which was kept above the saturation temperature ($T_1 > T_{\text{sat}}$) in order to prevent undesired crystallization during the experiment preparation. For the experiments under *stagnant conditions*, after the droplets had filled the whole length of the channel, both ends of it were sealed and the plastic capillary was immersed into the water bath at T_n (*nucleation section*). The time t_n during which the droplets were kept in the *nucleation section* was fixed a priori. After that, the droplet array was manually moved into the *growth section* at T_g for an additional time t_{gE} . Temperature has a strong influence on crystallization, and so its precise control is crucial in the investigation of the kinetics of the process. In these experiments, the temperature in the *nucleation* and *growth sections* was kept constant using two water baths (Huber, MPC-K6 programmable), while in the *droplet generation section* a fan heater kept the temperature a few degrees above the saturation level.

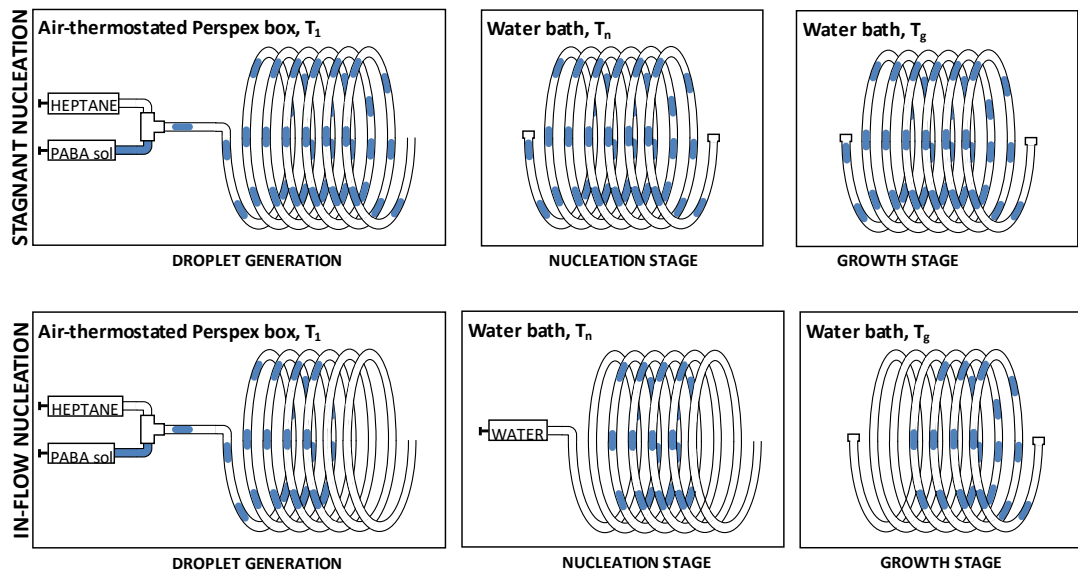


Figure 5.3 Schematic of the experimental setup used in this work for the quiescent conditions (stagnant nucleation) and flowing conditions (in-flow nucleation) experiments.

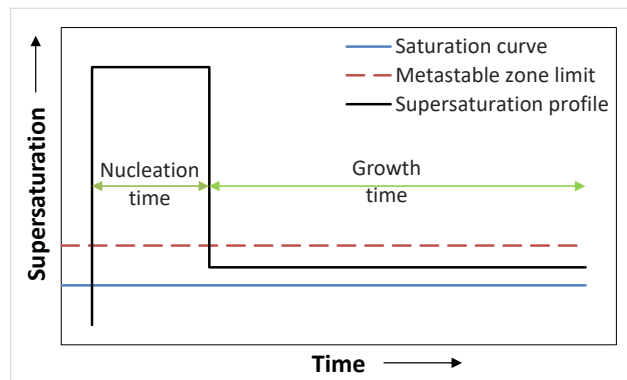


Figure 5.4 Qualitative representation of the specific supersaturation ratio profile used.

Figure 5.4 shows the supersaturation profile used in the experiments. The temperature (T_g) of the *growth stage* was carefully chosen to be within the metastable zone to allow the growth of the nuclei formed during t_n while preventing further nucleation or dissolution. The reason is that, after the *nucleation stage*, the droplets might contain crystals that are too small to be detected. Therefore, to estimate correctly the number of droplets in which at least one stable nucleus has formed during the *induction time*, we let the nuclei grow until they reached a detectable size. This allows us to achieve the separation of the

nucleation from the growth stage and thereby to set t_g to zero in equation (2.30). As a consequence, for our specific experimental procedure results $t_n = t_i$. The *experimental growth time* (t_{GE}) should be long enough that its length does not affect the outcome of the experiments. After a range of *experimental growth times* was investigated, we set t_{GE} to be at least twice as large as the *nucleation time* (t_n).

After the *experimental growth time* had elapsed, I observed the droplets using an optical microscope (Olympus IX50) and I counted the number of droplets containing at least one crystal. This procedure was used to determine the experimental probability distribution of *induction times* $P_E(t_i, V, S)$, as defined in equation (2.31). Polymorphs were identified by visual inspection. Although PABA crystallizes into two polymorphic forms (α and β), in all these experiments only the α -polymorph was obtained, so all the results presented in this chapter are related to the α -polymorph. In order to improve the quality of the images the PTFE capillary was immersed in a small Perspex container filled with water as shown in Figure 5.5. Because Perspex, water and PTFE have very similar refractive indices, this technique corrects the optical distortion caused by the curvature of the tubing and to obtain very clear images. The tubing is moved manually through the Perspex box so to pass each droplet in front of the microscope's lens (Figure 5.6).

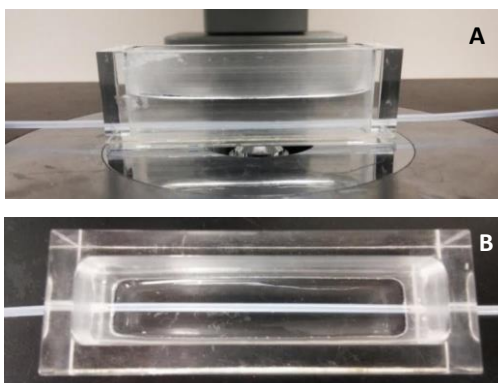


Figure 5.5 PTFE tubing (IDEX, 1 mm I.D., 1.58 mm O.D.) immersed in a custom Refractive Index Matching (RIM) device filled with water; (A) side, (B) top

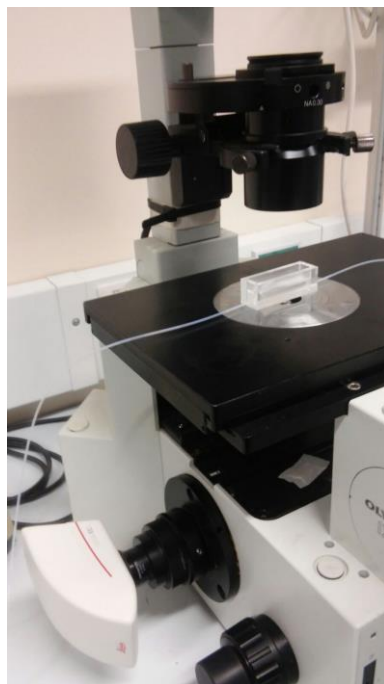
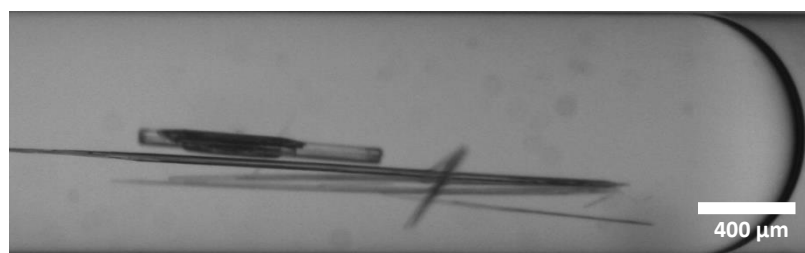


Figure 5.6 PTFE tubing (DEX, 1 mm I.D., 1.58 mm O.D.) immersed in a custom Refractive Index Matching (RIM) device filled with water placed under the microscope (Olympus IX50), a digital camera (Leica EC3) is connected to the microscope to capture images of the droplet inside the tubing.

Although this method allowed us clear identification of the crystals inside the droplets, it was difficult to establish how many crystals are in each droplet as they tend to agglomerate and/or optically overlap (Figure 5.7). However, as already discussed in section 2.1.5, the focus is on whether a droplet contains crystals or not, therefore this does not represent an issue for the present investigation.



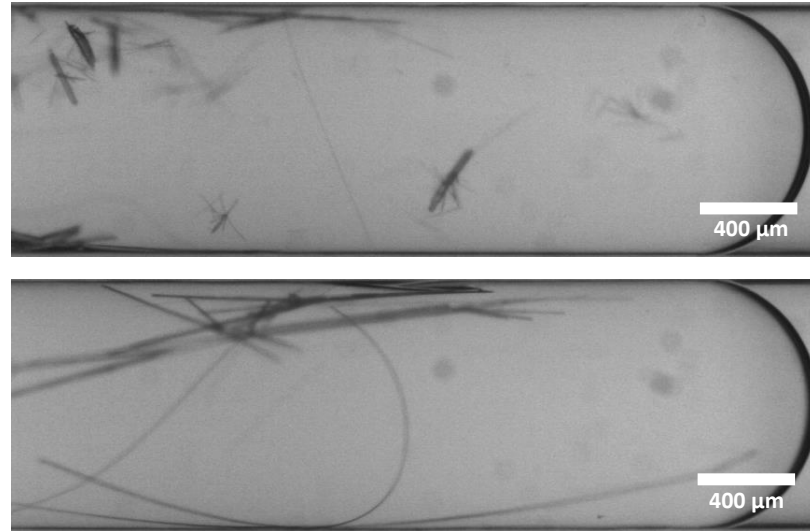


Figure 5.7 Aqueous droplets containing α -PABA crystals

I connected a digital camera (Leica EC3) to the microscope to take pictures of the droplets. The pictures were then analysed using a Matlab® customised routine (Appendix D) that calculates the volume of each droplet as the volume of the solid of revolution obtained by rotating the curve representing the droplet boundary about the horizontal axis. The script also calculates the mean and standard deviation of the droplet volume distribution for each experiment. It should be noted that, for the volume calculation, it was assumed that each droplet is axisymmetric along the horizontal direction.

To apply equation (2.30) correctly it is crucial that the droplets are monodisperse so that they can be considered having the same volume. The polydispersity index (PDI) gives an indication about size uniformity and is defined as

$$PDI = \frac{\sigma_V}{\bar{V}} \quad (5.1)$$

where σ_V is the standard deviation of the volume distribution and \bar{V} is the average droplet volume in each run. In each experiment, about 400 droplets were analysed and the PDI was below 5%; so I assumed that the droplets could be regarded as monodisperse (Castro-Hernández et al., 2011). The microscope used for the crystal count was set up in a laboratory where the temperature was about 23 °C. As this temperature was equal to the one chosen for the *growth stage* and the time needed for the crystal count was much shorter than the set *nucleation time*, it was assumed that no nucleation or dissolution

occurred while counting the number of droplets containing PABA crystals. This was verified by counting again the percentage of droplets containing crystals after leaving the PTFE tube containing the droplets in the room for several hours without any temperature control. As the percentage stayed the same, confirming that the outcome of the experiment was not affected by the experimental procedure.

A very similar procedure was used for the experiments in *flowing conditions* (moving droplets). After the droplet array had been generated in the Perspex box at $T_1 > T_{sat}$, the PTFE tube was connected to a glass syringe containing only DI water, the syringe was placed in the syringe pump, while the tube was immersed into the water bath at T_n . Immediately after placing the tube into the water bath, the syringe pump was activated (the flow rate was set at 100 $\mu\text{l}/\text{min}$ for all the experiments) and the droplets started moving inside the tube. After the nucleation time had elapsed, the pump was stopped and both ends of the tube were immediately sealed; and the droplet array was moved into the growth section, where it was left for a time equal to t_{GE} . Finally the tube was removed from the water bath and I observed the droplets under the microscope as described above for the *stagnant conditions* experiments and the experimental probability $P_E(t_i, V, S)$ was calculated. Each experiment was repeated three times to ensure reproducibility and the mean values and standard deviations were calculated. Table 5.1 summarises the experimental conditions used for the experiments in quiescent and flowing conditions performed in this chapter.

Table 5.1 Summary of the experimental parameters for the *stagnant* and *flowing* conditions experiments in the capillary crystalliser.

	Quiescent droplets	Flowing droplets
T_n	3.0, 4.0, 5.0 °C	3.0, 5.0, 8.3 °C
T_g	23 °C	23 °C
t_n	22 – 169 h	3 – 23 min
t_{GE}	0 – 888 h	0 – 888 h
S	2.29, 2.37, 2.47	2.02, 2.29, 2.47
Average volume	4 μl	4 μl
Droplets velocity	0	2.12 mm/s

5.3 Results

5.3.1 Nucleation rate under stagnant conditions

Figure 5.8 shows the experimental probability, $P_E(t_i, V, S)$, obtained experimentally versus the *nucleation time* at different supersaturation ratios (2.29, 2.37, 2.47) in *stagnant conditions* (static droplets). An attempt was also made to collect data for $S = 2.02$, however the repeatability of these experiments was very poor, so data regarding this supersaturation have not been reported. As expected, with the increase of supersaturation the induction time needed to reach a certain probability, $P_E(t_i, V, S)$, decreases. Figure 5.8 D summarises the results obtained in term of nucleation rate. In particular, we found that the nucleation rate increases with the increase of the supersaturation ratio.

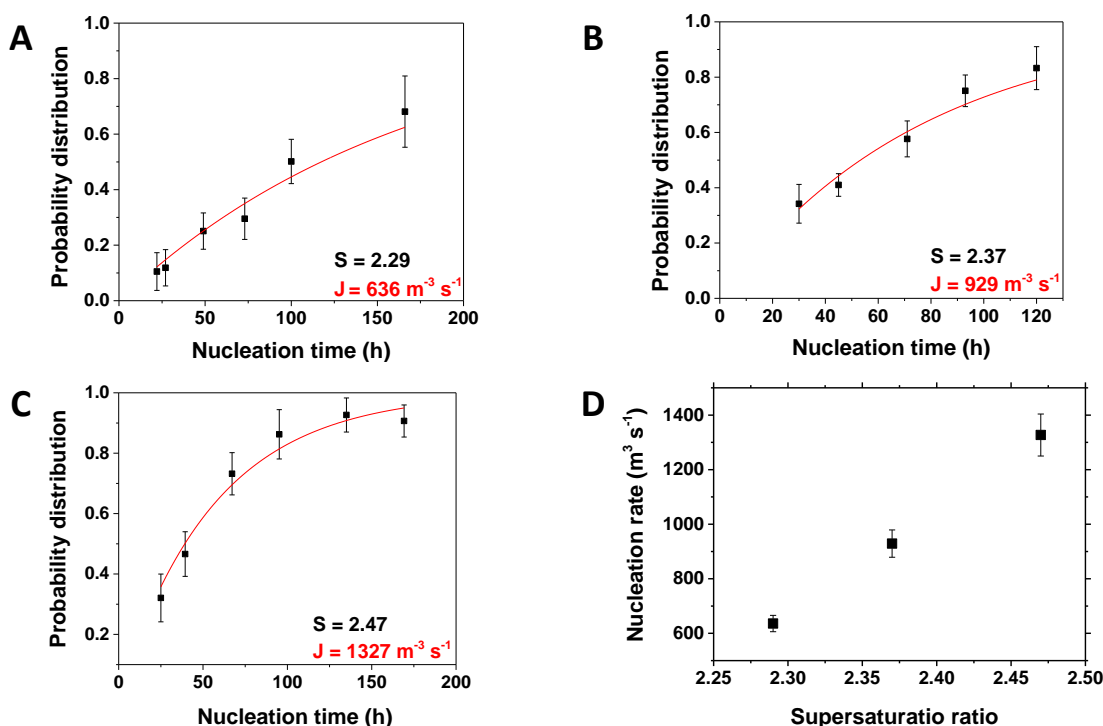


Figure 5.8 Experimental probability $P_E(t_i, V, S)$ versus nucleation time t_n of α -PABA in *stagnant conditions* at different supersaturation ratios: 2.29 (A), 2.37 (B), 2.47 (C); (D) nucleation rate J determined by fitting the experimental data with equation (2.30).

The linearized nucleation rate equation (2.37), reported in section 2.1.5, allowed the kinetic and thermodynamic parameters of nucleation A and B to be estimated from the slope and intercept of the line of best fit (Figure 5.9) for the experimental data obtained

here. As reported in the literature, in case of homogeneous nucleation the expected value for the kinetic parameter A is about $10^{26} - 10^{30} \text{ m}^{-3} \text{ s}^{-1}$ based on Classical Nucleation Theory (Laval et al., 2007). Despite taking the greatest care not to contaminate the solution during the preliminary steps of the experimental procedure (solution preparation, filling of the syringes etc.) and by using online filters (filter size $2 \mu\text{m}$), we expect that a large amount of foreign particles is still expected to be present in the crystallising droplets (Nanev et al., 2011). If this is the case, it is most likely that what was measured is the heterogeneous nucleation rate. This hypothesis is supported by the value found for the kinetic parameter, A , which is in the order of 10^4 , much lower than the value expected for homogeneous nucleation.

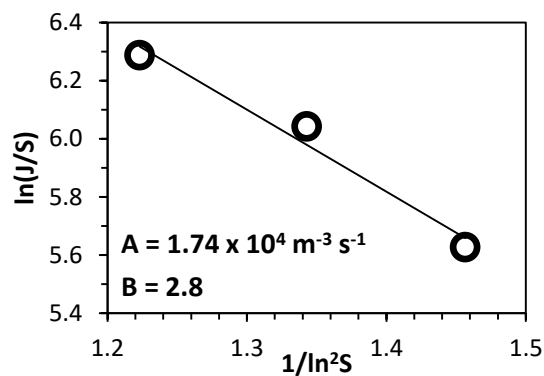


Figure 5.9 Fitting of nucleation rate equation $J(S) = A S \exp[-B/(\ln S)^2]$ (2.23) relative to the experimental data obtained from the capillary crystalliser in *stagnant conditions*, $R^2 = 0.97$.

From A and B I calculated the critical nucleus size, n^* , the nucleation work, W , the Zeldovich factor, the attachment frequency, f^* , and the interfacial energy, γ_{eff} based on the Classical Nucleation Theory (equations (2.38)-(2.42)). Results from these calculations are reported in Table 5.2. It can be noted that as supersaturation increases the critical nucleus size, and the normalized nucleation work barrier $W/k_B T$ decreases. This is an expected result as supersaturation is the driving force of nucleation, so at higher supersaturations it is easier to form stable nuclei. The Zeldovich factor is in the typical range (0.01 – 1) reported by Kashchiev (2000). In case of heterogeneous nucleation, c_0 , contained in the group $f^* c_0$, represents the concentration of possible nucleation sites; this value is related to the concentration and the nature of impurities in the solution and it is impossible to determine.

The consequence is that the real value of c_0 is unknown. However, it is reasonable to assume that it stays constant when the experiments are performed in the same laboratory following the same experimental procedure. If this is the case, then the increase of f^*c_0 with supersaturation, corresponds to an increase of the attachment frequency, f^* .

Table 5.2 Nucleation rate parameters derived from the Classical Nucleation Theory (equations (2.38)-(2.42))under stagnant conditions.

T [°C]	S	n^*	$W/k_B T$	z	f^*c_0 [m ⁻³ s ⁻¹]	γ eff
5	2.29	9.9	4.1	0.067	598870	1.6E-07
4	2.37	8.8	3.8	0.072	571444	1.5E-07
3	2.47	7.6	3.4	0.079	542359	1.5E-07

5.3.2 Nucleation rate under flow conditions

Figure 5.10 shows the experimental probability, $P_E(t_i, V, S)$, obtained versus the induction time under *flowing conditions* (moving droplets) at different supersaturations: 2.02, 2.29, 2.47. As in the previous case (*stagnant conditions* experiments), the probability of nucleation increases with the increase of induction time, however, the time needed for the probability to reach unity is orders of magnitude lower than the previous case. This result corresponds to a much higher (deterministic) nucleation rate. Indeed, by fitting the experimental results with equation (2.30) we obtain values of the nucleation rate about two orders of magnitude higher than the values obtained in stagnant conditions at similar values of the supersaturation ratio Figure 5.10. This suggests that the flow plays a crucial role in enhancing nucleation. However, the mechanism behind this effect is still unclear in the scientific community. As discussed in section 2.2.7, numerous theories have been proposed to explain the role of fluid dynamics on primary nucleation. One of the most accepted theories suggests that the shear rate may be responsible for enhancement of nucleation rate in agitated systems, as it can increase the aggregation frequency of meso-scale clusters in solution (Liu and Rasmuson, 2013).

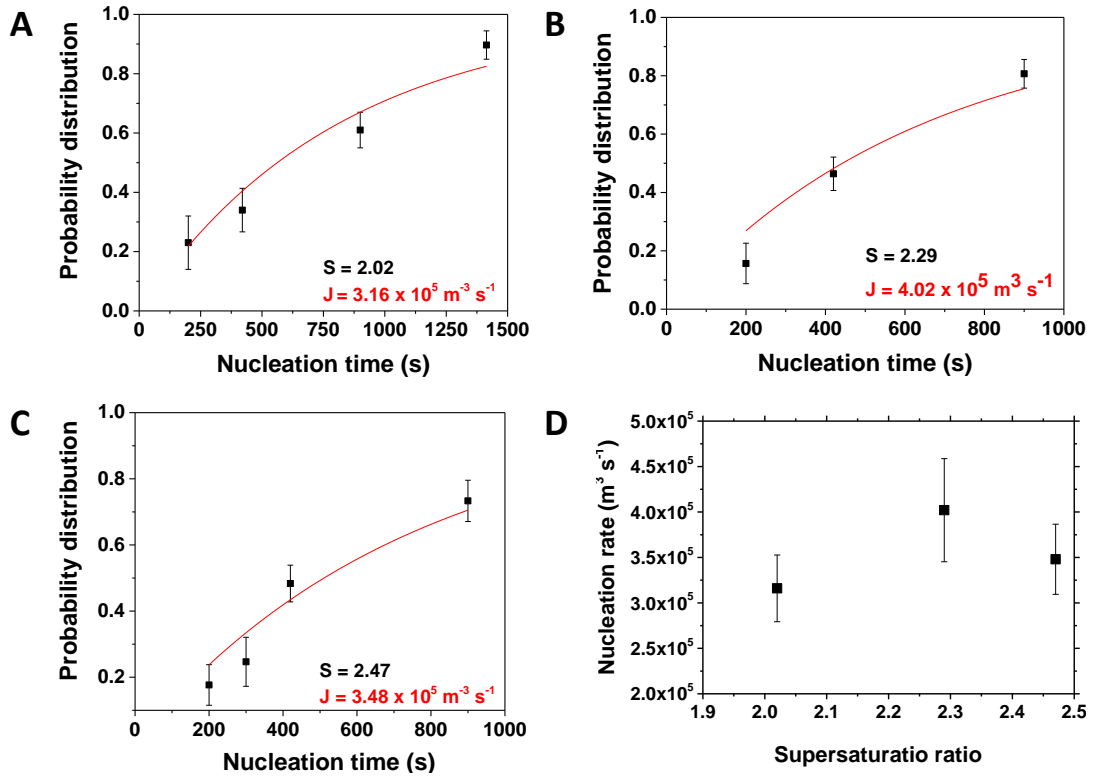


Figure 5.10 Experimental probability $P_E(t, V, S)$ versus the nucleation time of α -PABA in flowing conditions (moving droplets) at different supersaturation ratios 2.02 (A), 2.29 (B), 2.47(C); (D) nucleation rate J determined by fitting the experimental data with equation (2.30).

In single-phase laminar flow the shear rate experienced by these meso-scale clusters would be proportional to the average velocity in the channel:

$$\dot{\gamma} \sim \frac{v_{av}}{R} \tag{5.2}$$

where $\dot{\gamma}$ is the shear rate (1/s), v_{av} is the average velocity inside the channel and R is the channel radius. Flow in micro and milli channels is normally characterised by very low Reynolds numbers (in the order of $10^0 - 10^1$), and so no turbulence is expected to take place in these systems. For the *flowing conditions* experiments presented here, the Reynolds number has unit order of magnitude, and so we can assume that the fluid flow is fully laminar. Because of the segmented flow configuration used in this work, two counter-rotating vortices are generated inside the droplets as qualitatively represented in Figure 5.11. At the centre of the droplets (far from the front and the tail of the droplet) a fully

developed parabolic velocity profile is established with the maximum velocity being twice the average mixture velocity (calculated as the ratio between the flow rate and the channel cross section) (Dore et al., 2012; Kurup & Basu, 2012). Although equation (5.2) does not strictly apply to two-phase segmented flow, in the light of the above considerations, it can be used to estimate the order of magnitude of the shear rate in the flowing droplets. In particular, considering the flow velocity and the channel dimensions used here, we obtain:

$$\dot{\gamma} \sim \frac{v_{av}}{R} = 4.2 \text{ s}^{-1} \quad (5.3)$$

Although this value might seem relatively small, the results obtained suggest that even a gentle shear field plays an important role in enhancing the nucleation rate.

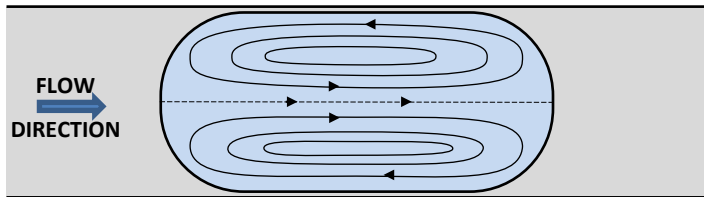


Figure 5.11 Schematic representation of recirculation pattern inside the droplet.

It is also worth noting that our experimental results show that the supersaturation level does not seem to affect the results in the range analysed, because the differences between the nucleation rate values found at different supersaturation ratios are within the experimental error and no clear trend can be identified. For this reason, I consider that, for the present experimental conditions, the value of the nucleation rate is the same within the range analysed, regardless of mixture supersaturation. This is a surprising result and suggests that the effect of shear rate over nucleation overpowers the effect of supersaturation ratio in the range analysed. Unfortunately, as only one value of the nucleation rate was obtained, it is not possible to extract the parameters A and B of the

nucleation rate equation. Consequently, it is not possible to do a comparison of the kinetic and thermodynamic parameters obtained in stagnant conditions.

5.3.3 Stochastic model validation

As discussed in section 2.1.5, nucleation in small volumes has to be treated as a stochastic, volume-dependent process. In particular, the model used in this work to estimate nucleation rate is based on the assumption that the droplet volume is small enough that nucleation occurs following the *Mononuclear Mechanism* (MNM) described in section 2.1.5. In order to check the applicability of this model it must be verified that

$$V \ll \alpha_v^{-0.25} \left(\frac{G}{J} \right)^{\frac{3}{4}} = V_{stoc} \quad (5.4)$$

where V is the average volume of a droplet, α_v is the volume fraction of crystal to the total volume ($\alpha_v = V_m/V$), G is the growth rate of the crystal, J is the nucleation rate and V_{stoc} represents the limit volume that allows the application of the MNM mechanism. Assuming a relatively high growth rate, 1 $\mu\text{m/s}$, a typical value for α_v of 10^{-4} (Kashchiev & Van Rosmalen, 1991), and the largest nucleation rate value found in this work we find that the maximum volume for which the nucleation can be considered to occur via mononuclear mechanism, V_{stoc} , is about 22 mm^3 , which is much larger than the droplets volume in this study. Therefore, the MNM is applicable.

5.3.4 Nucleation rate in stirred vials

Para-amino benzoic acid nucleation in water has also been measured by Sullivan (2015) using a commercial stirred multiple reactor system (Crystal16®). Despite the supersaturation range investigated by Sullivan is slightly different from the one used in our experiments we still believe that a comparison is significant both for the *stagnant* and the *flowing conditions* experiments. The experimental system they used consists of a platform with an integrated heating/cooling system that can hold up to 16 small vials (about 2 ml). The device is also equipped with a turbidity sensor to register the onset of crystallization. Using this apparatus, the *nucleation time* t_n for a 0.8 ml PABA aqueous solution was measured at various supersaturation ratios (1.67, 1.73, 1.8, 2.02). Concentration and

temperature uniformity was ensured by stirring the solution with a magnetic stirrer (1250 rpm). Because the solution volume in each vial is very small, the experimental nucleation rate is also considered to follow a Poisson distribution; therefore, the results were fitted with equation (2.30). For these experiments, the vials containing the solution were kept at 50 °C for 60 minutes to ensure complete dissolution of the crystals; then the temperature was dropped to reach the desired supersaturation and the time corresponding to the onset of crystallization was recorded. This time corresponds to t_n in equation (2.30). Because in this case, unlike the experiments performed in the capillary tube, the nucleation time is recorded from the experiment rather than set a priori, the separation of nucleation and growth stage is not achieved ($t_n \neq t_i$) and the time the crystal nuclei need to reach a detectable size is not distinguishable from the actual nucleation time. As a consequence, t_g in equation (2.30) remains undetermined and was estimated as the shortest induction time measured, for each supersaturation level. Alternatively, t_g could be calculated based on the growth rate kinetics or estimated as a model parameter; however, Xiao et al. (2017) demonstrated that the three methods produce equivalent results in terms of nucleation rate, therefore the authors decided to take t_g as the shortest experimental induction time. Table 5.3 summarises the experimental conditions used in their work, while the detailed experimental procedure and setup can be found in Sullivan (2015).

Table 5.3 Summary of the experimental parameters for the experiments performed by Sullivan (2015) using a commercial stirred multiple reactor system (Crystal16®).

T_n	20 °C
t_n	10 – 60 min
S	1.67, 1.73, 1.8, 1.9, 1.97, 2.02
Volume	0.8 ml
Polymorphic form	α
Stirring speed	1250 rpm

Their results are reported in Figure 5.12 in terms of nucleation rate as function of supersaturation. Even if the superstation ratios investigated in this case are comparable to those used in the capillary flowing experiments, nucleation rate was found to be significantly lower (1 – 2 orders of magnitude) than in the previous case.

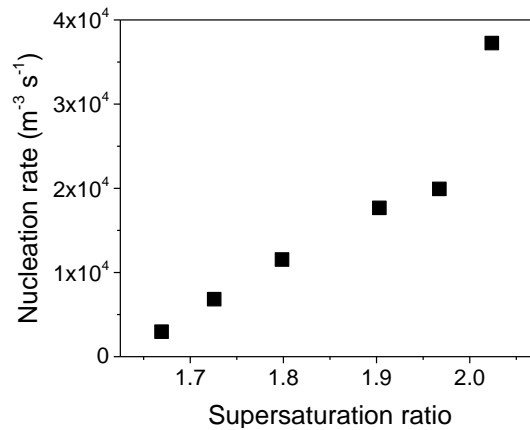


Figure 5.12 Experimental (deterministic) nucleation rates (J) obtained for α -PABA in water versus supersaturation ratio in stirred vials; each experimental point is based on 80 nucleation time measurements; fluid dynamic conditions are the same for all the experiments (adapted from Sullivan, 2015).

This is a surprising result and can be explained by taking into account the influence of fluid dynamic on the nucleation process. However, the fluid dynamic conditions inside the vials are expected to be quite complex and were not assessed by the authors. Therefore, we decided to estimate the shear rate in the vials using a semi-empirical approach. The average shear rate in stirred vessels can be expressed as a function of the specific energy dissipation rate (Pérez et al., 2006)

$$\dot{\gamma}_{av} = \left(\frac{P}{\mu V} \right)^{1/2} \quad (5.5)$$

where μ and V are the fluid viscosity and volume, respectively, and P is the power input (W) which is a function of the power number, the rotational rate of the impeller, the density of the fluid and the diameter of the stirrer according to equation (2.63). Using the correlation proposed by Furukawa et al. (2012) for unbaffled vessels we were able to calculate the power number N_p and, consequently, the power input P . Applying equation (5.5) then we obtain the average shear rate inside the vials: $\dot{\gamma}_{av} \approx 150 \text{ s}^{-1}$. This value is about two orders of magnitude larger than the shear rate in the droplets flowing in the capillary.

Comparison between our results in *stagnant conditions* with what obtained by Sullivan (2015) interestingly shows that nucleation rates achieved in the stirred vials are one order

of magnitude higher than those obtained in our capillary crystalliser (*stagnant conditions*) even for lower supersaturation ratio (Figure 5.8 D and Figure 5.12). I used the nucleation data they obtained to calculate the kinetic and thermodynamic parameters of nucleation A and B from the slope and intercept of the line of best fit shown in Figure 5.13. From A and B, we were then able to calculate the characteristic parameters of the nucleation process according to the Classical Nucleation Theory (equations (2.38)-(2.42)); the results of calculations are shown in Table 5.4.

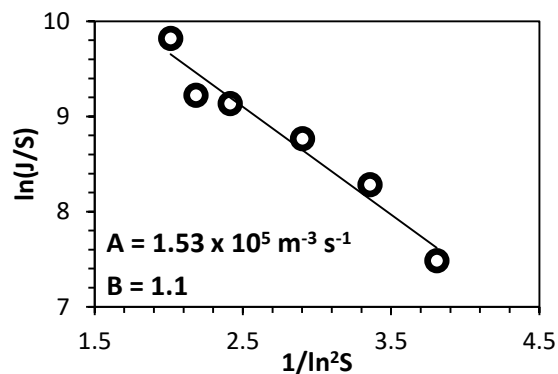


Figure 5.13 Fitting of nucleation rate equation $J(S) = A S \exp[-B/(\ln S)^2]$ (2.23) relative to the experimental data obtained from the capillary crystalliser in *stagnant conditions*, R^2 of fitting = 0.96.

If compared with the values of A and B relative to our microfluidic crystalliser (*stagnant conditions*), I can notice that the values for B are in the same order of magnitude, suggesting that fluid dynamic conditions do not have a significant effect on the thermodynamic of the nucleation process. As a consequence, the difference with the parameters n^* , $W/k_B T$, z and y_{eff} (Table 5.4) are relatively small. On the other hand, A appears to be one order of magnitude larger than the value obtained for the *stagnant conditions* experiments performed in this work, indicating that fluid dynamics has a significant effect on the nucleation process. In particular, by comparing the values of the nucleation parameters which are derived from A, it is apparent that the Zeldovich factor z remains approximately constant for the two cases here considered (*stagnant droplets* and *stirred vials*), while a remarkable difference can be observed for the group $f^* c_0$. As previously discussed, the value of c_0 cannot be estimated as it is related to the purity of the solution, therefore the exact value of the attachment frequency f^* remains unknown.

However, it is reasonable to assume that c_0 is in the same order of magnitude for the two cases analysed because all the experiments were performed using laboratory deionised filtered water as solvent. If this is the case, then the increase of combined parameter f^*c_0 has to be attributed to an increase in the attachment frequency f^* due to the different fluid dynamic conditions.

Table 5.4 Nucleation rate parameters derived from the Classical Nucleation Theory (equations (2.38)-(2.42)) based on the experimental nucleation rates of PABA in water at 20 °C obtained by Sullivan (2015).

S	J m⁻³ s⁻¹	n*	W/k_BT	z	f*c₀ [m⁻³ s⁻¹]	γ_{eff}
1.67	2.97 x 10 ³	17	4.3	0.040	6.33 x 10 ⁶	8.75 x 10 ⁻⁸
1.73	6.83 x 10 ³	14	3.8	0.046	5.77 x 10 ⁶	8.75 x 10 ⁻⁸
1.80	1.15 x 10 ⁴	11	3.3	0.053	5.20 x 10 ⁶	8.75 x 10 ⁻⁸
1.90	1.77 x 10 ⁴	8	2.7	0.063	4.58 x 10 ⁶	8.75 x 10 ⁻⁸
1.97	1.99 x 10 ⁴	7	2.5	0.070	4.28 x 10 ⁶	8.75 x 10 ⁻⁸
2.02	3.72 x 10 ⁴	6	2.3	0.076	4.05 x 10 ⁶	8.75 x 10 ⁻⁸

5.4 Discussion

The experimental results relative to the nucleation rate of α -PABA obtained both in the capillary system and in the stirred vials setup for selected values of the supersaturation ratio are summarised in Figure 5.14. These specific nucleation rate values have been chosen with the intent of comparing the performance of the different systems presented here. Although the nucleation rate relative to the stagnant conditions refers to a slightly higher supersaturation ratio I believe that the discussion does not lose generality as the focus is on the order of magnitude. The nucleation rate is lowest under stagnant conditions in our capillary system, while it is highest in the flowing conditions experiments conducted at relatively low shear rate. The large difference (about two orders of magnitude) between the nucleation rates values found in these two conditions is even more significant considering that the stagnant conditions nucleation rate refers to slightly higher supersaturation values. These findings confirm that fluid dynamics play a fundamental role in the nucleation process and lowers the time required for the formation of the first crystal

in the supersaturated solution. Because the experimental method measures primary nucleation rates, this effect cannot be attributed to the enhancement of secondary nucleation. On the basis of previous studies, it can be argued that the reduction of induction time is due to the enhancement of meso-scale clusters rate of collision promoted by the motion of the fluid. However, this cannot be confirmed without further experimentation that might unveil the presence of large meso-scale clusters in the supersaturated solution, which is at the base of the two-step nucleation theory.

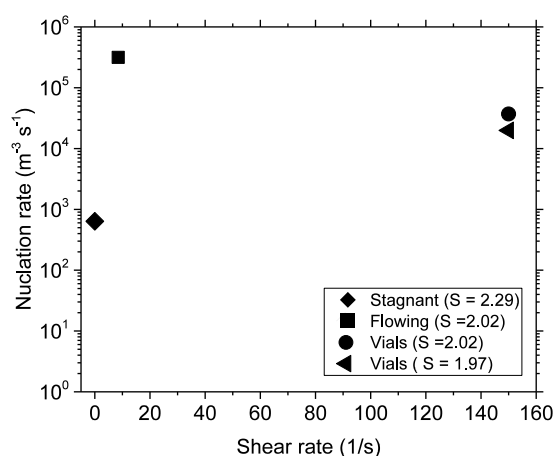


Figure 5.14 Nucleation rate of α -PABA estimated from the best fit of equation (2.30) vs average shear rate; the reported values refer to the microfluidic experimental setup in stagnant conditions (S = 2.29), flowing conditions (S = 2.02) and stirred vials (S = 1.97, 2.02).

For the stirred vials experiments, although the average shear rate is about two orders of magnitude larger than in the flowing conditions experiments, the nucleation rate found is about one order of magnitude lower. This result is unexpected and may be explained considering the effect of agitation on nucleation. There is evidence that fluid shear may increase nucleation by reducing the metastable zone width; however, there is also evidence that too vigorous agitation may hinder nucleation (Liu & Rasmuson, 2013; Miyasaka et al., 2006; Mullin & Raven, 1962). In this regard, Liu and Rasmuson (2013) measured the induction time of butyl-paraben crystallization in ethanol using small vials (20 ml) equipped with a magnetic stir bar and found that increasing agitation was effective in reducing the induction time only when the stirring rate was below 200 rpm, while more vigorous stirring resulted in a significant increase of the induction time. These results seem to be consistent

with the shear-enhanced aggregation theory; in fact it is reported that the probability of particle collision increases linearly with the shear rate only at low shear rates, but it decreases to zero at high shear rates (Hollander et al., 2003). In addition, the flow dynamics in the stirred vials is highly non-uniform and the shear rate near the stirrer bar tip can be orders of magnitude higher than the average value causing the disruption of the aggregation process. Therefore, it is reasonable to assume that agitation might have hindered the coalescence of meso-scale clusters present in the solution leading to a lower nucleation rate. If this is the case, using a gentler stirring may actually lead to a higher nucleation rate, similar to the one measured for the droplets flowing in the capillary tube.

5.5 Conclusion

I estimated the primary nucleation kinetics of para amino-benzoic acid in water in different fluid dynamic conditions using a capillary droplet based crystalliser. Due to the small dimension of the droplets, I treated nucleation as a stochastic process that can be described by a Poisson distribution. In order to expand the depth and the breadth of the analysis, I compared these results with those obtained by Sullivan (2015) using a commercial stirred multiple reactor system (Crystal16®) at similar supersaturation ratios. The results obtained for stagnant droplet experiments and the multiple reactor system were fitted to the nucleation rate equation and the kinetic and thermodynamic parameters A and B were determined from the slope and the intercept of the line of best fit. On the basis of the Classical Nucleation Theory, the characteristic nucleation parameters were calculated: critical nucleus size, nucleation work, Zeldovich factor, attachment frequency and interfacial energy. From practical considerations and the values obtained for the kinetic parameter A, it was assumed that nucleation proceeds through a heterogeneous mechanism. Comparison between the results relative to the stirred vials and the stagnant droplet experiments demonstrated that fluid dynamic conditions do not affect the thermodynamic (B is within one order of magnitude for the two systems), but have a significant effect of the kinetics of the process (A is found to be one order of magnitude larger for the case of the stirred vials even for lower supersaturation ratios). A careful analysis of the nucleation parameters shows that the larger value of the parameter A found

in case of the stirred vials experiments might be attributed to an enhancement of the attachment frequency f^* . The considerable effect of fluid dynamics on nucleation was confirmed by my results relative to the flowing droplets. In fact, it was observed that by forcing the droplets to move in the capillary tube at constant velocity the nucleation rate increases by two orders of magnitude relative to the rate obtained in stagnant conditions (static droplets). These results have been attributed to the effect of shear rate, which can increase the probability of collision of meso-scale clusters in solution leading to an increase in the rate of crystal formation. In addition, in *flow conditions*, I observed that the supersaturation ratio does not affect the nucleation rate value, suggesting that the effect of the flow overcomes the effect of supersaturation in the range analysed. This confirms the strong effect of shear over the nucleation process. Finally, Comparison between our experimental results and those obtained by Sullivan (2015) show that although the shear rate achieved in the stirred vials is orders of magnitude larger than the characteristic shear rate in the flowing droplets, the nucleation rates I measured in the capillary system under *flow conditions* are higher than those obtained in the vials. These findings support the idea that nucleation is most likely to proceed according to the shear-enhanced aggregation theory, as shear enhances the probability of collision, and consequently of aggregation, of meso-scale clusters in the supersaturated solution; however, the results also demonstrate that increasing the shear rate beyond a certain level is not beneficial, as it results into a disruption of the nucleation process due to particles attrition. This could be verified by performing additional experiments using the droplets system and varying the droplet velocity in order to vary the shear rate. In this way, it might be possible to find an optimal value of the shear rate that would allow to maximise the nucleation rate.

Chapter 6

CRYSTAL NUCLEATION ON A GAS-LIQUID INTERFACE

6.1 Introduction

In the scientific literature it is suggested that a gas bubble in a supersaturated solution can provide a surface to trigger heterogeneous nucleation acting in practice as a foreign particle in the solution (Hem, 1967; Wohlgemuth et al., 2009). However, no direct evidence was provided to support this hypothesis. In Chapter 4 of this thesis, we observed that the presence of gas bubbles moving in a supersaturated solution can significantly reduce the metastable zone width in cooling crystallization experiments. However, it is unclear if this effect is related to the particular fluid dynamic conditions attained when a gaseous phase is dispersed in a liquid or to a decreased nucleation energy barrier due to the presence of gas bubbles acting as an additional nucleation centre. In this chapter, I want to investigate if the gas-liquid interface can act as nucleation centre for heterogeneous nucleation of small molecules in solution in stagnant condition with the aim of isolating the effect of fluid dynamic from the bubble presence. To do so, I employed a custom made experimental setup that allows direct observation of crystal formation at three different location: i) the liquid bulk, ii) the gas-liquid interface and iii) the liquid-solid interface, by mean of a standard optical microscope. The aim is to clarify the role of the gas-liquid interface in cooling crystallization and to provide evidence of nucleation on the gas-liquid interface by direct observation.

6.2 Experimental section

6.2.1 Experimental setup and procedure

The experimental setup used in this chapter consists of a square glass transparent capillary (1 mm internal diameter) which contains the crystallizing solution. For the present investigation, adipic acid (AA) in water was used as model compound instead of PABA in order to reduce the time required for the experiment. It is in fact reported that the characteristic induction time for primary nucleation of adipic acid in water is in the order of minutes for a solution volume of 1.5 mm³ (Rossi et al., 2015), while for PABA it is expected to be orders of magnitude larger on the base of the results obtained in Chapter 5. In order to control the supersaturation, the glass capillary was fixed within a Perspex enclosure (as

shown in Figure 6.1) connected to two water baths; the thermostatic water baths (Huber MPC-K6, programmable) were used to control the temperature of the solution inside the glass capillary and thereby to apply the *double pulse* temperature profile technique introduced in section 2.1.5. The Perspex box where the square glass capillary was fitted was placed on an optical inverted microscope stage (Olympus IX50) that allowed to detect the presence of crystals inside the capillary by visual observation.

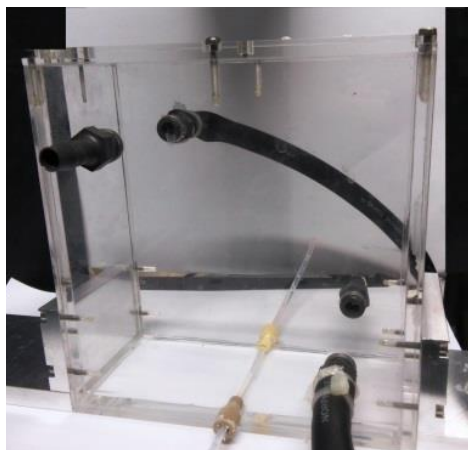


Figure 6.1 Experimental setup: Perspex box and square glass capillary fitted at the bottom.

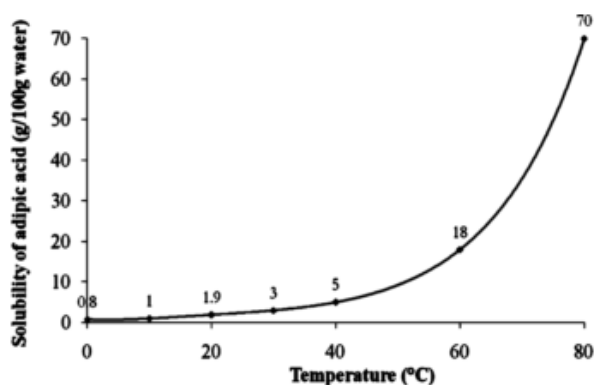


Figure 6.2 Solubility of adipic acid in water as function of the temperature (Rossi et al., 2015).

The solution was prepared by dissolving 2.1 g of adipic acid ($(\text{CH}_2)_4(\text{COOH})_2$, >99.5% pure, Sigma-Aldrich) in 100 ml of filtered (0.2 μm) deionised water (conductivity <0.2 $\mu\text{S}/\text{cm}$). Adipic acid solubility is displayed in Figure 6.2 where the solubility curve was derived by fitting the experimental data available in the literature (Mullin, 2001). The solution was

kept above the saturation temperature (30 °C) for several hours to allow the complete dissolution of the crystalline material. Then, a few millilitres of solution were withdrawn using a clean pre-heated (30 °C) glass syringe and pushed inside the empty glass channel through a 0.2 µm filter. A small air pocket was left at the end of the glass channel in order to create a gas-liquid interface. After that, the temperature of the solution was dropped to the desired *nucleation temperature* T_n by circulating water from a thermostatic bath within the Perspex enclosure for a set time t_n (*nucleation time*) to allow nucleation. After the set nucleation time was elapsed, the first thermostatic bath was stopped and water at T_g (*growth temperature*) from a second thermostatic bath was circulated through the Perspex enclosure for an additional time t_{GE} (experimental growth time) to allow the nuclei formed to grow into a detectable size. The temperature T_g was chosen in such a way that the solution is within the metastable zone, so that no further nucleation or dissolution can happen but only growth of the already formed nuclei. The experimental procedure described allows the separation of the nucleation and growth stages according to the *double pulse technique* briefly described in section 2.1.5; the corresponding supersaturation profile applied is shown in Figure 6.3. The experimental growth time t_{GE} is set to be 3 h as suggested by Rossi et al. (2015) to allow the nuclei formed during the nucleation stage to grow to a macroscopic size. To identify a suitable temperature for the growth stage (T_g) we performed a preliminary experiment where we kept the adipic acid solution (at the same concentration used for the experiments: 2.1 g_{AA}/100 ml_{H2O}) inside our experimental system at T_g and verifying that no crystals were present after a time equal to t_{GE} . While to verify that the crystals formed would not dissolve at T_g , we counted the number of crystals inside the glass channel multiple times during the growth stage. As the number of crystals stayed constant, we confirmed that the selected value of T_g is within the MZW for the experimental conditions used here.

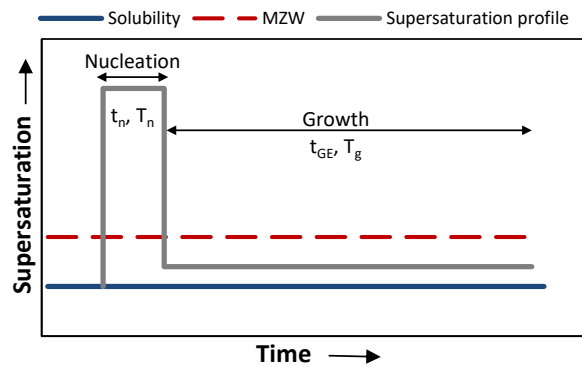


Figure 6.3 Experimental supersaturation profile used (gray line), metastable zone width (dashed red line) and solubility limit (blue line).

After the set growth time t_{GE} elapsed, we counted the number of crystals born at three different locations: the liquid bulk, ii) the gas-liquid interface and iii) the liquid-solid interface. A schematic of the glass capillary and the three different nucleation locations considered for nucleation is depicted in Figure 6.4. The crystals were visualised by means of an optical microscope which allows to focus on different planes inside the square channel (focus depth of the microscope is about $20\ \mu\text{m}$, channel depth was $1000\ \mu\text{m}$). In this way we were able to distinguish between crystals growing on the glass walls and in the bulk of the solution. In this respect, the choice of a square channel instead of a circular one was essential to easily determine the position of the glass walls and therefore distinguish between the crystals located in the bulk of the solution and on the glass surface. Table 6.1 summarise the experimental conditions used in this chapter.

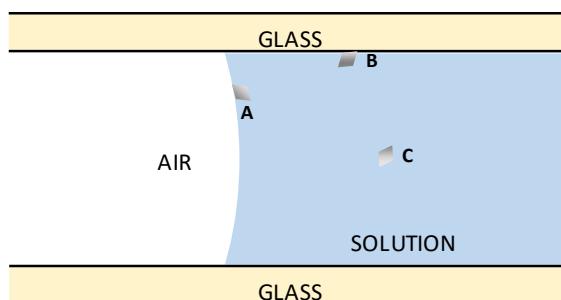


Figure 6.4 Schematic of the glass capillary used for the experiments; the air pocket forms a meniscus separating the gas and the liquid solution; the three locations considered for nucleation are depicted as A (gas-liquid interface), B (glass surface) and C (bulk of solution).

Table 6.1 Summary of the experimental condition used.

Nucleation stage temperature T_n	8.8, 9.5, 10, 11, 12 °C
Growth stage temperature T_g	22 °C
Nucleation time t_n	30 – 1080 s
Experimental growth time t_{GE}	3 h
Supersaturation S	1.8, 1.94, 2.09, 2.18, 2.3

6.2.2 COMSOL simulation of temperature profile

The temperature profile inside the square channel during the cooling process was determined by using COMSOL Multiphysics 5.0 (Heat Transfer Module) and it is shown in Figure 6.5. The simulation refers to the worst case scenario in which the solution has to be cooled from 30 °C (that is the temperature at which the solution is kept before the start of the experiment to avoid undesired formation of crystals) to the lowest nucleation temperature used in this work (8.8 °C).

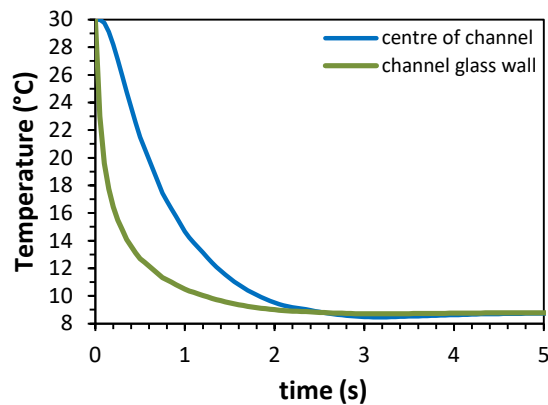


Figure 6.5 Temperature profile versus time at the centre of the glass channel (blue line) and the glass internal surface (green line); at $t=0$ temperature at the glass external surface is dropped from 30 °C to 8.8 °C.

The plot (Figure 6.5) displays both the temperature at the centre of the glass channel and at the glass internal surface. The results from the simulation show that the temperature becomes uniform and reaches its final value (within $\pm 5\%$ of the final nominal value) after less than 3 s from the start of the cooling process. Because the time needed to reach a constant uniform temperature is much shorter than the time allowed for nucleation (minimum nucleation time used for these experiments is 30 s), then we can assume that no

crystals were formed during this period and therefore the results are not influenced by the specific experimental procedure used.

6.3 Results and discussion

Some preliminary nucleation experiments were performed at a supersaturation ratios $S = 1.8$ and 1.94 , that correspond to nucleation temperatures of 12 and 11 °C, respectively. At this levels of supersaturation no crystals were formed for $t_n < t_{GE}$. For $S > 1.94$ ($T_n < 11$ °C), we were able to measure the number of nuclei formed in a certain time on the different surfaces (bulk of the solution, glass surface and gas-liquid interface) and the results are reported in Figure 6.5.

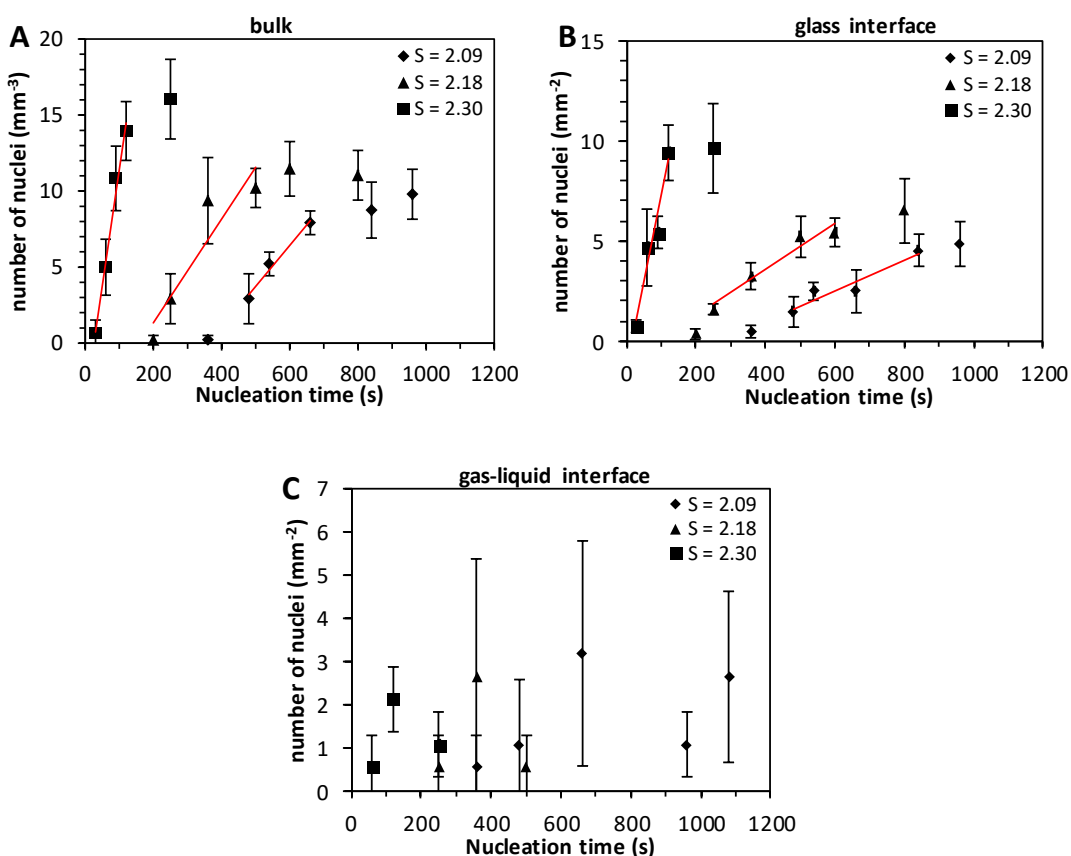


Figure 6.6 Number of nuclei counted in the bulk of solution (A), glass surface (B) and gas-liquid interface (C) versus the nucleation time for different supersaturation; solid red lines represent the best linear fit for a selected subrange of data ($R^2 = 0.98, 0.86, 0.99$ for $S = 2.09, 2.18, 2.30$ respectively for the bulk of solution, graph A) ($R^2 = 0.86, 0.95, 0.94$ for $S = 2.09, 2.18, 2.30$ respectively for the glass surface, graph B); the slope of the fitting curves represents the stationary nucleation rate; standard deviations are reported as error bars.

Although our results demonstrate that nucleation on a gas-liquid interface is possible (Figure 6.6 C), unfortunately data relative to the nucleation on this substrate were too scattered to perform a quantitative analysis. The high level of uncertainty relative to these data might be due to the fact that, although the gas-liquid interface provides sites for heterogeneous nucleation, crystals do not stick to this support strongly enough so they end up in the bulk of the solution or at the bottom of the channel. In addition, it should be considered that the temperature changes throughout the experiment cause the volume of the air bubble inside the channel to increase and decrease; this causes unpredictable changes in the gas-liquid interface position and shape, thereby making it difficult to distinguish between crystals born on the gas-liquid interface and those born in the bulk. Considering that the length of the gas bubble is approximately 5 mm, we estimated that the volume change caused by the temperature increase from T_n to T_g is about 3-4%, which correspond to the gas-liquid interface moving of approximately 20 μm . Due to the small dimensions of the crystals this could cause some uncertainty in the determination of the original position of the nuclei. In the case of nucleation in the bulk of the solution and on the glass surface, a certain level of uncertainty is still observed. If we consider the limitations of the experimental system, this uncertainty is perhaps inherent and could be attributed to the difficulties in identifying the exact position where the crystals were born. It might be possible in fact that crystals born in proximity of the glass surface will grow until they touch the glass surface, thereby reducing the number density of nuclei measured in the bulk. On the other hand, crystals born in the bulk might not stick to the glass support strongly enough and end up in the bulk of the solution thereby increasing the apparent number density of the nuclei in bulk. Despite the relatively large uncertainty observed, it is still possible to clearly identify a trend in the experimental data. In particular, the data reported in Figure 6.6 A and B show a clear increase in the number of nuclei formed as the time allowed for nucleation is increased. However, the number of the nuclei reaches a plateau after a certain time, indicating significant supersaturation depletion due to nucleation. Figure 6.7 shows Adipic acid crystals observed in different positions inside the glass capillaries.

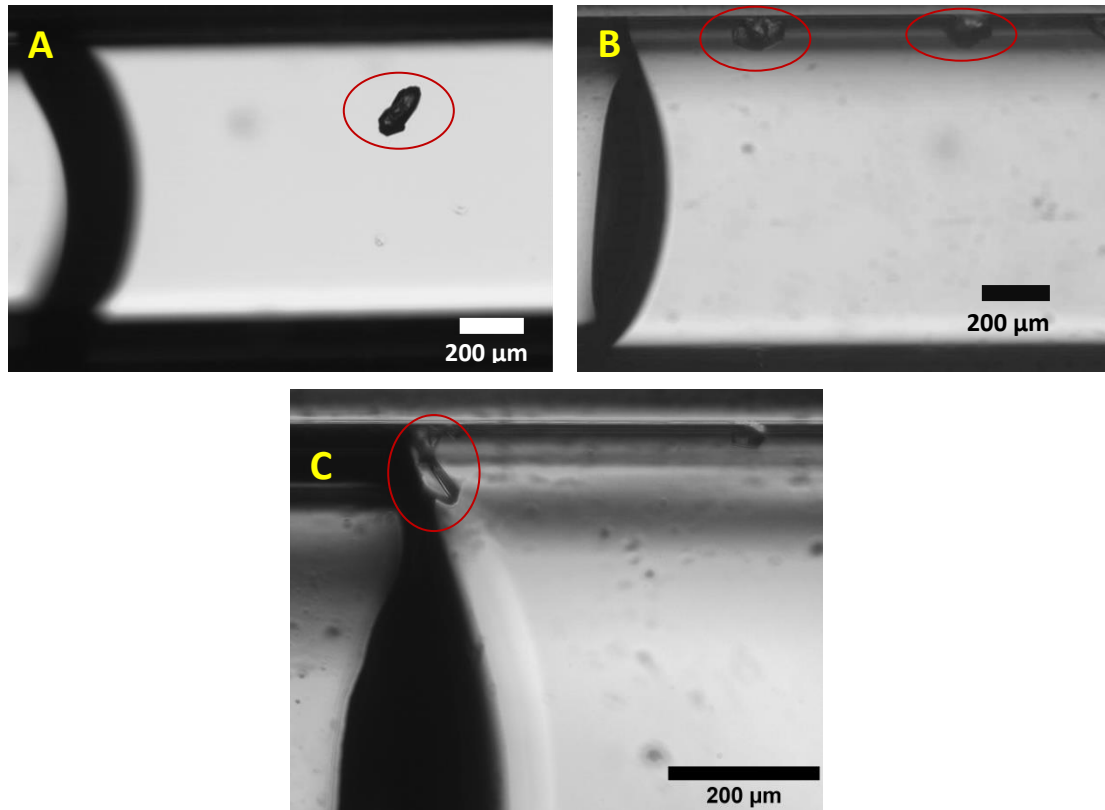


Figure 6.7 Microscope images of adipic acid crystals in the glass channel at the three locations considered bulk of the solution (A), glass surface (B) and gas-liquid interface (C) as schematically shown in Figure 6.4; the gas-liquid interface is visible on the left-hand side of each image as a dark curved fringe.

The results relative to nucleation in the bulk and on the glass surface cannot be directly compared because the former is expressed as number of nuclei per mm^3 of solution, while the latter is expressed as number of nuclei per mm^2 of glass surface. However, assuming that in both cases (nucleation in the bulk and on the glass surface), the nucleation rate is time independent it is possible to extrapolate the nucleation rate for each supersaturation from the best linear fitting of the experimental data presented in Figure 6.6 A and B. . The slope of the line of best fit would then represent the stationary nucleation rate $J(S)$ for a given supersaturation ratio. For the experimental data presented in Figure 6.6 A and B, the number of nuclei formed exhibits a linear dependence on the nucleation time only for low values of the nucleation time, while the plateau observed for long nucleation times is due to the supersaturation depletion, due to crystal formation and growth, becoming so large that nucleation is no longer time-independent. Therefore, only a subrange of the

experimental data was used here for the nucleation rate estimation; the corresponding best linear fit is represented by the red line in Figure 6.6 A and B.

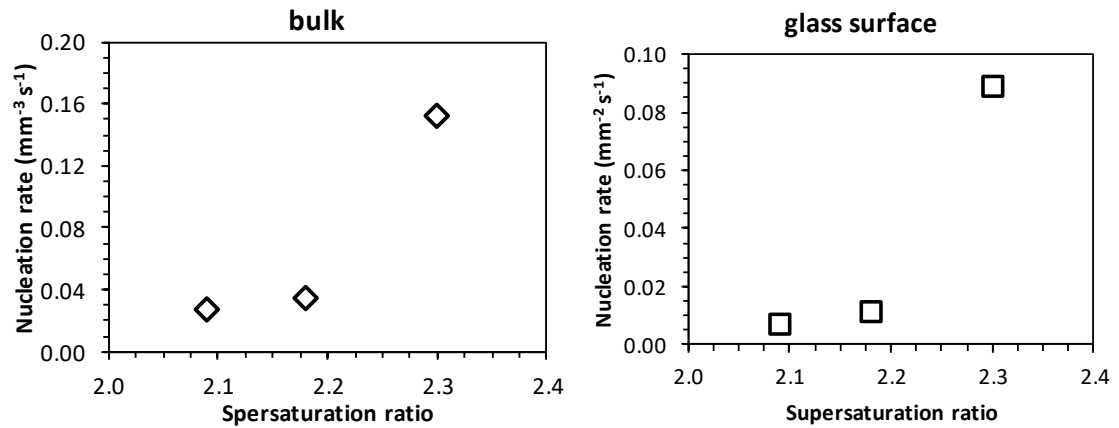


Figure 6.8 Nucleation rate versus supersaturation ratio calculated as the slope of the best linear fit shown in Figure 6.6 relative to the bulk of the solution and the glass surface.

By plotting $\ln(J/S)$ versus $\ln^2 S$ we can calculate the kinetic and thermodynamic parameters A and B according to equation (2.36) as the slope and the intercept of the line of best fit (Figure 6.9).

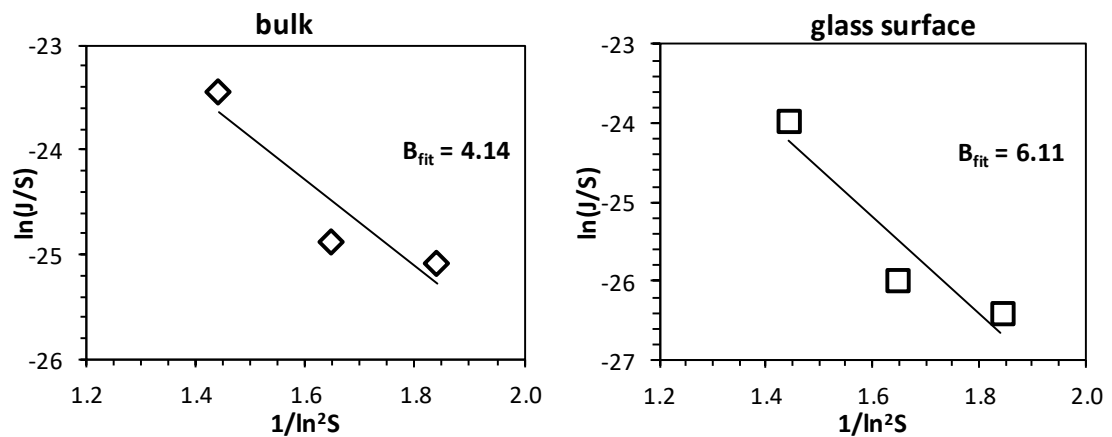


Figure 6.9 Fitting of nucleation rate equation $J(S) = A S \exp[-B/(\ln S)^2]$ (equation (2.36)) ($R^2 = 0.76, 0.89$ for the bulk of the solution and the glass surface respectively).

The parameter B in particular can be used to calculate the size of the critical nucleus n^* , the (normalised) work barrier $W/k_B T$ and the Zeldovich factor z according to the Classical

Nucleation Theory (equations (2.38), (2.39), (2.40), (2.42) and (2.43)). The results of the calculations, presented in Table 6.2, show that the three parameters n^* , $W/k_B T$ and z are in the expected range suggested by (Kashchiev, 2000). In particular, as the supersaturation ratio is increased the critical nucleus size and the nucleation energy barrier (represented by the parameter $W/k_B T$) decrease as expected, so nucleation becomes more thermodynamically favourable. Table 6.3 reports the interfacial energy calculated on the basis of the experimental results obtained γ_{eff} for both cases (nucleation in the bulk and on the glass surface) and the interfacial energy we would expect in case of homogeneous nucleation γ . As discussed in section 2.1.1, the value of the ratio $\gamma_{\text{eff}}/\gamma$, calculated for nucleation in the bulk, is related to the relative magnitude of homogeneous and heterogeneous nucleation rate and it is found to be below unity.

Table 6.2 Nucleation rate equation parameters relative to nucleation in the bulk on the solution and on the glass surface.

T [°C]	S	J(S) (mm ⁻³ s ⁻¹) (mm ⁻² s ⁻¹)		n*		W/k _B T		z	
		bulk	glass	bulk	glass	bulk	glass	bulk	glass
10	2.09	0.027	0.007	21	31	8	11	0.0435	0.0358
9.5	2.18	0.028	0.011	17	26	7	10	0.0486	0.0400
8.8	2.30	0.153	0.089	14	21	6	9	0.0556	0.0457

Table 6.3 Interfacial energy for heterogeneous (γ_{eff}) and homogeneous (γ) nucleation, based on equations (2.42) and (2.45)

T [°C]	S	γ_{eff} (mJ m ⁻²)		γ (mJ m ⁻²)	$\gamma_{\text{eff}}/\gamma$
		bulk	glass		
10	2.09	7.75	8.83	4.58	0.169
9.5	2.18	7.74	8.81	4.60	0.168
8.8	2.30	7.72	8.79	4.61	0.167

The results obtained show that the normalised energy barrier ($W^*/k_B T$) is lower in the case of nucleation in the bulk of the solution than in the case of nucleation on the glass surface

suggesting that nucleation is thermodynamically more favourable in the bulk of the solution rather than on the glass surface. This result might seem surprising if one assumes that homogeneous nucleation is the dominant nucleation mechanism taking place in the bulk of the solution. In fact, it is well known that the energy barrier that has to be overcome for heterogeneous nucleation to happen is inherently lower than the one relative to homogeneous nucleation, so nucleation is expected to be more thermodynamically favourable on the glass surface. However, it should be considered that, despite the greatest care has been taken to avoid contamination of the solution by foreign particles (filtered deionised water has been used for all the experiments), it is impossible to remove all solid bodies from a solution or a solvent (Mersmann, 2001). For this reason, homogeneous nucleation in the bulk of the solution is highly improbable. This is confirmed by the value of the ratio $\gamma_{\text{eff}}/\gamma$ (shown in Table 6.3) that is well below the unity, showing that even in the bulk of the solution nucleation happens according a heterogeneous mechanism. If I compare my results with those obtained by other authors in similar experimental conditions ($S = 1.23 - 2.10$, stagnant droplets of adipic acid solution), my values of n^* and $W/k_B T$ relative to the nucleation in the bulk of the solution are slightly higher than the ones previously reported in the literature (Rossi et al., 2015). As discussed above, this result might be explained by considering that the number density of nuclei born in the bulk of the solution might have been overestimated by including crystals that were actually born on the glass support. If this is the case, I would expect a reversed situation in which the glass surface appears as a more active support for nucleation with respect to the bulk of the solution, while the nucleation work and the critical nucleus size ($W/k_B T$ and n^*) relative to the bulk of the solution will be more similar to that reported in the literature (Rossi et al., 2015).

6.4 Conclusion and future recommendations

In this chapter we aimed to study the activity of different nucleation sites (glass surface, bulk of the solution and gas-liquid interface) relative to the nucleation rate of adipic acid in water. For this investigation I created an air pocket in a glass capillary containing adipic acid aqueous solution and we measured the number density of crystals over time at three

relevant locations: the glass surface, the bulk of the solution and the gas-liquid interface. The results demonstrate that the gas-liquid interface can act as a site for heterogeneous nucleation confirming what inferred by Wohlgemuth et al. (2009) on the basis of their metastable zone width measurements. However, unfortunately the data obtained were too scattered to perform a quantitative analysis. This scatter was attributed to the difficulties in determining the original position where the crystalline nuclei were born. In fact, the crystals might not stick strongly enough to the gas-liquid interface and therefore ending up in the bulk of the solution. In addition, the shape and position of gas-liquid interface might change due to gas bubble expansion and contraction produced by the temperature changes throughout the experiment, making it difficult to determine if a crystal was formed on the gas-liquid interface or just in its proximity. The data relative to nucleation on the glass surface and the bulk of the solution were analysed and the critical nucleus size, nucleation work and the Zeldovich factor were calculated on the basis of the Classical Nucleation Theory. The results surprisingly show that the energy barrier associated with nucleation is lower for the bulk of the solution rather than for the glass surface. These results might be explained by considering that the chances of homogeneous nucleation in the bulk of the solution are relatively low due to the unavoidable presence of foreign particles in the solution. Therefore, it might be assumed that the particles present in the solution represent more active nucleation sites for the adipic acid crystals leading to a higher experimental nucleation rate. On the other hand, the difficulties of locating the exact position where the nuclei were born might add an additional uncertainty in the experimental results by leading to over/underestimation of the nucleation rate.

Although the approach here used seemed promising to study the activity of different substrates over nucleation rate in solution, we believe that the inherently uncertainty associated with the determination of the original position where the nuclei were formed represents a huge limitation for this kind of studies. One reason is that, due to their small dimensions (in the order of nm), critical-size nuclei can travel within the bulk of the solution due to Brownian motions. Consider for example a crystalline nucleus with a radius of 10 nm, it is possible to estimate the time required to travel a distance of 50 μm from the Einstein's equation $t_{\mathcal{D}} = x^2/2\mathcal{D}$ (where x is the distance travelled and \mathcal{D} is the diffusivity calculated from equation (2.70)) to be about 1 min. It is therefore reasonable to assume

that crystals born in proximity of the glass surface or of the gas-liquid interface might diffuse towards these surfaces before the experimenter is able to detect them. As a consequence, the real position where the nucleus was formed cannot be determined unambiguously. In addition, due to the small volume of solution used, the nucleation process might reveal here its stochastic nature, in this case, the nucleation rate has to be determined using a statistical approach based on a large number of identical experiments.

Chapter 7

CONCLUSION AND FUTURE WORK

7.1 General conclusions

The main objective of this work was to advance knowledge of the crystallization process by investigating some of the key process parameters that influence nucleation under various conditions. In particular, I decided to investigate the effect of three parameters: (i) micromixing efficiency, (ii) shear rate and (iii) gas-liquid interface on primary nucleation from supersaturated solutions. Although these parameters have been reported to have an effect on nucleation (e.g. (Hem, 1967; Jawor-Baczynska et al., 2013; Liu et al., 2014; Wohlgemuth et al., 2009), the exact mechanism by which they influence nucleation is still unclear due to the lack of systematic studies. Crystallization of para-amino benzoic acid (PABA) and adipic acid from water were chosen as model systems.

In Chapter 3, I introduced the experimental systems used in this thesis to study the effect of micromixing on the nucleation of PABA in water. In particular, I characterised the micromixing efficiency of a traditional stirred tank and of a bubble column. For this purpose, a 2.3 L cylindrical vessel that could be agitated using a standard Rushton turbine or by introducing bubbles by means of a ring-shaped gas sparger was employed. For both systems, the micromixing efficiency was estimated at two locations in the vessel using a parallel-competitive reaction scheme; from the results obtained I calculated the micromixing time by implementing the IEM model for the specific reactant concentration set used. From the micromixing times obtained in this way, the local energy dissipation rate relative to the two positions considered was estimated. The results showed that for both systems a very high micromixing efficiency (comparable to that obtained in micromixing devices specifically designed to enhance micromixing) can be achieved by feeding the reactants in specific locations inside the reactor (into the trailing vortex generated by the Rushton turbine and right above the gas sparger), even at relatively low power inputs. However, the minimum micromixing time achievable (best micromixing performance) seems to be independent of the power input. In addition, its value is of the same order of magnitude for the two systems analysed. Interestingly, our results showed that, although the maximum micromixing efficiency found for the stirred tank is slightly higher than that in the bubble column, the latter is characterised by a more spatially uniform micromixing efficiency.

In Chapter 4, we compared the metastable zone width from cooling crystallization experiments of PABA in water obtained using the stirred tank and the bubble column reactor studied in Chapter 3. Our investigation demonstrates that more intense agitation of the supersaturated solution results in a narrower MZW, regardless of whether the agitation is provided by means of a stirrer or of bubbles. However, the results obtained showed that even when the two systems (stirred tank and bubble column) experience the same micromixing conditions (local energy dissipation rates), the experimental MZW is different, suggesting that micromixing is not the parameter controlling the onset of crystallization and that nucleation into the bubble column might have been significantly enhanced via a different mechanism. The same trend was observed when the experimental MZW is analysed as function of the average energy dissipation rate. Nevertheless, we have to consider that as demonstrated in Chapter 3, fluid dynamic conditions inside the vessels are quite complex and non-uniform, especially in the case of the stirred tank. This might have had an effect on crystal formation and suggests that the degree of uniformity of the mixing conditions should also be taken into account when designing the crystallization process. Therefore, it is not possible to completely discard the hypothesis that micromixing is the critical parameter controlling crystal formation in supersaturated solutions. On the other hand, the narrower MZW obtained in the case of the bubble column seems to support the hypothesis that the gas-liquid interface provided by the bubbles can act as a site for heterogeneous nucleation, thereby producing a narrower MZW. In order to investigate both theories (fluid dynamic as the parameter controlling primary nucleation or gas-liquid interface triggering heterogeneous nucleation), the series of experiments described in Chapter 5 and Chapter 6 were performed.

In Chapter 5, a droplet based crystalliser was used to study nucleation kinetics of PABA in water under well-controlled fluid dynamics conditions with the aim of clarifying the role of fluid dynamic and shear rate on primary nucleation. The PABA aqueous solution was divided into small droplets with the aid of an immiscible carrier phase and nucleation kinetics were derived using a statistical approach. In order to clarify the effect of shear rate on nucleation, both stagnant conditions (motionless droplets) and flowing conditions (droplets are forced to move inside the capillary at constant velocity so that a gentle shear field is produced) were investigated by experiment. In addition, with the aim to investigate

a larger range of shear rates, I compared my results with those obtained by Sullivan (2015), who estimated nucleation kinetics of PABA in water in small stirred vials (supersaturated solution is subject to an intense shear field). My results relative to the droplet based crystallizer demonstrate that the nucleation rate can be increased by several orders of magnitude by applying a mild shear field. However, comparison with the experimental work of Sullivan's (2015) shows that very high shear rates may produce lower nucleation rates. These results suggest that nucleation of PABA in water proceeds through a two-step nucleation mechanism where the aggregation of meso-scale clusters is enhanced by the shear field. However, high shear rates are found to hinder the cluster aggregation in the solution thereby leading to an overall decrease of the nucleation rate.

In Chapter 6, the hypothesis that gas bubbles in a supersaturated solution can act as sites for heterogeneous nucleation was investigated by performing a series of experiments in a custom-made nucleation cell where an air pocket was created to offer a gas-liquid interface for nucleation. Nucleation rates in the bulk of the solution and on the cell walls were determined by counting the number of crystals formed in a certain time span. For both cases (solution bulk and cell walls), the parameters of the nucleation rate equation (nucleation work, size of critical cluster etc.) were determined based on the Classical Nucleation Theory and the results of the calculations showed that nucleation in the bulk of the solution mainly occurs via a heterogeneous mechanism. Although nucleation rates on the gas-liquid interface could not be quantitatively assessed, the experimental results demonstrated that nucleation on a gas-liquid interface is possible.

In summary, this work demonstrates that primary nucleation can be influenced by a number of factors. Fluid dynamics and shear rate, in particular, seem to have a fundamental role in determining the onset of crystallization by enhancing the collision frequency of meso-scale clusters in solution. By quantifying the enhancement of the primary nucleation rate due to shear rate, I highlighted a non-monotonic dependence of nucleation rate on the shear rate. These results support the cluster-aggregation theory which is at the base of the Two-Step Nucleation theory. In addition, although it was not possible to perform a quantitative analysis, I demonstrated that the gas-liquid interface has the potential to trigger heterogeneous nucleation. Therefore, it is concluded that the presence of bubbles in a supersaturated solution is able to lower the energy barrier to

initiate nucleation, potentially leading to a narrower MZW. These results suggest that the nucleation rate enhancement observed in the presence of bubbles can be attributed to the combined effect of fluid dynamics and heterogeneous nucleation on the gas-liquid interface. Finally, we showed that the methodology used in Chapter 5 represents an effective way to accurately study the effect of fluid flow on primary nucleation and has the potential to enable to find a quantitative link between fluid shear and nucleation rate.

7.2 Future work

Despite some important achievements in the understanding of the factors that influence nucleation during cooling crystallization, on the basis of the present work, some suggestions for future investigations can be made.

1. The droplet based crystalliser has been demonstrated to be particularly suitable to investigate the link between fluid shear and nucleation kinetics thanks to its unique characteristics (easily controlled fluid dynamic conditions and laminar flow). In this work, we estimated the average shear rate in the capillary on the basis of previous experimental studies that characterised the flow pattern inside droplets moving in micro and milli channels. However, a more accurate estimation of the fluid dynamic regime inside the flowing droplets could be obtained by means of experimental techniques such as Particle Image Velocimetry (PIV) or fluid flow simulations. This would allow a spatial visualization of the flow profile inside the droplets of the crystallising solution enabling to carry out a deeper analysis of the nucleation data.
2. Due to time limitations, in the present work only one value of flow rate has been explored. However, it would be interesting to perform the same investigation at higher and lower flow rates. Such a study could reveal the existence of a minimum value of fluid shear below which the nucleation rate is not actually significantly enhanced with respect to the case of stagnant droplets. On the other hand, I might identify an optimal value of the shear rate that would produce the highest nucleation rate for a given supersaturation ratio. On the basis of the results obtained, we would expect that above this value of optimal shear rate nucleation rate would start to decrease.

3. The experimental study presented in Chapter 5 has been carried out assuming that the liquid-liquid interface does not constitute a possible site for heterogeneous nucleation. However, since it is shown that a gas-liquid interface has the potential to trigger heterogeneous nucleation, it would be interesting to perform experiments in similar fluid dynamic conditions (the droplet velocity would have to be adjusted in order to obtain the same average shear rate) using capillaries with different internal diameter. In this way, the surface to volume ratio of each droplet is changed and thereby also the liquid-liquid surface area possibly available for heterogeneous nucleation.
4. Due to the shape (needle shape) and the fragility of α -PABA crystals, it was not possible to measure the crystal size distribution of the crystals obtained in the stirred tank and bubble column crystallisers (Chapter 4). Therefore, a similar study may be conducted using a model compound with a different crystal habit. In particular, the slightly elongated, hexagonal shape of adipic acid has been demonstrated to be suitable for CSD determination using laser diffraction techniques (Jamshidi et al., 2016).
5. The study performed on micromixing in stirred tanks and bubble columns highlights some interesting characteristics about local energy dissipation rate and micromixing time and could be expanded by measuring the micromixing efficiency in different parts of the reactor in order to more accurately assess the effect of micromixing phenomena on nucleation in turbulent conditions, similar to those used in the industrial processes.
6. Although the study relative to the gas-liquid heterogeneous nucleation (Chapter 6) allowed us to reach important conclusions about the nucleation mechanism in the presence of a gas-liquid interface, it also highlighted the importance of considering the stochastic nature of nucleation in small volumes. In order to overcome this problem, the developed experimental setup could be improved by adding more nucleation cells within the Perspex enclosure so that the number of experiments which can be performed in parallel is increased. This would allow to quantify the nucleation rate on the gas-liquid surface and to compare the corresponding nucleation energy barrier with that obtained for the bulk of the solution and the glass surface.

Appendix A

Triiodide extinction coefficient determination

According to the Beer-Lambert law, light absorption D is proportional to I_3^- concentration through the molar extinction coefficient ϵ_λ of I_3^- at 353 nm

$$[I_3^-] = \frac{D}{\epsilon_\lambda l} \quad \text{valid for } 0.1 < D < 2.5 \quad (\text{Falk \& Commenge, 2010})$$

Where l is the optical path length, and ϵ_λ (m^2/mol) is the molar extinction coefficient of I_3^- ions at 353 nm. The parameter ϵ_λ has been determined by measuring the light absorption D of a solution at a known concentration of triiodide using a spectrophotometer. Figure A.1 shows an example of absorbance spectrum

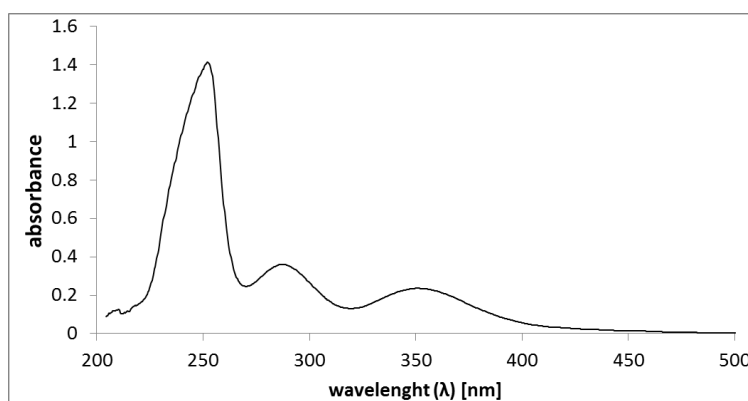
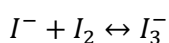
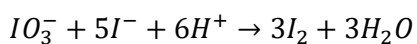


Figure A.1 Example of iodine-triiodide absorbance spectra

As triiodide solutions are not very stable, it is preferred to prepare an iodine (I_2) solution through reaction (ii) and then add a large excess of iodide (KI) to convert all the I_2 to I_3^- according to the equilibrium reaction



Appendix

The procedure used is as follow:

- Dissolve KI and KIO₃ in water making two separate solutions in order to have the following concentrations:

$$[\text{KI}] = 1.13 \text{ mM}$$

$$[\text{KIO}_3] = 0.226 \text{ mM}$$

- Mix 0.5 ml of the KI solution with 0.5 ml of the KIO₃ solution in the cuvette to be used for the spectrophotometer measurement.
- To this add an excess of sulphuric acid to convert all the iodide and iodate into iodine, adding the following concentration of acid:

$$[\text{H}^+] = 14.2 \text{ mM}$$

- To achieve this, add 1 ml of 28.4 mM H⁺ (14.2 mM H₂SO₄) to the 1 ml mixture of 2.26 mM KI and 0.452 mM KIO₃. Sulphuric acid is used for the supply of H⁺ ions.
- By combining these reagents in the quantities above, one obtains the following iodine concentration:

$$\frac{1}{5} [\text{IO}_3^-] = [\text{I}^-] = \frac{5}{3} [\text{I}_2] = 1.13 \text{ mM}$$

$$[\text{I}_2] = 0.68 \text{ mM}$$

- After about 5 min the reaction should be completed and the process of diluting the sample and measuring the absorbance can commence. It is recommended to dilute the solution directly into the cuvette by taking out some of the solution and adding DI water.
- By diluting the iodine to 20%, 40%, 60%, 80% and 100% the original concentration and measuring the absorbance at 460 nm peak using UV-Vis spectra, one can obtain the extinction coefficient at this wavelength for iodine: $\epsilon_{\lambda}(\text{I}_2) = 653 \text{ m}^2/\text{mol}$

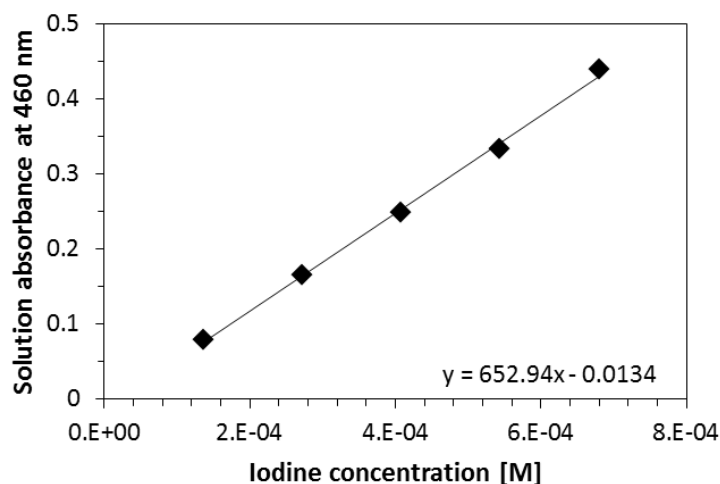
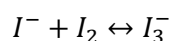


Figure A.2 Solution absorbance at 460 nm ($R^2 = 0.998$).

Following this, one can make the necessary concentration for triiodide calculations. To do this the saturation method is used. In this method, we take a known concentration of iodine and saturate the quantity with iodide as per the following reaction:



By using a large excess of iodide ions (about 7000x), the equilibrium is driven largely in favour of the triiodide ion. By adding a large excess of KI, in this case 0.321 M KI was added to a known concentration of 46.4 μ M iodine (I recommend using the last iodine solution measured), it is assumed all iodine converts to triiodide. Then measure triiodide concentration by analysing peak at 353 nm, making dilute concentrations from the initial known concentration to assemble calibration curve.

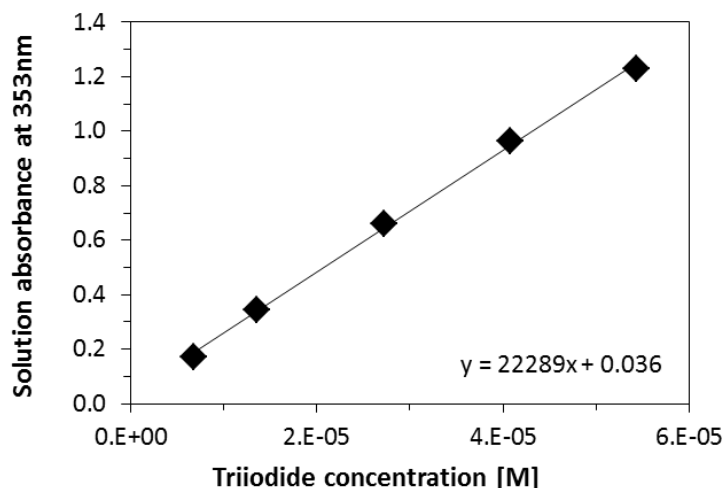


Figure A.3 Solution absorbance at 353 nm ($R^2 = 0.998$)

In each case, the slope of the line gives the molar extinction coefficient in $\text{l/mol}\cdot\text{cm}$ as per the beer lambert law equation:

$$A = \epsilon_{\lambda}cl$$

In the case where path length is 1 cm, the slope is equal to the extinction coefficient. $\epsilon_{\lambda} = 2229 \text{ m}^2/\text{mol}$

The obtained value is in good agreement with results given in the literature (Table A.1). The observed deviations may be explained by the diversity of the apparatus used.

Table A.1 Triiodide extinction coefficient values from literature and this work.

Reference	Wavelength λ [nm]	Extinction coefficient ϵ_{λ} [m^2/mol]
Custer & Natelson, 1949	352	2590
Awtrey & Connick, 1951	353	2640
Herbo & Sigalla, 1957	350	2510
Rousseaux et al., 2000	353	2575
Guichardon & Falk, 2000 (single beam spectroscopy)	353	2396

Appendix

Guichardon & Falk, 2000 (double beam spectroscopy)	353	2606
This work	353	2229

Appendix B

Acid injection procedure

In order to be sure to inject the selected amount of sulphuric acid I connected the feeding pipe to a 1 mm capillary; the length of this capillary is chosen so that its volume is approximately 1 ml. This capillary is connected to a shorter capillary (28 mm length, 0.8 mm diameter) through a PEEK shut-off valve; the approximate volume of this capillary is 0.141 ml.

A glass syringe (2.5 ml volume) is filled with 1 ml or more of sulphuric acid (0.75 M) and connected to the series of capillary described above. Using a syringe pump, we slowly (0.1 ml/min) push 1.141 ml of sulphuric acid through the channel. Once the pump stops we should close the shut off valve and disconnect the shorter capillary from it. Sulphuric acid has to be now washed out from this capillary and from the syringe; this can be done by simply using DI water. After that the capillary should be dried and connected to the syringe filled with at least 1.5 ml of DI water.

The syringe pump can be then started at the desired flow rate (0.5 ml/min) in order to run the micromixing characterization experiment.

It should be noticed that this simple procedure enables injection of the exact quantity of acid required and prevent the acid to coming into contact with the reactants before the start of the injection period.

Appendix C

Metastable zone width determination for the droplet based crystallizer

To measure the metastable zone width for our system, we generated about 400 droplets of PABA solution saturated at 27 °C (5.74 mg_{PABA}/ml_{H₂O}) within a PTFE transparent capillary as described in section 5.2.2. After the droplets have filled the whole length of the channel both ends of it were sealed and the capillary was placed in a thermostatic water bath at $T < T_{\text{sat}}$ for a time longer than t_{GE} used in the experiments described in Chapter 5. After the set time was elapsed, we observed the droplets using a standard optical microscope as described in section 5.2.2 and verified that no crystals were present in the droplets after this time.

The results obtained are depicted in Figure C.1 and show that no crystals were formed for $T_{\text{sat}} > T \geq 23$ °C, while for $T = 22$ °C a few droplets contained crystals, for $T < 22$ °C we observed that most of the droplets contained at least one crystal.

On the basis of these results we chose the temperature T_g of the growth stage for the experiments described in section 5.2.2 to be 23 °C.

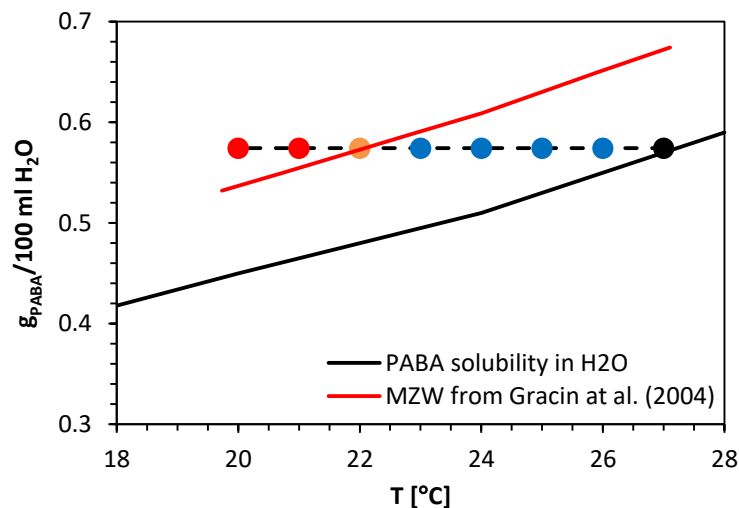


Figure C.1 Comparison between the metastable zone found for the experimental conditions described in Chapter 5 and the one reported by Gracin et al. (2004) (red line); the blue dots represent the condition in which no crystals were observed; orange dot represents the condition for which crystals were observed in a few droplets; the red dots represent the conditions for which crystals were observed in more than 70% of the droplets.

Appendix D

Image processing using Matlab®

```

%% image analysis %%
% Read all the jpg files in the specified folder,
% crop and rotate them according to the user input.
% Binarize the images using modified Otsu's method and measure
bubble length and velocity.
% Plot the results of the measurements and calculate the mean, the
standard deviation and the standard error.

%% initialize
clear all;
close all;
clc; i=1; a=1; e=1;
w='n'; k=1;

%% manipulate data files
% read all the data
filename = uigetdir;
fprintf('You are going to analyse the files in the following
folder:\n %s \n',filename);
red_fact=input('insert reducing factor for Otsu threshold (usually
between 0.8-0.9): ');
num_im = input('how many picture do you want display? ');
cd(filename)
files = dir('*.tif');
for k=1:length(files)
    data = imread(files(k).name);

    %% Crop and rotate
    if k == 1
        angle = input('specify the rotation angle (degree,
+anticlockwise): ');
        data = imrotate(data,angle,'bicubic');
        [data,crop_lim] = imcrop(data);
    else
        data = imrotate(data,angle,'bicubic');
        data = imcrop(data,crop_lim);
    end

    [y_pix,x_pix]=size(data);
    dc_ext = 1 ;           % Capillary diameter [=] millimeters
    conv_fact=dc_ext/205; % Conversion factor [=] millimeters/pixel

    plot original image (and histogram)
    figure(i); i=i+1;
    imshow(data);
    axis equal;
    title('Original image')
    figure(i); i=i+1;
    imhist(data);

```

Appendix

```
figure(i); i=i+1;
contourf(data(:,:,1));
axis equal;
title('Original image contour');

%% Manipulation of the histogram
mod_im = imsharpen(data);
figure(i); i=i+1;
imshow(mod_im);
axis equal;
title('Sharpened image using "imsharpen"')

%% Binarization and cleaning
[threshhold,EM]=graythresh(mod_im);
bin_im=im2bw(mod_im,threshhold*red_fact);
if k <= num_im
figure(i); i=i+1;
imshow(bin_im);
axis equal;
title('Binarized image')
end

bin_im=imcomplement(bin_im); % inverting the binary image
figure(i); i=i+1;
imshow(bin_im);
axis equal; title('inverted')

bin_im(:,[1 2 3])=0;bin_im(:,[x_pix-2 x_pix-1 x_pix])=0;
figure(i); i=i+1;
imshow(bin_im);
axis equal; title('dx and sin line')
spy(bin_im);

small=20;
if dc_ext>2
    small=300;
end
bin_im=bwareaopen(bin_im,small); %removing small objects
if k <= num_im
figure(i); i=i+1;
imshow(bin_im);
axis equal;
title('Modified binarized image (removing small objects)')
end

%% Cleaning
bin_im=bwareaopen(bin_im,small); %removing small objects
figure(i); i=i+1;
imshow(bin_im);
axis equal;
title('Modified binarized image (removing small objects)')

%% Measurements
```

Appendix

```
measurements = regionprops(bin_im, 'all');

%% Bubble volume measurements
filled=imfill(bin_im, 'holes'); %
figure(i); i=i+1;
imshow(filled);
axis equal;
title('filled')

perimeter=bwperim(filled); %
figure(i); i=i+1;
imshow(perimeter);
axis equal;
title('perimeter')

half = imcrop(perimeter, [0,0,x_pix,y_pix/2]);
half=bwareaopen(half,5); %removing small objects
figure(i); i=i+1;
imshow(half);
axis equal;
title('half perimeter')

volume_measurements = regionprops(half, 'all');
x=volume_measurements.PixelList(:,1);
y=volume_measurements.PixelList(:,2);
[x1,y1] = vectorcleaner(x,y);
ymax=max(y1);
y2=y1-ymax;
rc=dc_ext/2; %mm
rB=ymax-min(y1);
x1=x1*conv_fact;
y2=y2*rc/rB;

volume(k)=pi*trapz(x1,y2.^2);

N=length(y2);
figure(i); i=i+1;
cylinder(y2,N);

end

volume_av = mean(volume);
stand_dev=std(volume);
fprintf('the average droplet volume is %0f',volume_av);
```

Appendix E

Raw data Chapter 3

E.1 Stirred tank

Below are reported the values of the segregation index X_s , the micromixedness ratio α , the micromixing time t_{μ} , and the local energy dissipation rate ϵ_T (W/kg) obtained for the stirred tank. Table E.1 and Table E.2 refer to the results relative to position <1>, while Table E.3 and Table E.4 refer to the results relative to position <2> (position <1> and <2> for the stirred tank are defined in section 3.2.4). The value of X_s *average* is calculated as the arithmetic mean of three values of X_s obtained from three repeated experiments (X_{s1} , X_{s2} and X_{s3}). The micromixedness ratio α is calculated from the segregation index X_s according to equation (3.17). The micromixing time is derived from the micromixedness ratio α according to the IEM model described in section 2.2.3.3; the solution of the IEM model for the particular experimental conditions used in Chapter 3 is presented in section 3.3.1. The local energy dissipation rate is calculated from the micromixing time according to equation (2.51). Standard deviations for all values are also reported. All values have been reported as functions of the stirrer rotational speed N (1/s) and the average dissipation rate ϵ_{av} (W/kg) as defined in equation (2.64).

Appendix

Table E.1 Segregation index X_S and micromixedness ratio α as function of the rotational stirring rate N and average energy dissipation ϵ_{av} for the stirred tank relative to POSITION <1>.

N 1/s	ϵ_{av} W/kg	X_S 1	X_S 2	X_S 3	X_S average	X_S st.dev	α 1	α 2	α 3	α average	α st.dev
2.4	0.002	0.115	0.099	0.129	0.114	0.012	7.7	9.1	6.8	7.9	0.96
4.6	0.014	0.084	0.101	0.074	0.086	0.011	11.0	8.9	12.5	10.8	1.46
6.3	0.034	0.068	0.072	0.076	0.072	0.003	13.7	12.9	12.1	12.9	0.64
9.6	0.108	0.061	0.065	0.059	0.062	0.002	15.3	14.5	15.9	15.2	0.57
10.3	0.131	0.062	0.059	0.055	0.059	0.003	15.0	16.1	17.1	16.0	0.83
11.3	0.169	0.057	0.059	0.054	0.057	0.002	16.5	15.9	17.5	16.6	0.65
11.6	0.181	0.050	0.056	0.055	0.053	0.003	19.1	16.9	17.3	17.7	0.99
13.7	0.288	0.057	0.050	0.050	0.052	0.003	16.7	18.8	18.8	18.1	1.02
16	0.441	0.046	0.043	0.048	0.046	0.002	20.8	22.0	19.6	20.8	0.97

Appendix

Table E.2 Micromixing time t_μ and local energy dissipation ϵ_G as function of rotational stirring rate N and average energy dissipation ϵ_{av} for the stirred tank relative to POSITION <1>.

N 1/s	ϵ_{av} W/kg	t_μ 1 s	t_μ 2 s	t_μ 3 s	t_μ average s	t_μ st.dev s	ϵ_T 1 W/kg	ϵ_T 2 W/kg	ϵ_T 3 W/kg	ϵ_T average W/kg	ϵ_T st.dev W/kg
2.4	0.002	0.983	0.299	3.15	1.478	1.216	3.09×10^{-4}	3.33×10^{-3}	3.00×10^{-5}	1.22×10^{-3}	1.50×10^{-3}
4.6	0.014	0.103	0.346	0.056	0.168	0.127	0.028	0.002	0.096	0.042	0.039
6.3	0.034	0.038	0.049	0.065	0.050	0.011	0.21	0.13	0.07	0.13	0.06
9.6	0.108	0.024	0.030	0.021	0.025	0.004	0.50	0.33	0.65	0.49	0.13
10.3	0.131	0.026	0.020	0.017	0.021	0.004	0.44	0.71	1.08	0.74	0.26
11.3	0.169	0.019	0.021	0.015	0.018	0.002	0.86	0.65	1.26	0.92	0.25
11.6	0.181	0.012	0.017	0.016	0.015	0.002	2.25	0.99	1.16	1.47	0.55
13.7	0.288	0.018	0.012	0.012	0.014	0.003	0.92	2.05	2.05	1.68	0.53
16	0.441	0.009	0.008	0.011	0.009	0.001	3.7	5.0	2.6	3.79	0.61

Appendix

Table E.3 Segregation index X_s and micromixedness ratio α as function of rotational stirring rate N and average energy dissipation ϵ_{av} for the stirred tank relative to POSITION <2>.

N 1/s	ϵ_{av} W/kg	X_s 1	X_s 2	X_s 3	X_s average	X_s st.dev	α 1	α 2	α 3	α average	α st.dev
4.3	0.012	0.117	0.129	0.115	0.120	0.006	7.5	6.7	7.7	7.3	0.43
6.8	0.042	0.094	0.101	0.087	0.094	0.006	9.7	8.9	10.5	9.7	0.65
7.7	0.059	0.090	0.099	0.084	0.091	0.006	10.1	9.1	10.9	10.1	0.73
10.2	0.128	0.076	0.087	0.073	0.079	0.006	12.2	10.5	12.7	11.8	0.94
11.4	0.173	0.081	0.071	0.066	0.073	0.006	11.4	13.1	14.1	12.8	1.12
12.7	0.233	0.060	0.059	0.069	0.063	0.004	15.7	15.9	13.5	15.0	1.09
14.3	0.325	0.062	0.060	0.065	0.062	0.002	15.2	15.7	14.5	15.1	0.49
14.6	0.343	0.065	0.063	0.059	0.062	0.003	14.4	14.8	16.1	15.1	0.71
16	0.441	0.059	0.063	0.055	0.059	0.003	16.1	14.9	17.1	16.0	0.89

Appendix

Table E.4 Micromixing time t_μ and local energy dissipation ϵ_G as function of the rotational stirring rate N and average energy dissipation ϵ_{av} for the stirred tank relative to POSITION <2>.

N 1/s	ϵ_{av} W/kg	t_μ 1 s	t_μ 2 s	t_μ 3 s	t_μ average s	t_μ st.dev s	ϵ_T 1 W/kg	ϵ_T 2 W/kg	ϵ_T 3 W/kg	ϵ_T average W/kg	ϵ_T st.dev W/kg
4.3	0.012	1.22	3.35	0.97	1.848	1.068	1.99×10^{-4}	2.66×10^{-5}	3.19×10^{-4}	1.81×10^{-4}	1.20×10^{-4}
6.8	0.042	0.204	0.346	0.127	0.226	0.090	0.007	0.002	0.018	0.009	0.007
7.7	0.059	0.155	0.299	0.106	0.187	0.082	0.012	0.003	0.027	0.014	0.010
10.2	0.128	0.061	0.127	0.052	0.080	0.034	0.08	0.02	0.11	0.07	0.04
11.4	0.173	0.086	0.046	0.034	0.055	0.023	0.04	0.14	0.26	0.15	0.09
12.7	0.233	0.022	0.021	0.040	0.028	0.009	0.61	0.65	0.18	0.48	0.21
14.3	0.325	0.025	0.022	0.030	0.026	0.003	0.47	0.59	0.33	0.46	0.11
14.6	0.343	0.031	0.028	0.020	0.026	0.004	0.31	0.39	0.71	0.47	0.17
16	0.441	0.020	0.027	0.017	0.021	0.004	0.71	0.40	1.08	0.73	0.28

E.2 Bubble column

Below are reported the values of the segregation index X_s , the micromixedness ratio α , the micromixing time t_{μ} , and the local energy dissipation rate ϵ_G (W/kg) obtained for the bubble column. Table E.5 and Table E.6 refer to the results relative to position <1>, while Table E.7 and Table E.8 refer to the results relative to position <2> (position <1> and <2> are defined in section 3.2.4). The value of X_s *average* is calculated as the arithmetic mean of three values of X_s obtained from four repeated experiments (X_s 1, X_s 2, X_s 3 and X_s 4). The micromixedness ratio α is calculated from the segregation index X_s according to equation (3.17). The micromixing time is derived from the micromixedness ratio α according to the IEM model described in section 2.2.3.3; the solution of the IEM model for the particular experimental conditions used in Chapter 3 is presented in section 3.3.1. The local energy dissipation rate is calculated from the micromixing time according to equation (2.51). Standard deviations for all values are also reported. All values have been reported as functions of the gas flow rate Q (L/min) and the average dissipation rate ϵ_{av} (W/kg) as defined in equation (2.66).

Table E.5 Segregation index X_s and micromixedness ratio α as function of gas flow rate Q and average energy dissipation ϵ_{av} for the bubble column relative to POSITION <1>.

Q L/min	ϵ_{av} W/kg	X_s 1	X_s 2	X_s 3	X_s 4	X_s average	X_s st.dev	α 1	α 2	α 3	α 4	α average	α st.dev
1	0.014	0.106	0.102	0.104	0.086	0.099	0.008	8.5	8.8	8.6	10.7	9.1	0.88
2	0.029	0.104	0.090	0.104	0.097	0.099	0.006	8.6	10.1	8.6	9.3	9.1	0.61
3.5	0.051	0.081	0.090	0.084	0.080	0.084	0.004	11.3	10.1	10.9	11.4	10.9	0.53
5	0.072	0.077	0.076	0.075	0.070	0.074	0.002	12.0	12.2	12.3	13.2	12.4	0.45
7	0.101	0.069	0.070	0.068	0.064	0.068	0.002	13.4	13.2	13.8	14.6	13.7	0.54
9	0.130	0.065	0.066	0.061	0.062	0.064	0.002	14.4	14.1	15.4	15.1	14.7	0.50

Appendix

Table E.6 Micromixing time t_{μ} and local energy dissipation ϵ_G as function of gas flow rate Q and average energy dissipation ϵ_{av} for the bubble column relative to POSITION <1>.

Q L/min	ϵ_{av} W/kg	t_{μ} 1 s	t_{μ} 2 s	t_{μ} 3 s	t_{μ} 4 s	t_{μ} average s	t_{μ} st.dev s	ϵ_G 1 W/kg	ϵ_G 2 W/kg	ϵ_G 3 W/kg	ϵ_G 4 W/kg	ϵ_G average W/kg	ϵ_G st.dev W/kg
1	0.014	0.49	0.38	0.43	0.12	0.354	0.142	0.0012	0.002	0.002	0.021	0.0066	0.01
2	0.029	0.44	0.16	0.44	0.27	0.329	0.120	0.0015	0.012	0.002	0.004	0.0047	0.004
3.5	0.051	0.09	0.16	0.11	0.08	0.109	0.030	0.038	0.012	0.03	0.04	0.0300	0.01
5	0.072	0.07	0.06	0.06	0.04	0.058	0.008	0.068	0.077	0.09	0.15	0.0967	0.03
7	0.101	0.04	0.04	0.04	0.03	0.038	0.006	0.174	0.15	0.22	0.35	0.2248	0.08
9	0.130	0.03	0.03	0.02	0.03	0.029	0.004	0.31	0.27	0.51	0.44	0.3836	0.05

Table E.7 Segregation index X_s and micromixedness ratio α as function of gas flow rate Q and average energy dissipation ϵ_{av} for the bubble column relative to POSITION <2>.

Q L/min	ϵ_{av} W/kg	X_s 1	X_s 2	X_s 3	X_s 4	X_s average	X_s st.dev	α 1	α 2	α 3	α 4	α average	α st.dev
1	0.014	0.022	0.113	0.116	0.114	0.115	0.115	7.82	7.60	7.76	7.67	7.71	0.09
2	0.029	0.043	0.114	0.107	0.110	0.111	0.110	7.74	8.34	8.11	8.05	8.06	0.25
3.5	0.051	0.076	0.105	0.109	0.098	0.103	0.104	8.50	8.19	9.19	8.75	8.66	0.42
5	0.072	0.108	0.096	0.097	0.104	0.090	0.097	9.36	9.30	8.62	10.11	9.35	0.53
7	0.101	0.152	0.087	0.095	0.088	0.081	0.088	10.53	9.52	10.42	11.29	10.44	0.63
9	0.130	0.195	0.081	0.080	0.085	0.075	0.080	11.38	11.55	10.70	12.30	11.48	0.57

Appendix

Table E.8 Micromixing time t_μ and local energy dissipation ϵ_G as function of gas flow rate Q and average energy dissipation ϵ_{av} for the bubble column relative to POSITION <2>.

Q L/min	ϵ_{av} W/kg	t_μ 1 s	t_μ 2 s	t_μ 3 s	t_μ 4 s	t_μ average s	t_μ st.dev s	ϵ_G 1 W/kg	ϵ_G 2 W/kg	ϵ_G 3 W/kg	ϵ_G 4 W/kg	ϵ_G average W/kg	ϵ_G st.dev W/kg
1	0.014	0.87	1.12	0.93	1.03	0.989	0.097	3.95×10^{-4}	2.37×10^{-4}	3.43×10^{-4}	2.79×10^{-4}	3.14×10^{-4}	6.04×10^{-5}
2	0.029	0.96	0.55	0.67	0.71	0.723	0.173	3.25×10^{-4}	1.00×10^{-3}	6.72×10^{-4}	5.98×10^{-4}	6.67×10^{-4}	2.77×10^{-4}
3.5	0.051	0.48	0.62	0.29	0.39	0.462	0.137	1.30×10^{-3}	7.75×10^{-4}	3.66×10^{-3}	1.92×10^{-3}	1.91×10^{-3}	1.26×10^{-3}
5	0.072	0.25	0.26	0.43	0.16	0.277	0.100	0.0047	0.0043	0.0016	0.0121	0.0057	3.91×10^{-3}
7	0.101	0.13	0.23	0.13	0.09	0.144	0.051	0.019	0.006	0.017	0.038	0.020	1.14×10^{-2}
9	0.130	0.09	0.08	0.12	0.06	0.085	0.020	0.041	0.047	0.022	0.084	0.048	2.23×10^{-2}

Appendix F Raw data Chapter 4

F.1 Stirred tank

Below are reported the values of the metastable zone width MZW ($^{\circ}\text{C}$) (as defined in equation (4.2)) and the maximum supersaturation (as defined in equation (4.3)) relative to the experiments reported in Chapter 4. Table F.1 refers to the results obtained using the conductivity meter measurements while Table F.2 refers to the results obtained using naked eye observation, the difference between the two techniques is discussed in section 4.3.3. The average values (*MZW average* and *S average*) are calculated as the arithmetic mean of three separated measurements (*MZW1*, *MZW2*, *MZW3* and *S_{max 1}*, *S_{max 2}*, *S_{max 3}*). Standard deviations for all the values have also been reported. All values have been reported as function of the rotational stirring rate *N* (1/s), average energy dissipation rate ϵ_{av} (W/kg) defined in equation (2.64) and the local maximum energy dissipation rate $\epsilon_{\text{local-maximum}}$ (W/kg) (equation (3.20) for position <1>).

Table F.1 Metastable zone width and maximum supersaturation measured by conductivity meter for the stirred tank.

N 1/s	ϵ_{av} W/kg	$\epsilon_{\text{local-max}}$ W/kg	MZW1 $^{\circ}\text{C}$	MZW2 $^{\circ}\text{C}$	MZW3 $^{\circ}\text{C}$	MZW average $^{\circ}\text{C}$	MZW st.dev $^{\circ}\text{C}$	S_{max1}	S_{max 2}	S_{max 3}	S average	S st.dev
3.0	0.004	0.01	10.3	10.0	9.8	10.0	0.2	1.47	1.45	1.44	1.46	0.012
6.3	0.040	0.09	9.2	9.3	8.9	9.1	0.2	1.41	1.42	1.40	1.41	0.009
8.7	0.107	0.33	8.5	8.7	8.8	8.6	0.1	1.37	1.39	1.39	1.38	0.007
10.9	0.214	0.83	8.3	8.0	8.6	8.3	0.2	1.37	1.35	1.38	1.37	0.013
15.9	0.663	3.68	6.0	6.3	5.8	6.0	0.2	1.25	1.27	1.25	1.26	0.009

Appendix

Table F.2 Metastable zone width and maximum supersaturation resulting from naked eye observations for the stirred tank.

N 1/s	ϵ_{av} W/kg	$\epsilon_{local-max}$ W/kg	MZW1 °C	MZW2 °C	MZW3 °C	MZW average °C	MZW st.dev °C	S_{max1}	S_{max2}	S_{max3}	S average	S st.dev
3.0	0.004	0.01	7.9	9.9	9.2	9.0	0.8	1.35	1.45	1.41	1.40	0.043
6.3	0.040	0.09	9.1	7.6	8.7	8.5	0.6	1.41	1.33	1.39	1.38	0.033
8.7	0.107	0.33	7.5	8.7	8	8.1	0.5	1.33	1.39	1.35	1.35	0.025
10.9	0.214	0.83	7.8	6.9	7.8	7.5	0.4	1.34	1.30	1.34	1.33	0.021
15.9	0.663	3.68	5.8	5.5	4.65	5.3	0.5	1.24	1.23	1.19	1.22	0.022

F.2 Bubble column

Below are reported the values of the metastable zone width MZW (°C) (as defined in equation (4.2)) and the maximum supersaturation (as defined in equation (4.3)) relative to the experiments reported in Chapter 4. Table F.3 refers to the results obtained using the conductivity meter measurements while Table F.4 refers to the results obtained using naked eye observation, the difference between the two techniques is discussed in section 4.3.3. The average values (*MZW average* and *S average*) are calculated as the arithmetic mean of three separated measurements (*MZW1*, *MZW2*, *MZW3* and *S_{max 1}*, *S_{max 2}*, *S_{max 3}*). Standard deviations for all the values have also been reported. All values have been reported as function of the gas flow rate Q (L/min), average energy dissipation rate ϵ_{av} (W/kg) defined in equation (2.66) and the local maximum energy dissipation rate $\epsilon_{local-maximum}$ (W/kg) (equation (3.21) for position <1>).

Appendix

Table F.3 Metastable zone width and maximum supersaturation measured by conductivity meter for the bubble column.

Q L/min	ϵ_{av} W/kg	$\epsilon_{local-max}$ W/kg	MZW1 °C	MZW2 °C	MZW3 °C	MZW average °C	MZW st.dev °C	S_{max1}	S_{max2}	S_{max3}	S average	S st.dev
1	0.014	9.99×10^{-4}	7	6.6	7.35	7.0	0.3	1.30	1.28	1.32	1.30	0.015
2	0.029	6.57×10^{-3}	6.2	6.7	6.5	6.5	0.2	1.26	1.29	1.28	1.28	0.010
3.5	0.051	3.01×10^{-2}	6.5	5.7	5.75	6.0	0.4	1.28	1.24	1.24	1.25	0.017
5	0.072	7.93×10^{-2}	5.7	5.74	6.2	5.9	0.2	1.24	1.24	1.26	1.25	0.011
7	0.101	1.98×10^{-1}	5.62	5.75	5.83	5.7	0.1	1.24	1.24	1.25	1.24	0.004
9	0.130	3.92×10^{-1}	5.35	5.55	6	5.6	0.3	1.22	1.23	1.25	1.24	0.013

Table F.4 Metastable zone width and maximum supersaturation resulting from naked eye observations for the bubble column.

Q L/min	ϵ_{av} W/kg	$\epsilon_{local-max}$ W/kg	MZW1 °C	MZW2 °C	MZW3 °C	MZW average °C	MZW st.dev °C	S_{max1}	S_{max2}	S_{max3}	S average	S st.dev
1	0.014	9.99×10^{-4}	6.50	6.3	6.1	6.3	0.2	1.28	1.27	1.26	1.27	0.008
2	0.029	6.57×10^{-3}	5.80	6	5.6	5.8	0.2	1.24	1.25	1.23	1.24	0.008
3.5	0.051	3.01×10^{-2}	5.80	6	5.8	5.9	0.1	1.24	1.25	1.24	1.25	0.004
5	0.072	7.93×10^{-2}	4.3	5.9	5.2	5.1	0.7	1.18	1.25	1.22	1.21	0.030
7	0.101	1.98×10^{-1}	4.6	6	4.7	5.1	0.6	1.19	1.25	1.19	1.21	0.029
9	0.130	3.92×10^{-1}	4.7	5.55	5	5.08	0.4	1.19	1.23	1.21	1.21	0.016

Appendix G

Raw data Chapter 5

Below are reported the experimental average values of the probability of nucleation as defined in equation (2.31) for different supersaturation ratios as function of the nucleation time, set a priori, for the experiments performed in Chapter 5. Table G.1 refers to the experiments performed in stagnant conditions (static droplets) while Table G.2 refers to flowing conditions experiments (moving droplets). Standard deviation is also reported.

Table G.1 Experimental probability, $P_E(t,V,S)$ determined according to equation (2.31) as function of the nucleation time at different supersaturation ratios (2.29, 2.37, 2.47) in stagnant conditions (static droplets).

S = 2.47			S = 2.37			S = 2.29		
nucleation time	Probability	st.dev	nucleation time	Probability	st.dev	nucleation time	Probability	st.dev
hours	$P_E(t,V,S)$		h	$P_E(t,V,S)$		h	$P_E(t,V,S)$	
25	0.32	0.079	30	0.34	0.070	22	0.10	0.068
39	0.47	0.074	45	0.41	0.041	27	0.12	0.065
67	0.73	0.070	71	0.58	0.065	49	0.25	0.065
95	0.86	0.082	93	0.75	0.057	73	0.30	0.074
135	0.93	0.056	120	0.83	0.078	100	0.50	0.080
169	0.91	0.053				166	0.68	0.128

Appendix

Table G.2 Experimental probability, $P_E(t,V,S)$ determined according to equation (2.31) as function of the nucleation time at different supersaturation ratios (2.02, 2.29, 2.47) in flowing conditions (moving droplets).

S = 2.47			S = 2.29			S = 2.02		
nucleation time	Probability	st.dev	nucleation time	Probability	st.dev	nucleation time	Probability	st.dev
min	$P_E(t,V,S)$		min	$P_E(t,V,S)$		min	$P_E(t,V,S)$	
200	0.18	0.061	200	0.16	0.069	200	0.23	0.090
300	0.25	0.074	420	0.46	0.057	420	0.34	0.073
420	0.48	0.056	900	0.81	0.049	900	0.61	0.060
900	0.73	0.062				1414	0.90	0.048

Appendix H

Raw data Chapter 6

Below are reported the experimental values of the number of crystals detected in i) the bulk of solution, ii) on the glass surface and iii) the gas-liquid interface relative to the experiments presented in Chapter 6. Table H.1, Table H.2 and Table H.3 refer to the number of crystals counted in the bulk of solution per mm^3 of solution (the volume of solution considered for these experiments is 1.5 mm^3). Table H.4, Table 7.20 and Table 7.21 refer to the number of crystals per mm^2 counted on the glass surface. Table H.7, Table H.8 and Table H.9 refer to the number of crystals per mm^2 counted on the gas-liquid surface. All values are reported as function of the nucleation time and refer to different supersaturation ratios (2.09, 2.18, 2.30). The average values (*Number of crystals per mm^3 average*) are the result of three repetitions, standard deviations are also reported.

Table H.1 Number of nuclei counted in the bulk of solution per mm^3 of solution as function of nucleation time at $S = 2.09$ ($T = 10 \text{ }^\circ\text{C}$).

Nucleation time min	Number of crystals per mm^3 average	Number of crystals per mm^3 st.dv			
360	0	1	0	0.2	0.3
480	4	4	1	2.9	1.6
540	6	5	4	5.2	0.8
660	7	9	8	7.9	0.8
780	8	9	11	9.4	1.0
840	9	11	9	9.8	0.6
960	9	11	9	10	1
1080	9	10	11	10	1

Appendix

Table H.2 Number of nuclei counted in the bulk of solution per mm³ of solution as function of nucleation time at S = 2.18 (T = 9.5 °C).

Nucleation time min	Number of crystals per mm ³ average	Number of crystals per mm ³ st.dv			
200	0	1	0	0.2	0.3
250	0.6	4	4	2.9	1.6
360	13	6	10	9.4	2.8
500	9	12	10	10.2	1.3
600	11	13	9	11.0	1.3
720	11	13	11	11.5	0.8
850	12	13	11	11.7	0.8

Table H.3 Number of nuclei counted in the bulk of solution per mm³ of solution as function of nucleation time at S = 2.30 (T = 8.8 °C).

Nucleation time min	Number of crystals per mm ³ average	Number of crystals per mm ³ st.dv			
30	0	2	0	0.6	0.9
60	4	3	8	5.0	1.8
90	8.75	10	14	10.8	2.1
120	11.25	15	16	14.0	1.9
150	18.75	13	16	15.6	2.6
250	16.875	19	16	17.1	1.3

Appendix

Table H.4 Number of nuclei counted on the glass surface per mm² as function of nucleation time at S = 2.09 (T = 10 °C).

Nucleation time min	Number of crystals per mm ² average	Number of crystals per mm ² st.dv			
360	0.6	0.0	0.8	0.5	0.3
480	0.5	1.6	2.3	1.5	0.8
540	2.0	3.1	3.9	3.0	0.8
660	5.5	4.7	4.7	4.9	0.4
780	8.8	6.3	7.0	7.3	1.0
840	7.8	7.0	8.1	7.7	0.5
960	7.3	8.0	8.4	7.9	0.4
1080	0.6	0.0	0.8	0.5	0.3

Table H.5 Number of nuclei counted on the glass surface per mm² as function of nucleation time at S = 2.18 (T = 9.5 °C).

Nucleation time min	Number of crystals per mm ² average	Number of crystals per mm ² st.dv			
200	0.0	0.6	0.5	0.4	0.3
250	1.6	1.3	1.9	1.6	0.3
360	5.9	3.9	4.7	4.8	0.8
500	10.3	4.7	8.0	7.7	2.3
600	11.1	13.1	10.2	11.5	1.2
850	12.7	8.6	9.4	10.2	1.8

Appendix

Table H.6 Number of nuclei counted on the glass surface per mm² as function of nucleation time at S = 2.30 (T = 8.8 °C).

Nucleation time min	Number of crystals per mm ² average	Number of crystals per mm ² st.dv			
30	0.8	1.1	0.3	0.7	0.3
60	3.9	4.7	5.5	4.7	0.6
90	7.0	5.5	8.0	6.8	1.0
120	12.7	14.4	10.9	12.7	1.4
150	14.8	10.8	13.3	13.0	1.7
250	10.2	9.4	18.8	12.8	4.2

Table H.7 Number of nuclei counted on the gas-liquid interface per mm² as function of nucleation time at S = 2.09 (T = 10 °C).

Nucleation time min	Number of crystals per mm ² average	Number of crystals per mm ² st.dv			
360	0.0	1.6	0.0	0.5	0.8
480	0.0	3.2	0.0	1.1	1.5
660	0.0	6.4	3.2	3.2	2.6
960	0.0	1.6	1.6	1.1	0.8
1080	0.0	3.2	4.8	2.7	2.0

Appendix

Table H.8 Number of nuclei counted on the gas-liquid interface per mm² as function of nucleation time at S = 2.18 (T = 9.5 °C).

Nucleation time min	Number of crystals per mm ² average	Number of crystals per mm ² st.dv			
250	0.0	1.6	0.0	0.5	0.8
360	6.4	0.0	1.6	2.7	2.7
500	0.0	1.6	0.0	0.5	0.8
720	6.4	0.0	0.0	2.1	3.0

Table H.9 Number of nuclei counted on the gas-liquid interface per mm² as function of nucleation time at S = 2.30 (T = 8.8 °C).

Nucleation time min	Number of crystals per mm ² average	Number of crystals per mm ² st.dv			
60	0.0	1.6	0.0	0.5	0.8
120	1.6	1.6	3.2	2.1	0.8
250	1.6	0.0	1.6	1.1	0.8

List of symbols

Latin letters

A	Area (m^2)
A	kinetic parameter of nucleation rate equation ($m^3 s^{-1}$ or $m^2 s^{-1}$), section 2.1 and Chapt 5 and 6
A	absorbance (-), Appendix A
a, a'	fitting parameters, eq. 4.1
B	thermodynamic parameter (-), section 2.1 and Chapt. 5 and 6
b, b'	fitting parameters , eq. 4.1
C	equilibrium concentration of critical-sized clusters, eq. 2.16
c, C	concentration
C	cluster, eq. 2.15
C_0	concentration of nucleation centres (m^{-3}), section 2.1
C_{eq}	equilibrium concentration
\mathcal{C}	electrical conductivity ($\mu S/cm$), eq. 4.1
Ca	Capillary number (-)
D	absorbance (-), Appendix A
d,D	diameter (m)
dm/dt	mass flux of solute molecules, eq. 2.44 and 2.45
\mathcal{D}	diffusivity ($m^2 s^{-1}$)
E	engulfment rate (s^{-1}), section 2.2
f^*	frequency of attachment, section 2.1 and Chapt. 5 and 6
G	growth rate ($m s^{-1}$), section 2.1
g	incorporation function (-), section 2.2
g	gravitational acceleration constant ($m s^{-2}$)
g_i	overall order of crystal growth, eq. 2.46
H	height (m)
h	proportionality constant, eq. 2.68
J	nucleation rate ($m^3 s^{-1}$ or $m^2 s^{-1}$)
k, k_r	reaction rate coefficient

List of symbols

k_B	Boltzmann constant ($m^2 \text{ Kg s}^{-2} \text{ K}^{-1}$)
K_B	Reaction equilibrium constant (l/mol)
k_d	diffusion mass transfer coefficient, eq. 2.44
K_G	overall crystal growth coefficient, eq. 2.46
k_{SL}	solid-liquid mass transfer coefficient, eq. 2.72
k_r	reaction rate of the integration process, eq. 2.45
l	length (m)
M	monomer, eq. 2.15
M	number of droplets, eq. 2.31
n	number of molecules in a cluster (-), section 2.1 and Chapt. 5 and 6
n	number of moles (-), Chapter 3
n^*	number of molecules in a critical nucleus (-)
N	number of nuclei, section 2.1
N	rotational rate of impeller (s^{-1}), sections 2.2 and Chapt. 3 and 4
N_a	Avogadro number (mol^{-1})
N_p	power number (-)
p	empirical parameter, eq.2.54
P	power input for a stirred tank (W)
P_E	experimental probability
Pe, Pe'	Peclet number
P_T	theoretical probability
Q	flow rate
r, R	radius (m)
Re	Reynolds number (-)
R_i	Reaction rate
S	Supersaturation (-)
Sc	Schmidt number (-)
Sh	Sherwood number (-)
T	Temperature (K)
t	time

List of symbols

t_g	growth time
t_i	induction time
t_n	nucleation time
t_μ	micromixing time
u, U	velocity (m s^{-1})
V, v	volume (m^3)
v_{av}	average velocity (m s^{-1})
W	nucleation work (J)
W^*	critical nucleation work (J)
X_s	segregation index (-)
Y	I_2 yield (-)
z	Zeldovich factor

Greek letters

α	micromixedness ratio, (-) section 2.2 and Chapt. 3 and 4
α_v	volume fraction of crystal to tot volume (-), eq.2.35 and 5.4
γ	interfacial energy (Kg s^{-2}), section 2.1
$\dot{\gamma}$	shear rate (s^{-1})
ε	energy dissipation rate (W/Kg)
ε_λ	molar extinction coefficient ($\text{m}^2 \text{mol}^{-1}$), Appendix A
η	Kolmogoroff scale (m), section 2.2
θ	contact angle (rad)
λ	wavelength (nm)
μ	chemical potential ($\text{m}^2 \text{Kg s}^{-2}$), section 2.1
μ	ionic strength (M), Chapter 3
μ	dynamic viscosity (Pa s), eq. 2.70 and 5.5
v	volume of a solute molecule in crystalline state, section 2.1
ν	kinematic viscosity (m^2/s), section 2.2 and Chapt. 3 and 4
v	volume of a fluid aggregate (m^3), eq. 2.53
ρ	density (Kg/m^3)
τ	time (s)
Φ	surface function (J), eq. 2.4

List of symbols

φ	non-dimensional energy dissipation rate (-), section 2.2 and Chapt 3 and 4)
ψ	Shape factor (-), section 2.1
ψ	velocity parameter (-), eq. 2.74 and 2.75
ω	collision frequency (s^{-1}), eq. 2.68

References

- Alm eras, E., Risso, F., Roig, V., Cazin, S., Plais, C., & Augier, F. (2015). Mixing by bubble-induced turbulence. *Journal of Fluid Mechanics*, 776, 458–474. doi:10.1017/jfm.2015.338
- Angst, W., Bourne, J. R., & Sharma, R. N. (1982). Mixing and fast chemical reaction - IV. *Chemical Engineering S*, 37(4), 585–590.
- Anna, S. L., Bontoux, N., & Stone, H. a. (2003). Formation of dispersions using “flow focusing” in microchannels. *Applied Physics Letters*, 82(3), 364. doi:10.1063/1.1537519
- Assirelli, M., Bujalski, W., Eaglesham, A., & Nienow, A. W. (2002). Study Of Micromixing in a Stirred Tank Using a Rushton Turbine. *Chemical Engineering Research and Design*, 80(8), 855–863. doi:10.1205/026387602321143390
- Assirelli, M., Bujalski, W., Eaglesham, A., & Nienow, A. W. (2008). Macro- and micromixing studies in an unbaffled vessel agitated by a Rushton turbine. *Chemical Engineering Science*, 63(1), 35–46. doi:10.1016/j.ces.2007.07.074
- Augustijns, P., & Brewster, M. (2007). *Solvent Systems and Their Selection in Pharmaceuticals and Biopharmaceutics*. (P. Augustijns & M. Brewster, Eds.). New York: Springer-Verlag.
- Awtrey, A. D., & Connick, R. E. (1951). The Absorption Spectra of I₂, I₃⁻, I⁻, IO₃⁻, S₄O₆⁼ and S₂O₃⁼. Heat of the Reaction I₃⁻ = I₂ + I⁻. *Journal of the American Chemical Society*, 73(4), 1842–1843. doi:10.1021/ja01148a504
- Ba dyga, J. (2016). Mixing and Fluid Dynamics Effects in Particle Precipitation Processes. *KONA Powder and Particle Journal*, 33(0), 127–149. doi:10.14356/kona.2016021
- Baldyga, J., & Bourne, J. R. (1983). A fluid mechanical approach to turbulent mixing and chemical reaction. Part I: inadequacies of available methods. *Chemical Engineering Communications*, 28, 231–241.
- Baldyga, J., & Bourne, J. R. (1989). Simplification of Micromixing Calculations. I. Derivation and Application of New Model. *The Chemical Engineering Journal*, 42, 83–92.
- Ba dyga, J., & Bourne, J. R. (1999). *Turbulent Mixing and Chemical Reactions*. Wiley. Retrieved from <https://books.google.co.uk/books?id=77FTAAAAMAAJ>
- Baldyga, J., & Pohorecki, R. (1995). Turbulent micromixing in chemical reactors - a review.

References

- The Chemical Engineering Journal*, 58(2), 183. Retrieved from <http://www.sciencedirect.com/science/article/pii/S0923046795029826>
- Bourne, J. R., & Yu, S. (1994). Investigation of micromixing in stirred tank reactors using parallel reactions. *Industrial & Engineering Chemistry Research*, 33(1), 41–55. doi:10.1021/ie00025a007
- Castro-Hernández, E., van Hoeve, W., Lohse, D., & Gordillo, J. M. (2011). Microbubble generation in a co-flow device operated in a new regime. *Lab on a Chip*, 11(12), 2023–9. doi:10.1039/c0lc00731e
- Chattopadhyay, S., Erdemir, D., Evans, J. M. B., Ilavsky, J., Amenitsch, H., Segre, C. U., & Myerson, A. S. (2005). SAXS study of the nucleation of glycine crystals from a supersaturated solution. *Crystal Growth and Design*, 5(2), 523–527. doi:10.1021/cg0497344
- Cheng, J., Feng, X., Cheng, D., & Yang, C. (2012). Retrospect and perspective of micro-mixing studies in stirred tanks. *Chinese Journal of Chemical Engineering*, 20(1), 178–190. doi:10.1016/S1004-9541(12)60378-4
- Chisti, Y. (2001). Hydrodynamic Damage to Animal Cells. *Critical Reviews in Biotechnology*, 21(2), 67–110. doi:10.1080/20013891081692
- Cui, Y. Q., Van der Lans, R. G. J. M., & Kuyben, K. (1996). Local power uptake in gas-liquid systems with single and multiple turbines. *Chemical Engineering Science*, 51(2631–2636).
- Custer, J. J., & Natelson, S. (1949). Spectrophotometric Determination of Microquantities of Iodine. *Analytical Chemistry*, 21(8), 1005–1009. doi:10.1021/ac60032a040
- Davey, R. J., Schroeder, S. L. M., & Ter Horst, J. H. (2013). Nucleation of organic crystals - A molecular perspective. *Angewandte Chemie - International Edition*, 52(8), 2167–2179. doi:10.1002/anie.201204824
- Dombrowski, R. D., Litster, J. D., Wagner, N. J., & He, Y. (2007). Crystallization of alpha-lactose monohydrate in a drop-based microfluidic crystallizer. *Chemical Engineering Science*, 62, 4802–4810.
- Dore, V., Tsaoulidis, D., & Angeli, P. (2012). Mixing patterns in water plugs during water/ionic liquid segmented flow in microchannels. *Chemical Engineering Science*, 80, 334–341. doi:10.1016/j.ces.2012.06.030

References

- Edward, J. T. (1970). Molecular Volumes and the Stokes-Einstein Equation. *Journal of Chemical Education*, 47(4), 261–270.
- Espuny Garcia del Real, G., Davies, J., & Bracewell, D. G. (2014). Scale-down characterization of post-centrifuge flocculation processes for high-throughput process development. *Biotechnology and Bioengineering*, 111(12), 2486–2498. doi:10.1002/bit.25313
- Falk, L., & Commenge, J.-M. (2010). Performance comparison of micromixers. *Chemical Engineering Science*, 65(1), 405–411. doi:10.1016/j.ces.2009.05.045
- Forsyth, C., Burns, I. S., Mulheran, P. A., & Sefcik, J. (2016). Scaling of Glycine Nucleation Kinetics with Shear Rate and Glass–Liquid Interfacial Area. *Crystal Growth & Design*, 16(1), 136–144. doi:10.1021/acs.cgd.5b01042
- Forsyth, C., Mulheran, P. A., Forsyth, C., Haw, M. D., Burns, I., & Sefcik, J. (2015). Influence of Controlled Fluid Shear on Nucleation Rates in Glycine Aqueous Solutions. *Crystal Growth & Design*, 15, 94–102. doi:10.1021/cg5008878
- Fournier, M.-C., Falk, L., & Villermaux, J. (1996). Assessing Micromixing Efficiency-- Determination of Micromixing Time By a Simple Mixing. *Chemical Engineering Science*, 51(23), 5187–5192.
- Furukawa, H., Kato, Y., Inoue, Y., Kato, T., Tada, Y., & Hashimoto, S. (2012). Correlation of power consumption for several kinds of mixing impellers. *International Journal of Chemical Engineering*, 2012. doi:10.1155/2012/106496
- Galkin, O., & Vekilov, P. G. (1999). Direct Determination of the Nucleation Rates of Protein Crystals. *The Journal of Physical Chemistry B*, 103(49), 10965–10971. doi:10.1021/jp992786x
- Garstecki, P., Fuerstman, M. J., Stone, H. a, & Whitesides, G. M. (2006). Formation of droplets and bubbles in a microfluidic T-junction-scaling and mechanism of break-up. *Lab on a Chip*, 6(3), 437–46. doi:10.1039/b510841a
- Gavriilidis, A., Angeli, P., Cao, E., Yeong, K. K., & Wan, Y. S. S. (2002). Technology and applications of microengineered reactors. *Inst. Chem. Eng.*, 80, 3–30.
- Gracin, S., & Rasmuson, Å. C. (2004). Polymorphism and Crystallization of p-Aminobenzoic Acid. *Crystal Growth & Design*, 4(5), 1013–1023. doi:10.1021/cg049954h
- Gracin, S., Uusi-Penttilä, M., & Rasmuson, Å. C. (2005). Influence of ultrasound on the nucleation of polymorphs of p-aminobenzoic acid. *Crystal Growth and Design*, 5(5),

References

- 1787–1794. doi:10.1021/cg050056a
- Gray, D. J., Treybal, R. E., & Barnett, S. M. (1982). Mixing of Single and Two Phase Systems: Power Consumption of Impellers. *AIChE Journal*, *28*, 195–198.
- Gray, R. A., Warren, P. B., Chynoweth, S., Michopoulos, Y., & Pawley, G. S. (1995). Crystallization of Molecular Liquids through Shear-Induced Nucleation. *Proceedings of the Royal Society of London. Series A: Mathematical and Physical Sciences*, *448*(1932), 113 LP-120. Retrieved from <http://rspa.royalsocietypublishing.org/content/448/1932/113.abstract>
- Guichardon, P., & Falk, L. (2000). Characterisation of micromixing efficiency by the iodide - iodate reaction system. Part I: experimental procedure. *Chemical Engineering Science*, *55*, 4233–4243.
- Guichardon, P., Falk, L., & Villermaux, J. (2000). Characterization of micromixing efficiency by the iodide-iodate reaction system. Part II: Kinetic study. *Chemical Engineering Science*, *55*, 4245–4253. doi:10.1016/S0009-2509(00)00069-5
- Hartman, R. L. (2012). Managing Solids in Microreactors for the Upstream Continuous Processing of Fine Chemicals. *Org. Process Res. Dev.*, *16*, 870–887.
- Hem, S. L. (1967). The effect of ultrasonic vibrations on crystallization processes. *Ultrasonics*, *5*(4), 202–207. doi:10.1016/0041-624X(67)90061-3
- Herbo, C., & Sigalla, J. (1957). Principes de l'iodimétrie absorptiométrique. *Analytica Chimica Acta*, *17*, 199–207. doi:http://dx.doi.org/10.1016/S0003-2670(00)87013-0
- Hofinger, J., Sharpe, R. W., Bujalski, W., Bakalis, S., Assirelli, M., Eaglesham, A., & Nienow, A. W. (2011). Micromixing in two-phase (G-L and S-L) systems in a stirred vessel. *Canadian Journal of Chemical Engineering*, *89*(5), 1029–1039. doi:10.1002/cjce.20494
- Hohmann, L., Greinert, T., Mierka, O., Turek, S., Schembecker, G., Bayraktar, E., ... Kockmann, N. (2018). Analysis of Crystal Size Dispersion Effects in a Continuous Coiled Tubular Crystallizer: Experiments and Modeling. *Crystal Growth & Design*, *18*(3), 1459–1473. doi:10.1021/acs.cgd.7b01383
- Hollander, E. D., Derksen, J. J., Kramer, H. M. J., Van Rosmalen, G. M., & Van den Akker, H. E. A. (2003). A numerical study on orthokinetic agglomeration in stirred tanks. *Powder Technology*, *130*(1), 169–173. doi:http://dx.doi.org/10.1016/S0032-5910(02)00261-9
- Huchet, F., Liné, A., & Morchain, J. (2009). Evaluation of local kinetic energy dissipation rate

References

- in the impeller stream of a Rushton turbine by time-resolved PIV. *Chemical Engineering Research and Design*, *87*(4), 369–376. doi:<https://doi.org/10.1016/j.cherd.2008.11.012>
- Jamshidi, R., Rossi, D., Saffari, N., Gavriilidis, A., & Mazzei, L. (2016). Investigation of the Effect of Ultrasound Parameters on Continuous Sonocrystallization in a Millifluidic Device. *Crystal Growth and Design*, *16*(8), 4607–4619. doi:10.1021/acs.cgd.6b00696
- Jawor-Baczynska, A., Moore, B. D., & Sefcik, J. (2015). Effect of mixing, concentration and temperature on the formation of mesostructured solutions and their role in the nucleation of dl-valine crystals. *Faraday Discussions*, *179*(0), 141–54. doi:10.1039/c4fd00262h
- Jawor-Baczynska, A., Sefcik, J., & Moore, B. D. (2013). 250 nm Glycine-Rich Nanodroplets Are Formed on Dissolution of Glycine Crystals But Are Too Small To Provide Productive Nucleation Sites. *Crystal Growth and Design*, *13*(2), 470–478. doi:10.1021/cg300150u
- Jiang, S., & Ter Horst, J. H. (2011). Crystal nucleation rates from probability distributions of induction times. *Crystal Growth and Design*, *11*(1), 256–261. doi:10.1021/cg101213q
- Joshi, J. B., & Sharma, M. M. (1976). Mass transfer characteristics of horizontal sparged contactors. *Transactions of the Institution of Chemical Engineers*, *54*, 42–53.
- Kashchiev, D. (2000). *Nucleation: basic theory with applications*. (Butterworth-Heinemann, Ed.). Boston.
- Kashchiev, D., & van Rosmalen, G. M. (2003). Review: Nucleation in solutions revisited. *Crystal Research and Technology*, *38*(78), 555–574. doi:10.1002/crat.200310070
- Kashchiev, D., & Van Rosmalen, G. M. (1991). Induction time and metastability limit in new phase formation. *Journal of Crystal Growth*, *110*, 373–380.
- Kleetz, T., Braak, F., Wehenkel, N., Schembecker, G., & Wohlgemuth, K. (2016). Design of Median Crystal Diameter Using Gassing Crystallization and Different Process Concepts. *Crystal Growth & Design*, *16*(3), 1320–1328. doi:10.1021/acs.cgd.5b01428
- Kleetz, T., Pätzold, G., Schembecker, G., & Wohlgemuth, K. (2017). Gassing Crystallization at Different Scales: Potential to Control Nucleation and Product Properties. *Crystal Growth & Design*, *17*(3), 1028–1035. doi:10.1021/acs.cgd.6b01280
- Kordylla, A., Koch, S., Tumakaka, F., & Schembecker, G. (2008). Towards an optimized crystallization with ultrasound: Effect of solvent properties and ultrasonic process

References

- parameters. *Journal of Crystal Growth*, 310(18), 4177–4184. doi:10.1016/j.jcrysgro.2008.06.057
- Kozicki, F., Bourne, J. R., & Rys, P. (1981). MIXING AND FAST CHEMICAL REACTION - I. *Chemical Engineering Science*, 36(10), 1643–1648.
- Krishna, R., & Ellenberger, J. (1996). Gas holdup in bubble column reactors operating in the churn-turbulent flow regime. *AIChE Journal*, 42(9), 2627–2634. doi:10.1002/aic.690420923
- Kubota, N. (2008). A new interpretation of metastable zone widths measured for unseeded solutions. *Journal of Crystal Growth*, 310(3), 629–634. doi:10.1016/j.jcrysgro.2007.11.123
- Kumar, A., Kumaresan, T., Pandit, A. B., & Joshi, J. B. (2006). Characterization of flow phenomena induced by ultrasonic horn. *Chemical Engineering Science*, 61(22), 7410–7420. doi:10.1016/j.ces.2006.08.038
- Kurup, G. K., & Basu, A. S. (2012). Field-free particle focusing in microfluidic plugs. *Biomicrofluidics*, 6(2), 1–10. doi:10.1063/1.3700120
- Laval, P., Salmon, J.-B., & Joanicot, M. (2007). A microfluidic device for investigating crystal nucleation kinetics. *Journal of Crystal Growth*, 303(2), 622–628. doi:10.1016/j.jcrysgro.2006.12.044
- Leng, J., & Salmon, J.-B. (2009). Microfluidic crystallization. *Lab on a Chip*, 9(1), 24–34. doi:10.1039/b807653g
- Li, W., Geng, X., Bao, Y., & Gao, Z. (2014). Micromixing characteristics in an aerated stirred tank with half elliptical blade disk turbine. *International Journal of Chemical Reactor Engineering*, 12(1), 231–243. doi:10.1515/ijcre-2012-0097
- Liao, Y., & Lucas, D. (2010). A literature review on mechanisms and models for the coalescence process of fluid particles. *Chemical Engineering Science*, 65(10), 2851–2864. doi:10.1016/j.ces.2010.02.020
- Liu, J., & Rasmuson, Å. C. (2013). Influence of Agitation and Fluid Shear on Primary Nucleation in Solution. *Crystal Growth & Design*, 13(10), 4385–4394. doi:10.1021/cg4007636
- Liu, J., Svärd, M., & Rasmuson, Å. C. (2014). Influence of Agitation and Fluid Shear on Nucleation of m -Hydroxybenzoic Acid Polymorphs. *Crystal Growth & Design*, 14(11),

References

- 5521–5531. doi:10.1021/cg500698v
- Liu, J., Svärd, M., & Rasmuson, Å. C. (2015). Influence of Agitation on Primary Nucleation in Stirred Tank Crystallizers. *Crystal Growth & Design*, 15(9), 4177–4184. doi:10.1021/cg501791q
- Llinas, A., & Goodman, J. M. (2008). Polymorph control: past, present and future. *Drug Discovery Today*, 13, 198–210.
- McLeod, J. ., Paterson, a. H. ., Bronlund, J. ., & Jones, J. . (2010). Nucleation of Alpha lactose monohydrate induced using flow through a venturi orifice. *Journal of Crystal Growth*, 312(6), 800–807. doi:10.1016/j.jcrysgr.2009.12.029
- Mersmann, A. (2001). *Crystallization technology handbook* (second edi.). New York.
- Mitchell, N. A., Frawley, P. J., & Ó'Ciardhá, C. T. (2011). Nucleation kinetics of paracetamolethanol solutions from induction time experiments using Lasentec FBRM®. *Journal of Crystal Growth*, 321(1), 91–99. doi:10.1016/j.jcrysgr.2011.02.027
- Miyasaka, E., Kato, Y., Hagsawa, M., & Hirasawa, I. (2006). Effect of ultrasonic irradiation on the number of acetylsalicylic acid crystals produced under the supersaturated condition and the ability of controlling the final crystal size via primary nucleation. *Journal of Crystal Growth*, 289(1), 324–330. doi:10.1016/j.jcrysgr.2005.11.084
- Monnier, H., Wilhelm, A. M., & Delmas, H. (1999a). Influence of ultrasound on mixing on the molecular scale for water and viscous liquids. *Ultrasonics Sonochemistry*, 6(1–2), 67–74. doi:10.1016/S1350-4177(98)00034-0
- Monnier, H., Wilhelm, A. M., & Delmas, H. (1999b). The influence of ultrasound on micromixing in a semi-batch reactor. *Chemical Engineering Science*, 54, 2953–2961.
- Mullin, J. W. (2001). *Crystallization* (4th ed.).
- Mullin, J. W., & Raven, K. D. (1962). Influence of mechanical agitation on the nucleation of some aqueous salt solutions. *Nature*, 195, 35–38.
- Murugesan, T. (1998). Dispersed Phase Hold-Up in Mechanically Agitated Gas – Liquid Contactors. *Journal of Chemical Technology and Biotechnology*, 72, 221–226.
- Myerson, A. S. (1952). *Handbook of Industrial Crystallization* (2nd ed.). Oxford: Butterworth-Heinemann.
- Nagy, Z. K., Fujiwara, M., Woo, X. Y., Braatz, R. D., & Kingdom, U. (2008). Determination of the Kinetic Parameters for the Crystallization of Paracetamol from Water Using

References

- Metastable Zone Width Experiments. *Industrial & Engineering Chemistry Research*, *47*, 1245–1252.
- Nanev, C. N., Hodzhaoglu, F. V., & Dimitrov, I. L. (2011). Kinetics of Insulin Crystal Nucleation, Energy Barrier, and Nucleus Size. *Crystal Growth & Design*, *11*(1), 196–202. doi:10.1021/cg1011499
- Norwood, K. W., & Metzner, A. B. (1960). Flow patterns and mixing rates in agitated vessels. *AIChE Journal*, *6*(3), 432–437. doi:10.1002/aic.690060317
- Nyvt, J., Skrivanek, J., & Gottfried, J. (1966). No Title. *Chem. Commun*, *31*, 2127.
- Pan, W., Vekilov, P. G., & Lubchenko, V. (2010). Origin of anomalous mesoscopic phases in protein solutions. *Journal of Physical Chemistry B*, *114*(22), 7620–7630. doi:10.1021/jp100617w
- Pérez, S. J. A., Porcel, R. E. M., López, C. J. L., Sevilla, F. J. M., & Chisti, Y. (2006). Shear rate in stirred tank and bubble column bioreactors. *Chemical Engineering Journal*, *124*, 1–5. doi:10.1016/j.cej.2006.07.002
- Priday, G., Silverblatt, C., Slottee, J. S., Smith, J., & Todd, D. (1999). Liquid-Solid Operations and Equipment. In R. Perry, D. Green, & J. Maloney (Eds.), *Perry's Chemical Engineers' Handbook* (7th ed.). McGraw-Hill.
- Rhein, O. H. (1976). Verfahren und Vorrichtung zur Kristallisationsbeschleunigung II.
- Robertson, B., & Ulbrecht, J. J. (1987). Measurements of shear rate on an agitator in a fermentation broth. In J. Y. Oldshue (Ed.), *Biotechnology Processes: Scale-up and mixing*, *AIChE* (pp. 72–81). New York.
- Rossi, D., Gavriilidis, A., Kuhn, S., Candel, M. A., Jones, A. G., Price, C., & Mazzei, L. (2015). Adipic Acid Primary Nucleation Kinetics from Probability Distributions in Droplet-Based Systems under Stagnant and Flow Conditions. *Crystal Growth & Design*, *15*(4), 1784–1791. doi:10.1021/cg501836e
- Rousseaux, J.-M., Falk, L., Muhr, H., & Plasari, E. (1999). Micromixing efficiency of a novel sliding-surface mixing device. *AIChE Journal*, *45*(10), 2203–2213. doi:10.1002/aic.690451018
- Rousseaux, J.-M., Muhr, H., & Plasari, E. (2000). Chemical reactors of special geometry for the precipitation of mineral particles. *The Canadian Journal of Chemical Engineering*, *78*(4), 650–662. doi:10.1002/cjce.5450780407

References

- Sathe, M., Joshi, J., & Evans, G. (2013). Characterization of turbulence in rectangular bubble column. *Chemical Engineering Science*, *100*, 52–68. doi:10.1016/j.ces.2013.01.004
- Shekunov, B. Y., & York, P. (2000). Crystallization processes in pharmaceutical technology and drug delivery design. *Journal of Crystal Growth*, *211*(1–4), 122–136.
- Sullivan, R. A. (2015). *Molecules, Clusters and Crystals: The Crystallisation of p-aminobenzoic acid from Solution*. The University of Manchester.
- Sullivan, R. A., & Davey, R. J. (2015). Concerning the crystal morphologies of the α and β polymorphs of p -aminobenzoic acid †. *CrystEngComm*, *17*(8), 1015–1023. doi:10.1039/C4CE01857E
- Sullivan, R. A., Davey, R. J., Sadiq, G., Dent, G., Back, K. R., Ter Horst, J. H., ... Hammond, R. B. (2014). Revealing the roles of desolvation and molecular self-assembly in crystal nucleation from solution: Benzoic and p -aminobenzoic acids. *Crystal Growth and Design*, *14*(5), 2689–2696. doi:10.1021/cg500441g
- Sundaram, S., & Collins, L. R. (1997). Collision statistics in an isotropic particle-laden turbulent suspension. Part 1. Direct numerical simulations. *Journal of Fluid Mechanics*, *335*, 75–109.
- Tanthapanichakoon, W., Aoki, N., Matsuyama, K., & Mae, K. (2006). Design of mixing in microfluidic liquid slugs based on a new dimensionless number for precise reaction and mixing operations. *Chemical Engineering Science*, *61*(13), 4220–4232. doi:10.1016/j.ces.2006.01.047
- Taylor, G. I. (1960). Deposition of a viscous fluid on the wall of a tube. *Journal of Fluid Mechanics*, *10*, 161–165.
- Teychené, S., & Biscans, B. (2011). Microfluidic device for the crystallization of organic molecules in organic solvents. *Crystal Growth and Design*, *11*(11), 4810–4818. doi:10.1021/cg2004535
- Teychené, S., & Biscans, B. (2012). Crystal nucleation in a droplet based microfluidic crystallizer. *Chemical Engineering Science*, *77*, 242–248. doi:10.1016/j.ces.2012.01.036
- Thorsen, T., Roberts, R. W., Arnold, F. H., & Quake, S. R. (2001). Dynamic Pattern Formation in a Vesicle-Generating Microfluidic Device. *Physical Review Letters*, *86*, 4163–4166.
- Thulasidas, T. C., Abraham, M. a., & Cerro, R. L. (1997). Flow patterns in liquid slugs during bubble-train flow inside capillaries. *Chemical Engineering Science*, *52*(17), 2947–2962.

References

- doi:10.1016/S0009-2509(97)00114-0
- Turner, T. D., Corzo, D. M. C., Toroz, D., Curtis, A., Dos Santos, M. M., Hammond, R. B., ... Roberts, K. J. (2016). The influence of solution environment on the nucleation kinetics and crystallisability of para-aminobenzoic acid. *Phys. Chem. Chem. Phys.*, *18*(39), 27507–27520. doi:10.1039/C6CP04320H
- Vekilov, P. G. (2010). The two-step mechanism of nucleation of crystals in solution. *Nanoscale*, *2*, 2346–2357. doi:10.1063/1.3476239
- Villermaux, J. (1986). Macro and Micromixing Phenomena in Chemical Reactors. In H. I. de Lasa (Ed.), *Chemical Reactor Design and Technology: Overview of the New Developments of Energy and Petrochemical Reactor Technologies. Projections for the 90's* (pp. 191–244). Dordrecht: Springer Netherlands. doi:10.1007/978-94-009-4400-8_6
- Villermaux, J., Falk, L., & Fournier, M.-C. (1994). Potential use of a new parallel reaction system to characterize micromixing in stirred reactors. *AIChE Journal*, *90*(299), 50–54.
- Volmer, M. (1939). Kinetic der Phasenbildung. *Steinkopff*.
- Wagner, N. J., & Brady, J. F. (2009). Shear thickening in colloidal dispersions. *Physics Today*, *62*(10), 27–32. doi:10.1063/1.3248476
- Wohlgemuth, K. (2012). *Induced Nucleation Processes during Batch Cooling Crystallization*. Technischen Universität Dortmund. Retrieved from <http://scholar.google.com/scholar?hl=en&btnG=Search&q=intitle:Induced+Nucleation+Processes+during+Batch+Cooling+Crystallization#0>
- Wohlgemuth, K., Kordylla, A., Ruether, F., & Schembecker, G. (2009). Experimental study of the effect of bubbles on nucleation during batch cooling crystallization. *Chemical Engineering Science*, *64*(19), 4155–4163. doi:10.1016/j.ces.2009.06.041
- Wohlgemuth, K., Ruether, F., & Schembecker, G. (2010a). Sonocrystallization and crystallization with gassing of adipic acid. *Chemical Engineering Science*, *65*(2), 1016–1027. doi:10.1016/j.ces.2009.09.055
- Wohlgemuth, K., Ruether, F., & Schembecker, G. (2010b). Sonocrystallization and crystallization with gassing of adipic acid. *Chemical Engineering Science*, *65*(2), 1016–1027. doi:10.1016/j.ces.2009.09.055
- Xiao, Y., Tang, S. K., Hao, H., Davey, R. J., & Vetter, T. (2017). Quantifying the Inherent

References

Uncertainty Associated with Nucleation Rates Estimated from Induction Time Data Measured in Small Volumes. *Crystal Growth and Design*, 17(5), 2852–2863. doi:10.1021/acs.cgd.7b00372

Zarkadas, D. M., & Sirkar, K. K. (2007). Cooling Crystallization of Paracetamol in Hollow Fiber Devices. *Industrial & Engineering Chemistry Research*, 46(10), 2928–2935.